Direct-Write Assembly of Colloidal Materials

by

Alvin Thong Lip Tan

B.S., Northwestern University, 2011

M.S., Northwestern University, 2012

Submitted to the Department of Materials Science and Engineering in partial fulfillment of the requirements for the degree of

Doctor of Philosophy in Materials Science and Engineering

at the

Massachusetts Institute of Technology

September 2019

Signature redacted

Signature of Author: .....
Department of Materials Science and Engineering
August 16, 2019

Signature redacted

Certified by: .....
Robert J. Macfarlane
Assistant Professor of Materials Science and Engineering
Thesis Reader

Signature redacted

Certified by: .....
Anastasios John Hart
Associate Professor of Mechanical Engineering
Thesis Supervisor

Signature redacted

Certified by: .....
Donald R. Sadoway
Professor of Materials Science and Engineering
Chair, Departmental Committee of Graduate Studies

Direct-Write Assembly of Colloidal Materials

by

Alvin Thong Lip Tan

Submitted to the Department of Materials Science and Engineering
on August 16, 2019 in partial fulfillment of the
requirements for the degree of Doctor of Philosophy
in Materials Science and Engineering

Abstract

Colloidal assembly, which is the spontaneous organization of nano- and micro- sized particles, is an attractive means to create materials with properties that can be engineered via hierarchy of particle composition, size, ordering, and macroscopic form. However, while there are well-established methods for assembling colloidal crystals as films and patterns on substrates, it has not been previously possible to build freeform colloidal crystal structures. Macroscale, freeform colloidal crystals could enable the development of novel composites, photonics, electronics, and new studies of crystallization in three-dimensions. This thesis describes the development of direct-write assembly, a process combining the bottom-up principle of colloidal self-assembly with the versatility of direct-write 3-D printing. Direct-write assembly is performed by precision dispense of a colloidal suspension from a fine needle into a temperature-controlled environment. Using polystyrene particles suspended in water as a model system, we derive a scaling law that governs the rate of assembly. Moreover, by high resolution motion control of the substrate, the trajectory of crystal growth, and therefore the shape of the crystal, can be controlled in freeform. We show how to prevent cracking in these free-standing colloidal crystals, and demonstrate the emergence of structural color tunable by particle size. We also explore in-plane direct-write as a means for fabricating colloidal crystals patterned by a digital template. The kinetics of crystal growth can be modelled by the Dimitrov-Nagayama equation for convective assembly, which allows us to develop an operational phase diagram to serve as a practical guide for high-throughput assembly. Moreover, we develop a means of rapidly characterizing grain structure from the optical diffractive properties of the colloidal crystal. By sequentially sintering and overlapping passes, in-plane direct-write can potentially build up to 3-D structures. Finally, we consider the scaling of forces in the direct-write assembly process and demonstrate that direct-write can be extended to various particle systems. In particular, we demonstrate application of direct-write to the assembly of colloidal silica, gold, and iron oxide supercrystals.

Thesis Supervisor: A. John Hart, Associate Professor of Mechanical Engineering
Thesis Reader: Robert J. Macfarlane, Assistant Professor of Materials Science and Engineering
Thesis Committee Members:
Caroline Ross, Professor of Materials Science and Engineering
Mathias Kolle, Assistant Professor of Mechanical Engineering, MIT

Acknowledgements

I would like to thank Professor A. John Hart for guiding my PhD. I have benefitted from his energy, enthusiasm, and encouragement in all areas of research, including formulating research ideas, designing experiments, discussing results, writing, and presenting. Working in his lab has been a marvelous experience, and I hope that others might have a similar experience working with me in future. In addition to John, I also received much valuable advice from my other thesis committee members: Professors Caroline Ross, Robert Macfarlane, and Mathias Kolle.

Second, I would like to thank John's Mechanosynthesis Group and our many collaborators. Mostafa Bedewy and Justin Beroz did some important early work before I joined the group. I thank Justin for his expertise in machine design, our wide-ranging discussions of interesting physics, and practical help in the many things that we worked on together. I also thank Cécile Chazot for listening to some of my outlandish research ideas and actually coming up with helpful suggestions.

When I got interested in structural color, John introduced me to Prof. Mathias Kolle, who helped me build depth in the area and was very generous in letting me work in his optics lab, even teaching me how to use some of the instruments himself. I enjoyed the support and company of the students in his group, and have been fortunate to collaborate with Sara Nagelberg in our analysis of iridescence using ping-pong balls.

Some of the classes that I took helped me build good foundation and perspective for my thesis work. In particular, Prof. Daniel Blankschtein's class on colloids and Prof. John Bush's class on fluid mechanics helped me think lucidly about my experiments. Prof. Eugene Fitzgerald helped me formulate perspective on doing innovative work. I thank them for their world-class instruction.

I am indebted to undergraduate and high school researchers who have assisted in experiments and data analysis: Elizabeth Chang-Davidson (MIT), Joel Tan (SUTD), Benjamin Liu (Arcadia High School), Daniel Shkreli (MIT), and Johan Villanueva (MIT). Thank you for working with me and contributing to this work. It has been a privilege being your grad mentor.

I thank my family and friends: My parents were my first teachers, and encouraged me to broaden my horizons. Some of the tinkering in home-made experiments with my brother probably translated to useful lab skills. At MIT, I was fortunate to be a part of communities outside the lab, such as Burton-Conner House, Sidney-Pacific Graduate Community, the Addir Fellows, and the Lutheran-Episcopal Ministry. I also thank the MIT Spinning Arts Club and MIT Skydiving Club for healthy forms of recreation that keep me in peak physical and mental condition.

This research was supported by the National Science Foundation CAREER Award (CMMI-1346638, to A.J.H.) and by the MIT-Skoltech Next Generation Program. Additionally, I thank the Singapore Defence Science Organisation for a postgraduate scholarship.

Contents

1 Introduction and Background 7

1.1 Hierarchically structured materials 7

1.2 Evaporative self-assembly 8

1.3 Direct-write 3-D printing 14

2 Freeform direct-write assembly 17

2.1 Direct-write assembly of freestanding colloidal crystals 17

2.2 Kinetics of assembly 21

2.3 Freeform assembly 24

2.4 Optical properties 24

2.5 Cracking control 26

2.6 Conclusions 32

2.7 Experimental details 32

2.8 Supporting Information 39

3 In-plane direct-write assembly 53

3.1 In-plane direct-write assembly of patterned colloidal crystals 53

3.2 Kinetics of in-plane assembly 56

3.3 Effect of toolpath 59

3.4 Optical properties 63

3.5 Conclusions 67

3.6 Experimental details 69

3.7 Supporting Information 71

4 Generalizing direct-write assembly 76

4.1 General scaling of forces in direct-write assembly 76

4.2 Direct-write assembly of non-polymer particles 82

4.3 Direct-write assembly with non-aqueous colloids 84

4.4 Observations on the limits of crystalline assembly 91

4.5 Supporting Information 96
5 Conclusion and Outlook 99
5.1 Summary 99
5.2 Future opportunities 99
6 References 102

1 Introduction and Background

This chapter uses some text originally written for the following journal articles:

1. Tan, A. T. L.*; Beroz*, J.; Kolle, M.; Hart, A. J. Direct-Write Freeform Colloidal Assembly. *Adv. Mater.* **2018**, *30* (44), 1803620.
2. Sharma, M.*; Tan, A. T. L.*; Smith, B. D.; Hart, A. J; Grossman, J. C. Hierarchically Structured Nanoparticle Monolayers for the Tailored Etching of Nanoporous Silicon. *ACS Appl. Nano Mater.* **2019**, 2 (3), 1146-1151.

*Equal contribution

1.1 Hierarchically structured materials

Structural hierarchy–which involves the control of composition and form across length scales–is a powerful strategy for creating functional natural and synthetic materials. In natural materials, examples of hierarchical morphology can be found in, for instance: butterfly wings, which display intricate photonic effects;[1] the xylem architecture of plants, which feature optimized mass transport [2] and the skeletal structure of sea sponges, which possess outstanding mechanical properties.[3] In synthetic materials, colloidal particles can be assembled into crystals that exhibit unique optical,[4,5] chemical,[6,7] and mechanical[8,9] properties based on particle geometry, composition and arrangement. Colloidal assembly therefore enables materials design for diverse applications including optical coatings,[10] biological and chemical sensors,[11] and battery electrodes.[12]

Self-assembly can also be performed on colloidal particles of various geometries to attain emergent properties and functionalities. Seminal work by Vlasov et al.[5] (Fig. 1.1a) has shown

that assembled arrays of silica microparticles demonstrate a photonic bandgap, a property that arises due to the periodicity of the crystal lattice, rather than the individual particles themselves. Self-assembly can also be performed on colloidal particles of other geometries to attain emergent properties and functionalities. For example, Fig. 1.1b shows an array of aligned silver nanowires assembled by the LB technique. Each silver nanowire has a diameter of approximately 50 nm and aspect ratio of 50. The array of aligned silver nanowires collectively function as excellent substrates for surface enhanced Raman spectroscopy (SERS).[13] Even more recently, it has been possible to assemble colloidal particles into non-planar structures. Confinement of colloids within liquid droplets and assembly upon evaporation yields spherical clusters of particles, such as photonic "balls" (Fig. 1.1c) for optical applications such as visual displays [14–18] and crumpled balls of graphene for energy applications such as electrochemical storage.[19–21]

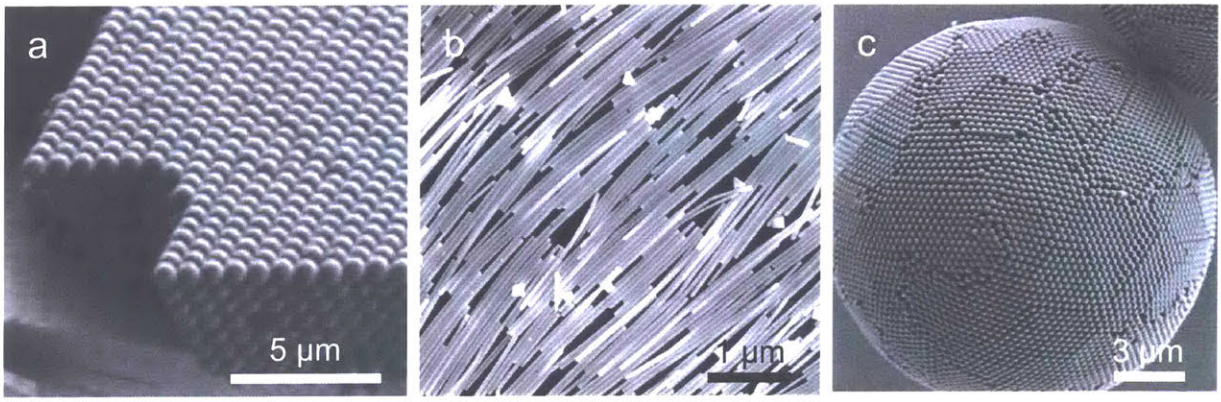

Figure 1.1. Examples of colloidal assembly. (a) Silica colloidal crystal assembled by evaporative assembly from Ref. [22] (b) Silver nanowires aligned by Langmuir-Blodgett Assembly from Ref. [13], (c) Polystyrene particles assembled into a photonic ball from Ref. [23].

1.2 Evaporative self-assembly

Colloidal particles can be directed by intermolecular and surface forces, and thus self-assemble into larger aggregates. Thus, self-assembly provides a pathway to establish hierarchy in colloidal

assembly.[24,25] However, the assembly of colloidal particles into a structure of well controlled geometry is non-trivial, even for a simple geometry such as a uniform film. Indeed, the common phenomenon of a drying drop of coffee provides a case in point. One might consider coffee as a colloidal suspension with the coffee grinds as the particulate phase and water as the fluid phase. When the droplet is left to dry, instead of forming a uniform film, the coffee dries as a ring stain (Fig. 1.2a) due to capillary flows that preferentially transport the coffee particles to the edge of the droplet (Fig. 1.2b). The result is thick deposit of particles at the edge of the droplet and sparse deposits in the middle of the droplet, as illustrated in Fig. 1.2b.

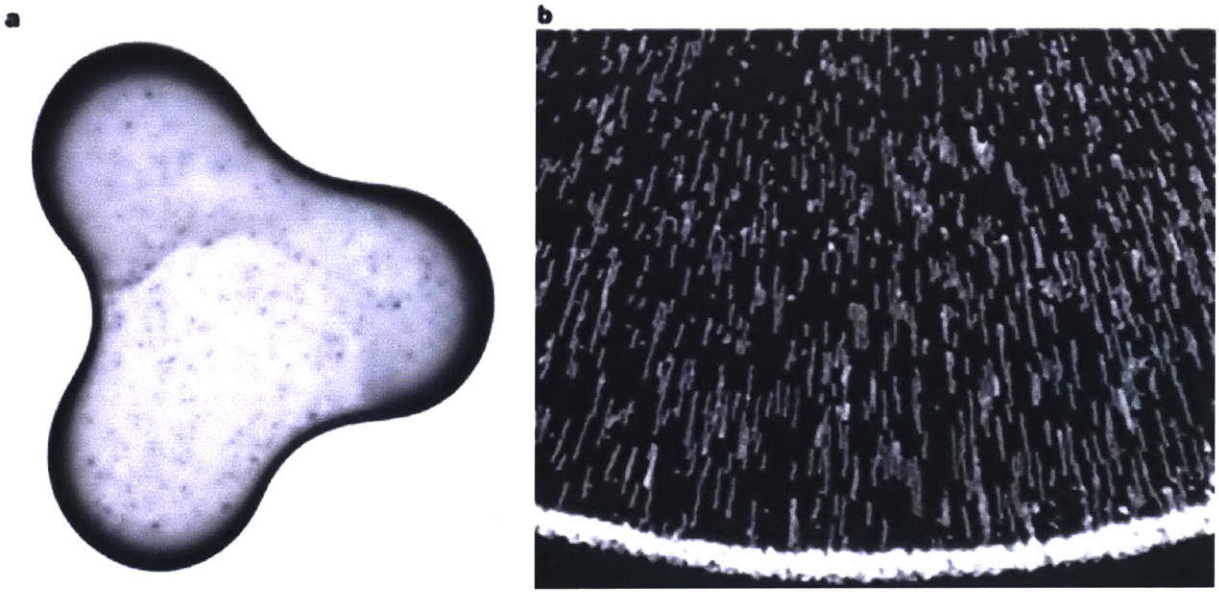

Figure 1.2. The coffee-ring effect. (a) A 2-cm-diameter drop of coffee containing 1 wt% solids that has dried to form a perimeter ring, accentuated in regions of high curvature. (b) Spheres in water during evaporation, as described in the text. Multiple exposures are superimposed to indicate the motion of the microspheres. Reproduced from Ref. [26].

Nevertheless, there are techniques that, through planar confinement in the evaporative process, yields large area films suitable for applications such as electronics and optical displays.

Such techniques include dip-coating, Langmuir-Blodgett drawing, [27,28] and blade-casting [29,30]. In my own work, I have utilized blade-casting as a means for assembling nanoparticles into a two-dimensional monolayer array. In blade-casting, a blade is used to stretch the meniscus of a colloidal suspension laterally across the substrate, resulting in uniform evaporative self-assembly at the trailing edge of the meniscus, as illustrated in Fig. 1.3. Blade-casting, and other similar methods, are an attractive means for scaling up the self-assembly of colloidal particles into films.

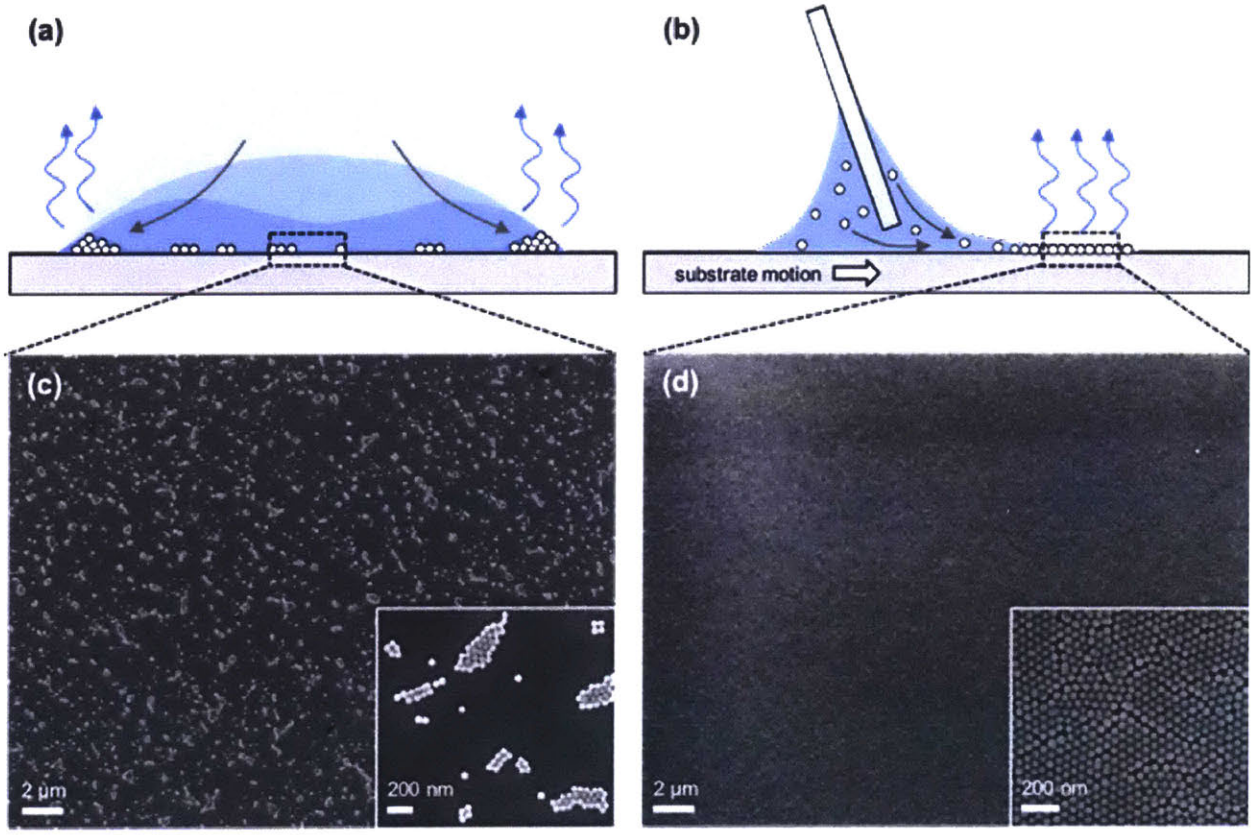

Figure 1.3. Evaporative self-assembly by drop-casting and blade-casting. (a) Illustration of drop casting, where evaporation is highest at the edge of the droplet, resulting in thick 'coffee ring' deposits at the edge and sparse particle islands at the middle of the drop. (b) Illustration of blade-casting, where a blade is used to draw the meniscus laterally across the substrate, resulting in uniform evaporative self-assembly of particles at the trailing edge. (c-d) SEM of particle deposits formed by (c) drop-casting, and (d) blade-casting. Reproduced from Ref. [31]

It is possible to create patterned films, i.e., film structures of higher order complexity, by manipulation of wetting phenomena. Here, we look at two examples in the literature. Masuda et al.[32] demonstrated that, by first treating a silicon substrate with a hydrophobic self-assembled monolayer (SAM), one could cause an oscillatory slip-stick motion of the contact line while colloidal particles assemble onto the substrate, as shown in Figure 1.4. The result is an array of colloidal particle stripes, assembled perpendicular to the drying direction. Conversely, one could create an array of stripes parallel to the drying direction. Huang et al.[33] reported the formation of metal nanoparticles stripes on a hydrophilic substrate by harnessing a fingering instability at the contact line, as shown in Figure 1.5.

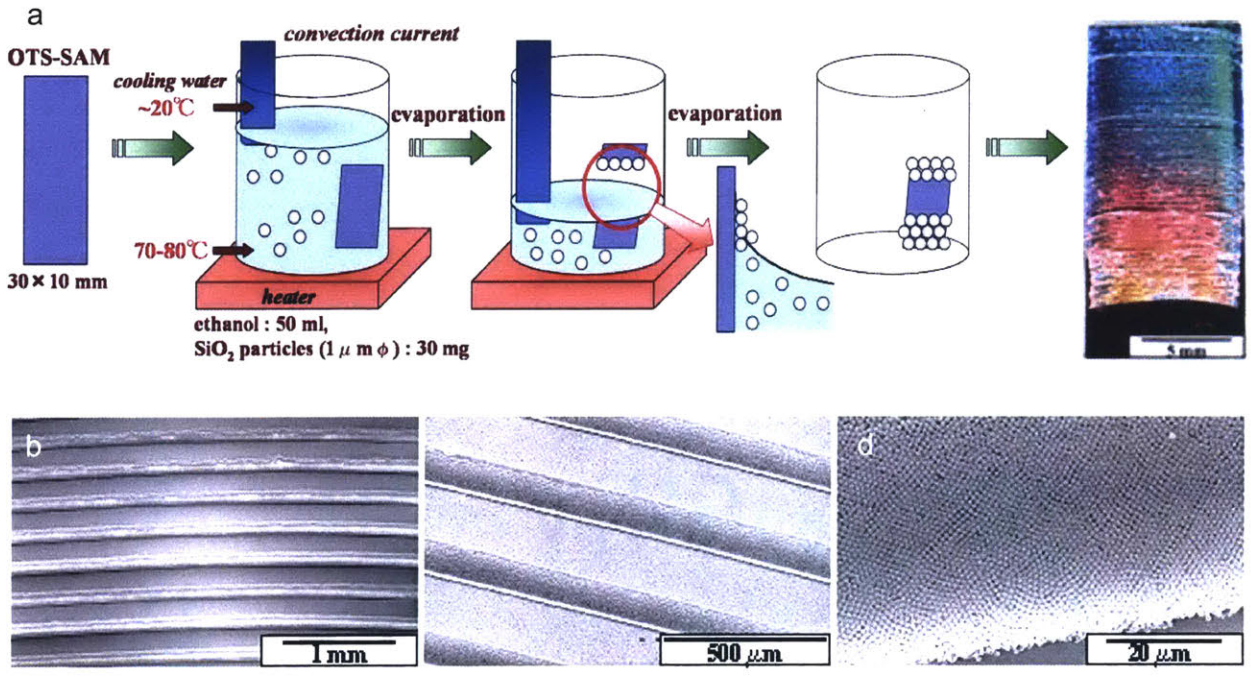

Figure 1.4. (a) Schematic for self-assembly process to fabricate an orderly array of particle wires constructed from a close-packed structure. (b)-(d) SEM micrographs of arrays of particle wires. Adapted from Ref. [32]

In my own work, we have used the blade-casting platform to harness both slip-stick motions and fingering instabilities to create a variety of film patterns. As shown in Figure 1.6, by blade casting a dilute suspension (6.7×10^{12} particles/mL) of 10-nm gold core particles at low blade speeds (0.002 mm/s), slip-stick motion is dominant and stripes perpendicular to the drying direction is obtained. At higher speeds (0.015 mm/s – 0.1 mm/s), a fingering instability causes the stripes to become webbed, and at very high speeds (0.15 mm/s), sparse clusters of nanoparticles form.

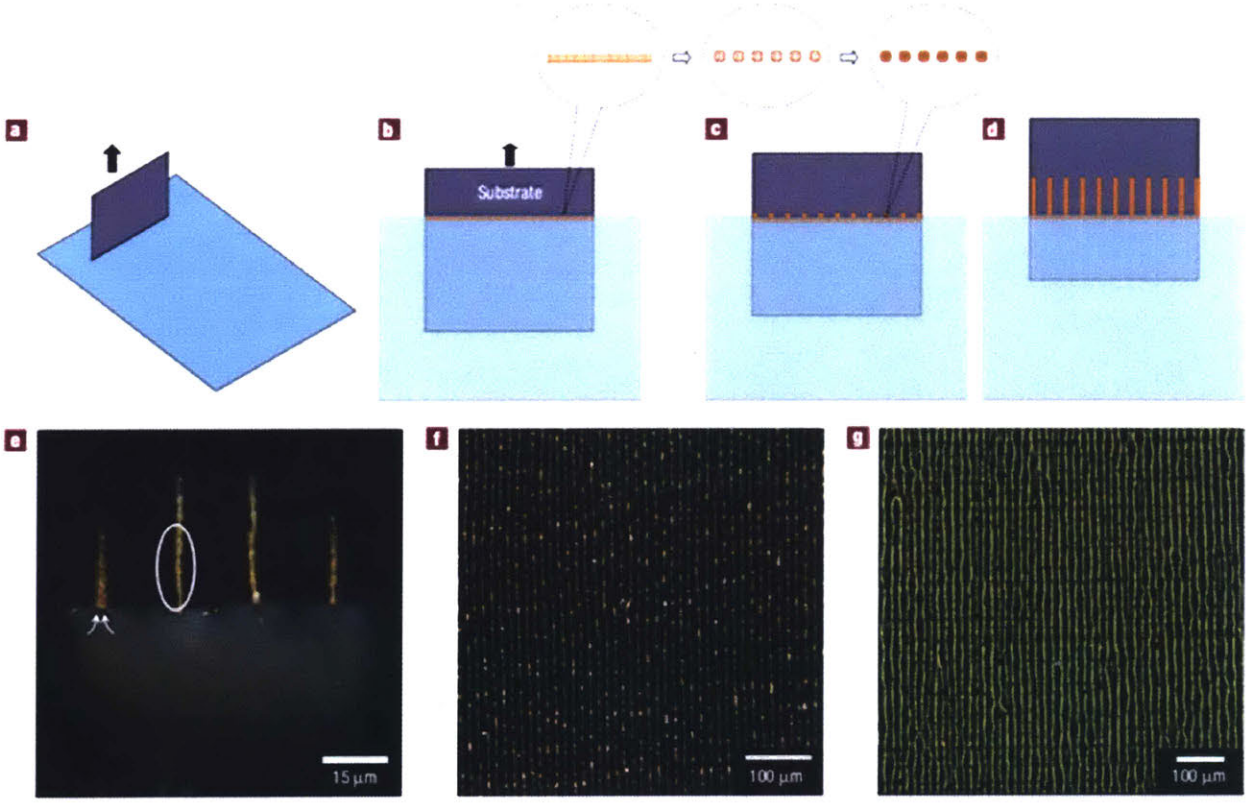

Figure 1.5. a–d, A schematic drawing illustrating the formation of an aligned gold nanoparticle stripe pattern by vertical deposition (a,b). Only the nanoparticles at the water–substrate contact line (gold dots in b–d) are shown for clarity. The substrate is raised slowly (a,b) so that water is evaporated when a new surface is exposed. The 'wet' contact line containing uniformly dispersed nanoparticles breaks up into aggregates of nanoparticles (b,c) owing to the fingering instability during the initial dewetting stage. These fingertips then guide further deposition of nanoparticles, finally forming the extended stripe pattern (d). e, Direct optical microscopy

observation of the water front reveals a rapid motion of nanoparticles towards the wet tips (circled area) of the stripes as indicated by the arrows. This leads to the unidirectional growth of the stripes across the entire substrate as shown in the optical microscopy image in f. g, Silver nanoparticle stripes have been obtained in the same fashion. Reproduced from [33]

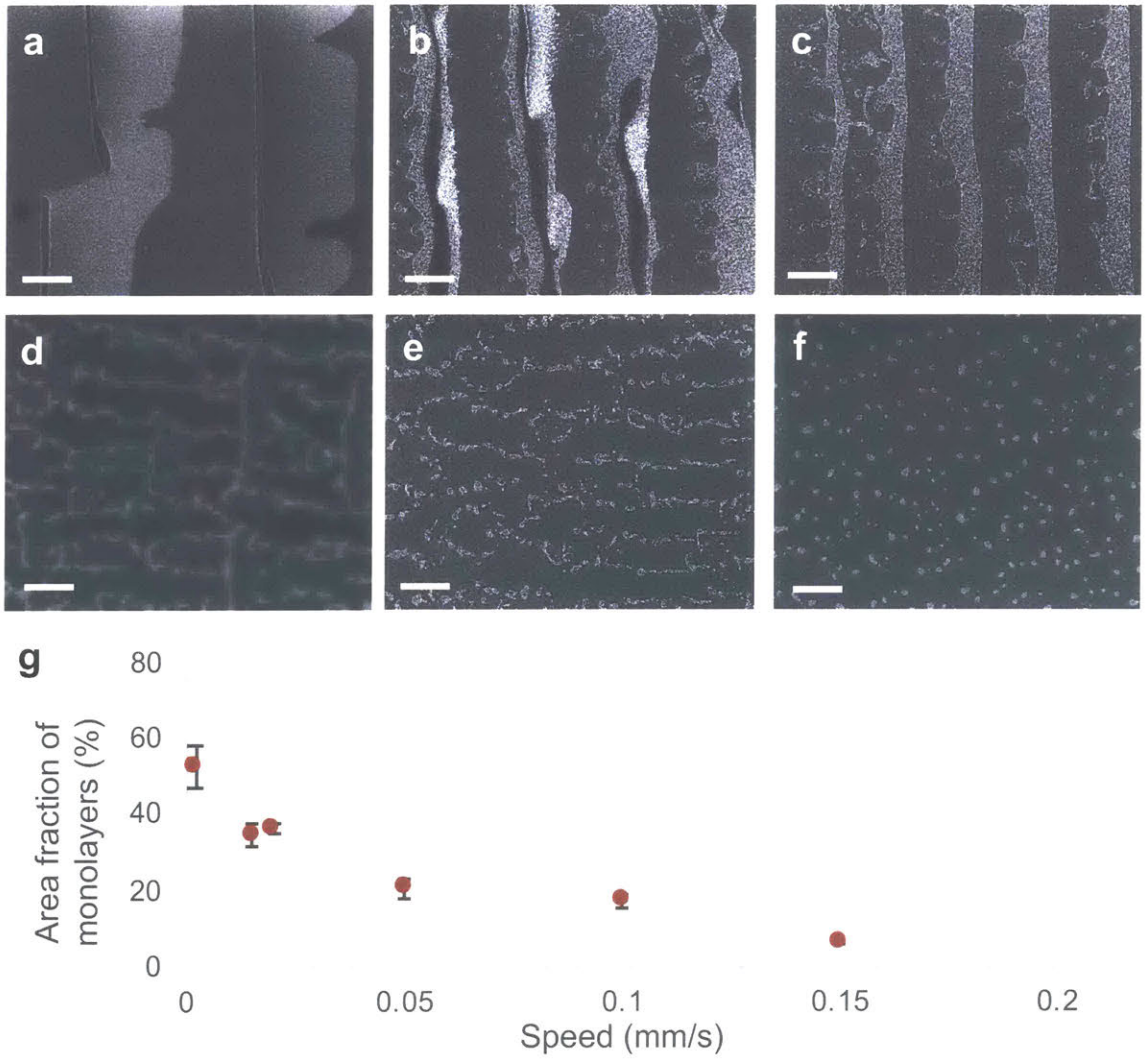

Figure. 1.6. SEM images of blade casted silicon produced using substrate speeds of (a) 0.002 mm/sec, (b) 0.015 mm/sec, (c) 0.02 mm/sec, (d) 0.05 mm/sec, (e) 0.1 mm/sec, (f) 0.15 mm/sec. Scale bars represent 10 μm. (g) Plot of area fraction of monolayer against blade speed, as obtained by image analysis of SEM images. Reproduced from [31]

These, and other established techniques for evaporative self-assembly, enable the organization of nanoparticles over large areas. We note, however, that these techniques are limited to thin films on substrates and the assembly of nanoparticles into out-of-plane structures remains a challenge.

1.3 Direct-write 3-D printing

Another emerging fabrication technique, direct-write 3D printing, has been used to build miniature antennae,[34] lightweight composites,[35] batteries,[36] and many other functional structures from metallic, dielectric, polymer, and biomaterial inks. In direct-write printing, an ink is provided to a needle or nozzle, which is moved with respect to a substrate as the ink is extruded. The rheology of the ink is typically engineered to give it a well-defined yield stress, therefore requiring cohesion between particles in high-density suspensions,[37] and enabling intricate freeform structures to be built.

Fig. 1.7a shows work by Lewis et al. performing direct-writing of colloidal silver on a hemispherical surface.[38] The concentration of silver particles in the ink is high and the particles form a percolated network within the dried ink. Therefore, each ink trace constitutes an electrically conductive path. Direct-writing of the silver ink into serpentine patterns creates a new functionality beyond electrical conductivity: An electrically conductive trace fashioned into such a geometry can be used as an antenna. Since the shape and periodicity of the serpentine

trace can be directly controlled by a computer, various antenna designs can be readily fabricated and optimized towards various frequencies and bandwidths.

Direct ink-writing has also been demonstrated as an enabling technology for biomedical applications[39,40], such as creating artificial blood vessels[41]. The example shown in Fig. 1.7b is a hydrogel with fluidic channels in its interior mimicking branched blood vessel networks. The channel networks were fabricated from a template created by direct ink-writing. This example is noteworthy for its creative use of direct writing as a templating technique to create complex inverse structures.

Direct-ink writing has also been used to create new materials with enhanced properties. Fig. 1.7c shows a graphene aerogel fabricated by direct writing graphene-laden ink into microlattice architecture. While random porous network aerogels can be readily created with bulk processing techniques, Worsley et al. have shown that, by using direct-write extrusion to fabricate aerogels of a designed architecture, mechanical properties such as the Young's modulus can be improved by an order of magnitude compared to bulk graphene aerogels of comparable geometric density.[42]

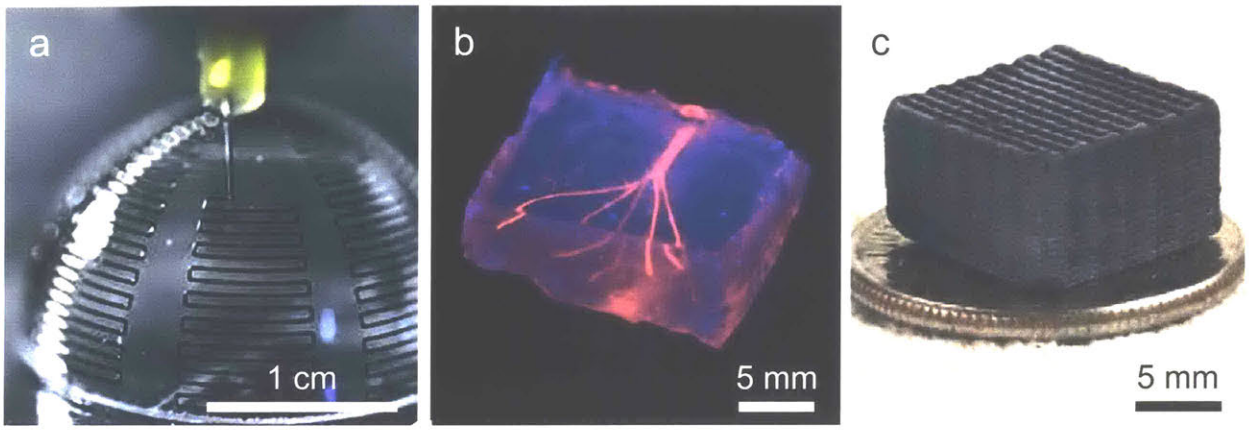

Figure 1.7. Emerging applications of direct write extrusion: (a) Conformal patterning of antennas from Ref. [38] (b) Templating artificial blood vessels in a hydrogel matrix from Ref. [41], (c) Fabrication of graphene aerogel, from Ref. [42].

Nevertheless, due to the need for specific ink rheology, direct ink writing does not allow long range crystalline ordering in the final structure.[43–45] If crystalline order can be achieved using colloidal building blocks in a direct-write process, emergent properties such as photonic[4,5] and electronic band gaps,[46] could be achieved.

Extending colloidal self-assembly to three dimensions would enable new applications uniquely enabled by macroscale colloidal crystals with complex geometry.

2 Freeform direct-write assembly

The work presented in this section was a joint effort with fellow graduate student Justin Beroz. The methods, procedures and construction of the experiment apparatus were developed jointly between us. The modelling effort, particularly on cracking of colloidal crystals, is credited to Justin Beroz. I designed and performed most of the experiments, including sample fabrication, microstructural characterization, optical characterization, image processing and analysis. X-ray Microscopy measurements and analysis were performed by courtesy of Dr. Stephen Kelly of Carl Zeiss X-ray Microscopy, Inc. This chapter uses text originally written for the following journal articles:

1. Tan*, A. T. L.; Beroz*, J.; Kolle, M.; Hart, A. J. Direct-Write Freeform Colloidal Assembly. *Adv. Mater.* **2018**, *30* (44), 1803620.
2. Beroz, J.*; Tan, A. T. L.*; Kamrin, K.; Hart, A. J. Crack-free colloidal crystal macrostructures. *In preparation.*

*Equal contribution

2.1 Direct-write assembly of freestanding colloidal crystals

By combining principles from direct-write 3-D printing and colloidal self-assembly, we can create materials with hierarchical complexity and order. In this chapter, I discuss the development of a new fabrication technique – direct-write assembly – that combines the principles and advantages of evaporative colloidal assembly with the versatility and scalability of direct-write 3D printing. This approach allows for both local control of particle organization, and global control of the shape of the structure.

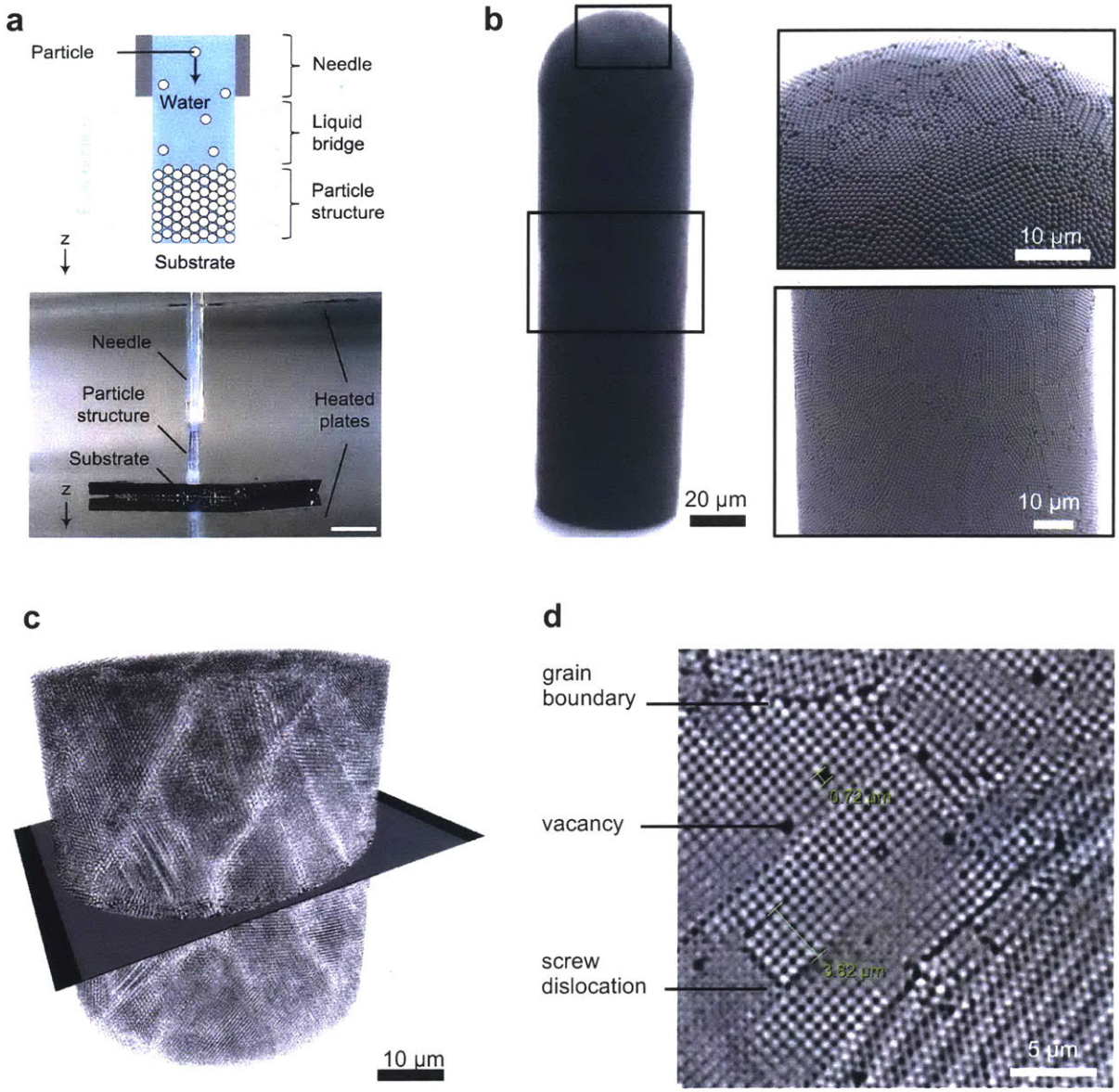

Figure 2.1. Direct-write assembly of macroscale freestanding colloidal crystal structures. a) Direct-write assembly is performed by precision dispensing of a colloidal solution from a fine needle, followed by controlled downward or multi-axis substrate motion to build the structure, as shown in the schematic (top) and in the photograph (bottom). Scale bar: 2 mm. b) Scanning electron microscopy (SEM) image of a freestanding structure comprising of particles of radius a = 500 nm. Insets: close views of top and middle sections. c) Three-dimensional reconstruction of the interior of a freestanding colloidal structure, as imaged by X-ray microscopy. d) High-magnification view of a portion of the cross-section indicated in (c), revealing crystal defects such as vacancies, dislocations, and grain boundaries.

Direct-write assembly is performed using a custom-built apparatus wherein a colloidal solution is dispended through a needle, with fine position control relative to a substrate, in a temperature-controlled environment (Figure 2.1a and Figure S2.1). The formation of a colloidal structure is initiated by dispensing a small amount of suspension to form a liquid bridge between the substrate and the orifice of the needle. This liquid bridge provides confinement for the assembling particles that accumulate at the base of the liquid bridge. In turn, we observe accumulation of particles into a solid layer at the base of the liquid bridge and retract the substrate downward as the particles accumulate. Continuing, we move the substrate downward at a rate matched to the vertical growth rate of the particle structure; this enables construction of high aspect ratio vertical structures (Figure 2.1), which we call colloidal "towers". The formation process can be terminated at any point by halting the flow from the needle, after which evaporation collapses the liquid bridge (Figure S2.2); freestanding structures several millimeters tall can be easily drawn. The dispense rate (~10^{-2} μl/s) and translational motions of the substrate relative to the needle (~1 μm/s) are motor controlled, and the needle, tower, and substrate are viewed *in situ* with video microscope cameras.

The radius R of the colloidal towers is nominally set by the needle radius, and the local width and curvature of the structure can be modulated by changing the dispense rate relative to the vertical rate of motion, as shown in Figure S2.3. When the dispense rate is lesser than the rate of evaporation, the liquid bridge necks, as shown in region (i). When the dispense rate is greater than the rate of evaporation, the liquid bridge bulges, as shown in region (ii). The result is a

structure of varying cross section, as exemplified by the 'hourglass' structure shown in Figure S2.3.

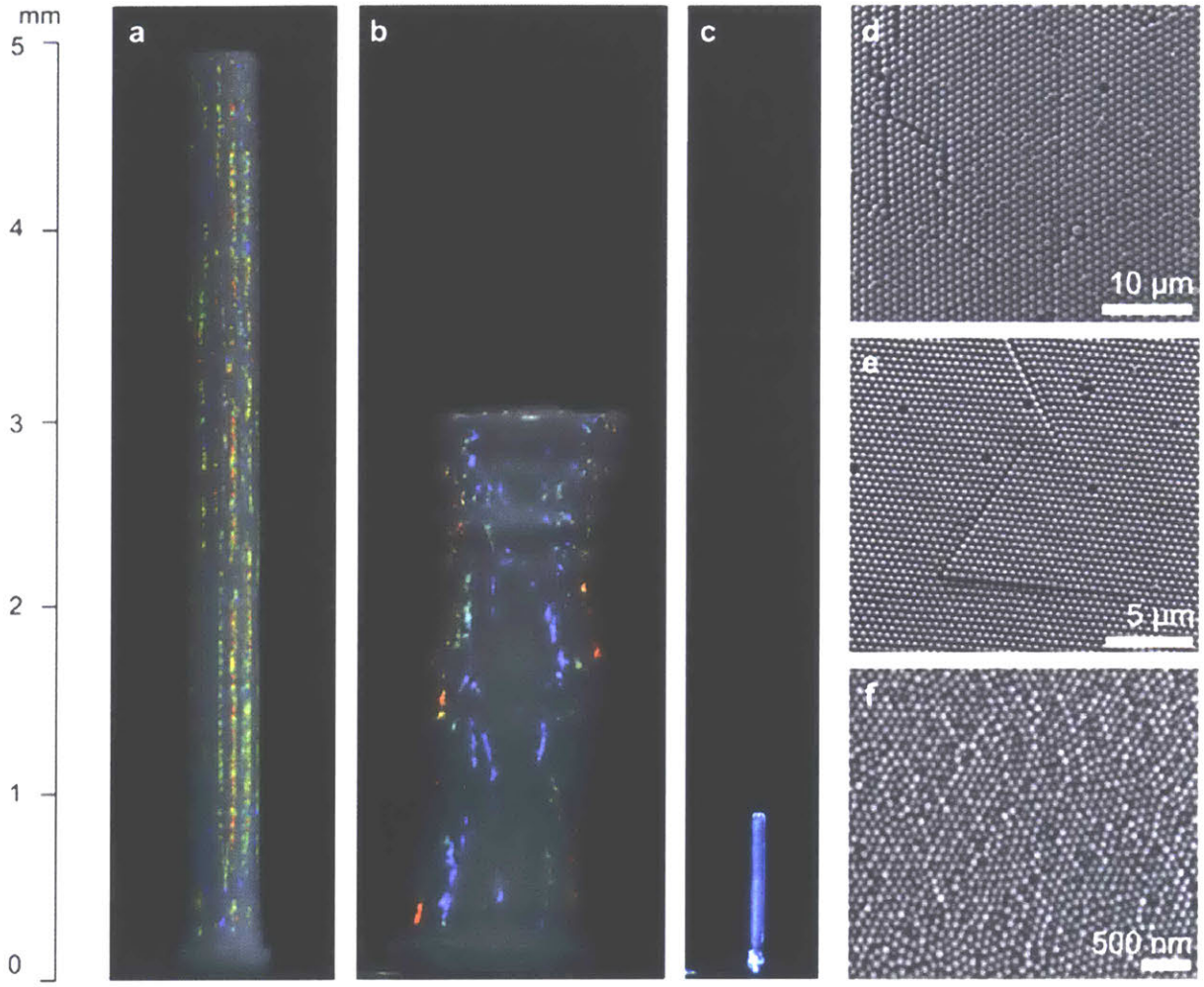

Figure 2.2. Exemplary millimeter-scale structures built by direct-write assembly. Optical and corresponding SEM images of vertical columns built from a,d) a = 500 nm polystyrene particles, b,e) a = 250 nm polystyrene particles, c,f) a = 88 nm polystyrene particles.

As a first model system, we built colloidal towers using aqueous solutions of spherical polystyrene particles with radius ranging from a = 44 nm to a = 500 nm, at volume fraction $\phi_1 \approx$

0.025. The diameters of the resulting towers range from 50 μm to 1 mm, and the heights range from 1 mm to 1 cm, as shown in Figure 2.2 and Figure S2.4.

Throughout this wide range of dimensions, colloidal towers built by direct-write assembly are polycrystalline, though the packing of the smallest particles (a = 44 nm) is less ordered due to broad size dispersity (CV = 11%). X-ray microscopy permits non-destructive imaging of the particle arrangement within the structures. A three-dimensional reconstruction of an exemplary tower reveals an average grain size of approximately 20 μm (Figure 2.1c). A cross sectional slice of the imaged volume reveals grain boundaries, voids, and dislocations (Figure 2.1d), as can be expected within colloidal crystals.[47]

2.2 Kinetics of assembly

In situ video microscopy reveals that the colloidal towers precipitate wet, i.e., saturated with water between the particles, and then dry at a distance L below the bottom of the liquid bridge. The "wet" and "dry" sections, as well as a drying front in between, are easily distinguishable based on optical appearance – the wet section is darker than the dry section, and the drying front is opaque white (Figure 2.3a). The precipitation of the solid structure occurs by an influx of water and particles through the bottom of the liquid bridge. The water flowing into the wet section compresses the particles downward while the capillary pressure at the section's outer surface, due to the liquid's surface tension γ, provides lateral constraint. This capillary pressure drives water through the wet section to its outer surface, where the water evaporates. The water experiences a resistance to flow due to its viscosity μ as it travels in the interstitial spaces

between the particles packed at volume fraction ϕ_2, driven locally by the pressure gradient ∇P. In all our experiments, the Reynolds number is $\mathrm{Re} \leq 10^{-3}$, based on the dispense rates and particle sizes.

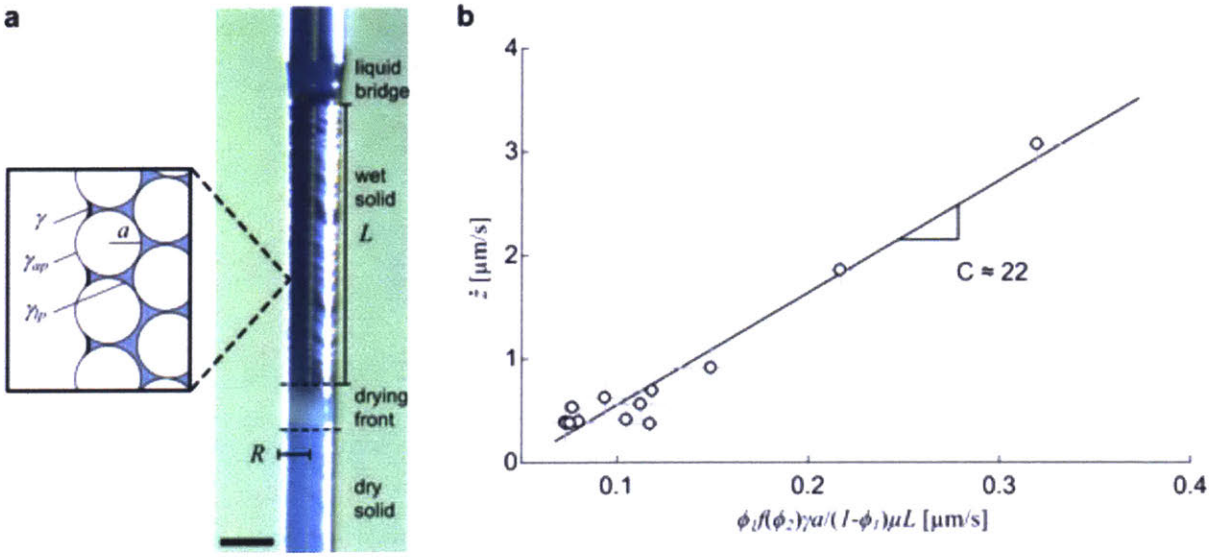

Figure 2.3. Scaling of build rate in direct-write colloidal assembly. a) The structure (radius R) precipitates wet, and evaporation occurs from the surface of the wet section of length L, which drives an influx of liquid and particles through the liquid bridge. Scale bar: 200 μm. The inset illustrates particles of radius a near the surface of a wet region of the solid, and the surface tension quantities on the air-liquid (γ), air-particle (γ_{ap}), liquid-particle (γ_{lp}) interfaces. b) The steady state build rate $\dot{z}$ follows a simple scaling relationship with γ, a, L, the volume fraction of particles in the suspension ϕ_1, volume fraction of particles in the solid ϕ_2, and viscosity of water μ. Calculation of error bars is detailed in Supporting Information.

A quantitative understanding of the factors governing the build rate in direct-write assembly was obtained by performing a series of experiments where vertical structures of constant radius R were built with various particle radius a. Experiments are performed with polystyrene spheres suspended in water, where the polystyrene particles occupy volume fraction $\phi_1 \approx 0.025$.

For steady build of a vertical structure with uniform radius R, the wet length L is constant and the speed at which the substrate is withdrawn from the needle to build the structure $\dot{z}$ relates to the above-mentioned quantities as follows. The energy change dewetting a particle of surface area A_p is $u = (\gamma_{ap} - \gamma_{lp})A_p = \gamma \cos\theta \, A_p$ as its surface energy changes from liquid-particle γ_{lp} to air-particle γ_{ap}; here Young's law $\gamma_{ap} - \gamma_{lp} = \gamma \cos\theta$ defines the contact angle θ. The free energy change associated with dewetting a differential layer dz of the structure is therefore $dF = (u\phi_2/V_p)\pi R^2 dz$, V_p being the volume of a particle, and ϕ_2 being the volume fraction of particles in the wet solid. The pressure difference P_F of the liquid relative to atmosphere at the drying front is the negative change in free energy per cross section area $P_F = -(dF/dz)/\pi R^2 \sim -\phi_2 \gamma \cos\theta \, /a$.

We assume that the average flux of water q through the liquid bridge into the structure is governed by Darcy's law $q = (-k/\mu)\nabla P$, where the permeability of the structure k must, on dimensional grounds, be of the form $k = f(\phi_2)a^2$ and using the Kozeny-Carman equation [48] we approximate $f(\phi_2) \approx (1-\phi_2)^3/45\phi_2^2$. The pressure at the top of the structure is set by the capillary pressure of the liquid bridge $P_B \sim \gamma/R$, so $\nabla P \sim \frac{P_F - P_B}{L} \sim -\phi_2 \cos\theta \frac{\gamma}{La}$ by $\frac{P_F}{P_B} \sim \frac{R}{a} \gg 1$, and the build rate of the structure is therefore

$$\dot{z} \approx C \frac{\phi_1 f(\phi_2)\gamma a}{(1-\phi_1)\mu L} \qquad \text{Eq. 2.1}$$

Mass balance gives $q = \dot{z}\phi_2(1-\phi_1)/\phi_1$, $\phi_2 \approx 0.73$ based on X-ray microscopy measurements, and the proportional factor C includes θ (Supplementary Information).

Experimentally, $C \approx 22$ for all structures we built to heights $\geq L$ (Figure 2.3b). Equation 2.1 fits the data well, for a plurality of experiments with particle sizes ranging from $a = 44$ nm to $a = 110$ nm, resulting in a growth rate of ~0.5 – 3 μm/s. The build rate is inversely proportional to L because a shorter L means a greater pressure gradient and therefore greater flow by Darcy's law. The intuition that a longer wet section implies a faster build rate – that is, more surface area implies greater total evaporation and greater flow rate through the needle – is true only for structures built to heights shorter than L.

2.3 Freeform assembly

Complex freeform shapes can be built by coordinating additional degrees of freedom in the substrate's motion. For example, to form a helical structure, we coordinated the curvilinear rate of growth of the structure with the rotational and vertical motion of the substrate, as illustrated in Figure 2.4b. Here, a slanted-tip needle was used so that the liquid bridge would be oriented in the direction of crystal growth, as shown in Figure S2.6. The helical structure shown in Figure 2.4b has a pitch of 2.28 mm, circular radius of 0.34 mm, and is built from polystyrene particles with a = 44 nm.

2.4 Optical properties

Colloidal assemblies exhibit a diverse range of optical phenomena depending on their crystalline order. Well-ordered colloidal crystals are known to have photonic stopbands that enable the spectrally-selective reflection of light,[49,50] which gives a sparkling, iridescent appearance. The spectral position of the stopband mainly depends on the particle size and packing.[18] Conversely,

amorphous colloidal structures made by frustrating the assembly process[51] can exhibit non-iridescent structural colors, and the building blocks can be chosen to exploit absorption and interference effects synergistically.[52–54] Such ordered and disordered materials can form the basis for lasers, optical sensors, waveguides, and structural color displays.[55]

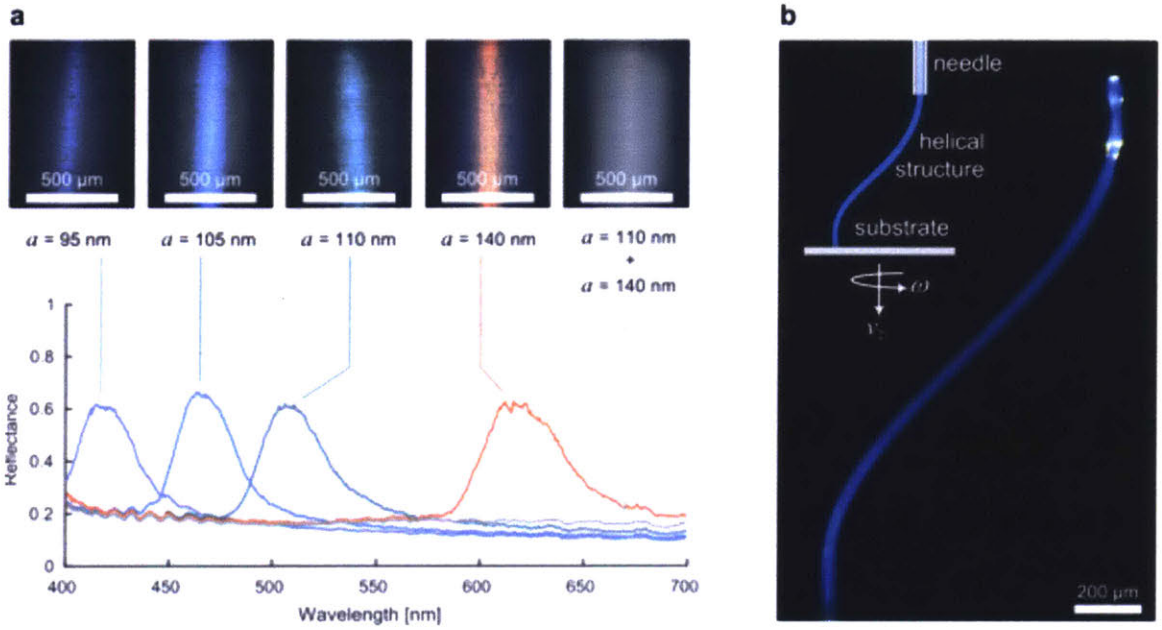

Figure 2.4. Tailoring the properties of freeform colloidal structures by choice of particle size, build trajectory, and material. a) Freestanding cylindrical colloidal crystals with structural colors tunable by the radius of polystyrene particles (increasing from left to right), and corresponding reflectance spectra measured from the surface of each of the above structures. b) Optical image of a freestanding helical shaped structure, with circular diameter of approximately 0.67 mm and height of approximately 1.1 mm. The helical structure was built by simultaneously rotating (ω) and lowering (v_z) the substrate.

Direct-write assembly therefore provides a route to build macroscale colloidal structures with tailored optical properties, such as by selecting the particle size and controlling the packing within the structures. The ordered crystalline arrangements observed in the interior of our structures (Figure 2.1c and Figure 2.1d) suggest that they should exhibit structural coloration due to Bragg reflection occurring in the visible range of light. Structures made from monodisperse

particles of different size should therefore reflect different colors when illuminated with white light. Upon white light illumination, towers formed from particles of radius a = 95 nm, 105 nm, 110 nm, and 140 nm appear violet, blue, green, and red, respectively, as shown in Figure 2.4a. Reflectance spectroscopy reveals that the towers exhibit Bragg reflection peaks at λ = 420 nm, 460 nm, 510 nm, and 620 nm, respectively. In towers built from suspension with mixed particle sizes (here, an equal proportion of a = 110 nm and a = 140 nm particles; Figure 2.4a), the slight mismatch in particle size leads to frustrated particle packing and no long-range order. Therefore, under white light illumination in an optical microscope, the mixed-particle towers appear whitish and reflectance spectroscopy shows that all visible wavelengths have been reflected at a uniform level of ~0.2. The emergence of structural colors from ordered assemblies of particles, and the tuning of particle size to modify the spectral position of the reflectance peak, is a well-established strategy for planar colloidal crystals, which we have now demonstrated can be realized in complex, macroscale shapes via direct-write assembly.

2.5 Cracking control

Interestingly, we find that cracks may be present or absent in these freestanding structures depending on structure dimensions and particle size. The established treatment of a liquid-saturated colloidal solid is as an elastic continuum material that, when compressed by a capillary pressure at its outer surface, shrinks volumetrically during drying in a manner analogous to thermal contraction[56]. In drying colloidal films, a no-slip boundary condition with the underlying substrate is said to be responsible for generating tensile stress in the film, causing cracks[57]. However, the external surfaces of our particle structures are free boundaries; in fact, we have

built structures with cracks only at the top. The presence of cracks is therefore curious from this point of view and suggests a different physical explanation.

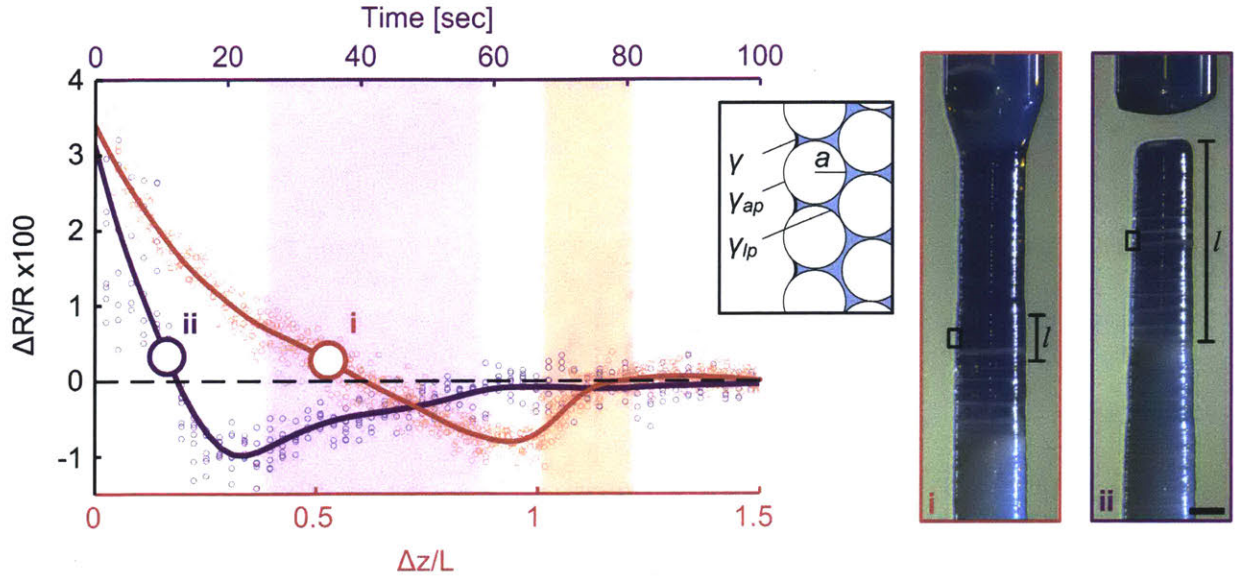

Figure 2.5. The radial change of a thin cross-section layer of the structure ΔR, relative to its final radius R when dry, exhibits the same contraction and expansion behavior in two cases: (**i**) during construction, as a function of the layer's distance below the bottom of the liquid bridge Δz; (**ii**) at termination, as a function of time. Cracks appear in the sections labeled by l, which for both curves correspond to $\Delta R \approx 0$ (large white-filled markers) ahead of the drying front (shaded regions); the data points are an aggregate of 10 layers that each develop a crack and the solid lines are moving averages. All measurements are from the same structure, a = 44 nm (additional measurements in Supplementary Fig. S2.8). Scale bar represents 500 μm

The cracks vary in width and orientation (Fig. 2.6a, Fig. S2.6); however, we generally observe that the widest cracks are preferentially circumferential and typically visible *in situ* with the video microscope cameras (Fig. 2.5). These circumferential cracks appear in the wet section just above the drying front during construction (Fig. 2.5(i)), and throughout the entire wet section during evaporation of the remaining liquid after construction is terminated (Fig. 2.5(ii)). In both cases, the cracks appear when the structure's radius constricts to $\approx R$.

At the moment these cracks occur, we estimate the capillary pressure exerted on the particles is primarily borne by particle-particle contacts because other forces experienced by the particles – namely viscous, electrostatic, Van der Waals, and thermal – are smaller by at least an order of magnitude (Figure S2.7). Because the radius is $\approx R$, as a lowest order approximation we assume the structure here is unstrained and ignore the elastic strain energy in the particles as if they are hard spheres. This leaves only energy quantities related to the liquid and wetting of the particles, and we proceed by considering the cylindrical section of the structure with radius $\approx R$ and height l just before it initiates a crack; l will be interpreted later in the context of building a structure and at termination of build. This section comprises contacting particles saturated in stationary water at uniform pressure difference P from atmosphere due to the microscopic water menisci wetting the particles at the section's outer surface as depicted in Fig. 2.5 (inset); the surface energies γ, γ_{ap}, γ_{lp} correspond respectively to surface areas A, A_{ap}, A_{lp}.

In a differential time interval, a differential volume of water dV evaporated from the section's outer surface in turn may deform and recede the menisci between the particles so that the differential change in free energy for the section is $dF = -PdV + \gamma dA + \gamma_{lp} dA_{lp} + \gamma_{ap} dA_{ap} = -PdV + \gamma\left(dA + \cos\theta dA_{ap}\right)$. This is simplified again using Young's law and recognizing that $dA_{ap} = -dA_{lp} > 0$ because the water may recede to expose more air-particle surface at the expense of liquid-particle surface.

If the particles are immobile, then the water is in equilibrium and $dF = 0$, so that $-PdV + \gamma\left(dA + \cos\theta dA_{ap}\right) = 0$. Hence, the energy expelled with the evaporated volume, i.e.,

$-PdV < 0$ because $P, dV < 0$, is equal to the energy acquired creating surface area by deforming and receding the menisci between the particles. By a scaling argument (Supplementary Information), we may substitute $-PdV \to -c_1 \gamma A_l$ and $\gamma(dA + \cos\theta dA_{ap}) \to c_2 \gamma A_l$, which recasts the equilibrium equality as $-c_1 \gamma A_l + c_2 \gamma A_l = 0$ where $c_1 / c_2 = 1$; $A_l = 2\pi Rl$ is the section's outer surface area and the factors c_i are positive functions of geometry and θ.

The particles cannot, in actuality, all be immobile because some must separate to form a crack. If the particles have a collective mobility such that within the differential time interval they may rearrange to occupy a slightly smaller overall volume – a reasonable supposition based on Fig. 2.5 – this lowers the free energy of the section because not all the energy expelled in the evaporated volume is consumed as surface energy in deforming and receding the water menisci. Here $-c_1 \gamma A_l + c_2 \gamma A_l \leq 0$ and therefore $c_1 / c_2 \geq 1$, where the ratio c_1 / c_2 is a metric that indicates the amount of particle mobility in the sense just described.

For initiation of a crack to be energetically favorable, the same inequality must be satisfied including an additional consumption of surface energy on a characteristic area A_δ associated with initiating the crack; this gives $-c_1 \gamma A_l + c_2 \gamma A_l + c_\delta \gamma A_\delta \leq 0$, where the factor c_δ on the crack initiation term is similar to c_2. It must be that $A_\delta \sim a^2$ because a crack can only propagate if the section can at least overcome an energy barrier on the order of bringing a particle to or from its outer surface. Rewriting the inequality as $c_2 (c_1 / c_2 - 1) / c_\delta \geq A_\delta / A_l$, evidently for a given particle size cracks will appear if the surface area of the section A_l is made large enough and only for

immobile particles, i.e., $c_1 / c_2 = 1$, is cracking impossible. Conversely, for a given particle size the section may be crack free provided its surface area is sufficiently small. Succinctly, the section cracks when satisfying

$$g \geq \frac{a^2}{Rl}. \qquad \text{Eq. 2.2}$$

The parameter g depends on contact angle θ, particle mobility c_1 / c_2 and geometry, where $g \geq 0$ and $g = 0$ for immobile particles. In this way, the section can develop a crack despite being compressed by a uniform capillary pressure. This result is a ratio of length scales due to having only considered the dominant wetting energy terms.

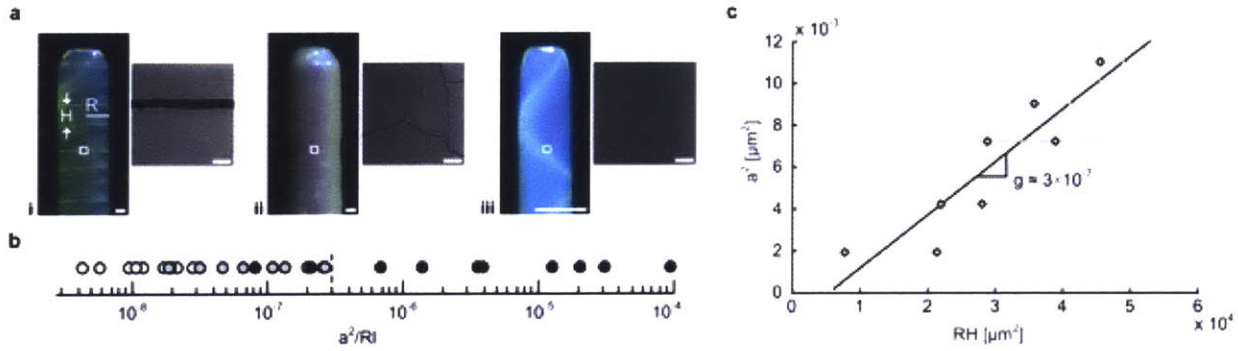

Figure 2.6 Conditions for crack development. (a) Optical images of the top section of particle structures exhibiting (i) wide circumferential cracks, (ii) shallower cracks in arbitrary orientations, and (iii) no cracks, where the structure internally reflects the illumination incident from the top right. (b) For all structures we built, the dimensionless number a^2/Rl demarcates the three cases, corresponding to (i) white, (ii) grey, and (iii) black data points. (c) Measurements of the spacing H between circumferential cracks provides an upper estimate on a^2/Rl for the onset of cracking, denoted by the dashed line in (b). Scale bars represent 50 μm for the optical images and 5 μm for the SEM images.

The height l corresponds to the section of the particle structure with its radius constricted to $\approx R$. According to Fig. 2.5, during construction this is the section with some height $l < L$ just above the drying front (Fig. 2.5(i)) and at termination it is the section $l \approx L$ at the top (Fig. 2.5(ii)); for

structures built to heights $< L$ due to the limits of our experiment apparatus, at termination, l is the structure's height. According to Eq. 2.2, this means that cracks are most likely to initiate at the top of the structure, and L determines the maximum likelihood of a structure initiating a crack. For all structures, the quantity $a^2/Rl \approx 10^{-7}$, using the maximum values for l, i.e., l equals L or for shorter structures their height, demarcates those with and without cracks after drying (Fig. 2.6b). For the subset of structures with wide circumferential cracks, the sections in between the cracks have area $A_H \sim RH$ (Fig. 2.6a left) which approximately saturate Eq. 2.2, and we find $g \approx 3\times10^{-7}$ (Fig. 2.6c). The measurements of H were taken only from the top parts of the structures where the cracks formed at termination throughout the remaining wet section of length $\gg H$, which ensures an approximate upper estimate for g (Fig. 2.6b, dashed line).

The fact that we can identify an approximately constant value for g indicates that the particle mobility c_1/c_2 is approximately constant at the moment of crack initiation, and $g \ll 1$ presumably indicates c_1/c_2 is nearly unity which agrees with our picture of the particles just contacting one another in their close-packed arrangement when the section's radius is $\approx R$. Interestingly, there is a transition between shallower cracks in arbitrary orientations (Fig. 2.6b, grey circles) and wide circumferential cracks (Fig. 2.6b, white circles) about $a^2/Rl \approx 2\times10^{-8}$; this perhaps indicates that particle mobility becomes directional, although the details of crack propagation are beyond our free energy argument for crack initiation. Combining Eq. 2.1 and Eq. 2.2, structures built at rates $\dot{z} \gtrsim \frac{gC\phi_1 f(\phi_2)\gamma R}{\mu a}$ are crack free. The construction of crack-free structures is important to future bulk optical[58,59], mechanical[60–62] and thermal[63,64] characterization of colloidal materials.

2.6 Conclusions

We have demonstrated the combination of evaporative self-assembly with a direct-write process, enabling the freeform construction of macroscale colloidal crystalline solids for the first time. Looking forward, we anticipate this technique can build colloidal materials with tailored optical, [58,59] mechanical [60,65] and acoustic [66] properties, and many other interesting emergent characteristics. Our technique may also serve as a model system to investigate meniscus-confined colloidal epitaxy [67], and to build macroscale structures with a single crystallographic orientation. Direct-write assembly may also be applied to particles with even smaller sizes and from a wide range of materials, thereby combining materials design via self-assembly with the versatility of direct-write 3D printing.

2.7 Experimental details

Liquid dispensing apparatus. We built particle structures using a custom-fabricated benchtop system that comprises a glass syringe and needle mounted vertically above two parallel aluminium plates that create a uniform temperature environment for the particle structures (Figure S2.1). The needle passes through a hole in the top plate, which we machined in half to expedite preparation for experiments, and the substrate rests on the bottom plate as shown. The top and bottom plates are uniformly heated by thermoelectric chips (standard square dimensions, Custom Thermoelectric), and the plate temperature is measured by embedded thermocouples (K-type) which feed to a temperature controller (PTC 10, Stanford Research Systems). The thickness of the top plate was chosen so that the particle suspension dispensed through the needle heats to the temperature of the plate while transiting its thickness for the dispense rates used in

experiments. The dispense rate (~0.01 μl/s) and translational motions of the substrate relative to the needle (~1 μm/s) are motor controlled (0.078 μm step size: M-229.26S, Physik Instrumente), and the motors are controlled manually using joysticks (Pro Flight Throttle Quadrant from Saitek); we found this to be the most convenient way to match the structure's evaporation and build rate, and enable fine adjustments. The motions of all the actuators are recorded for the duration of each experiment. Depending on the volume capacity of particle suspension required to build the structures, we used syringes with piston diameters [2.30, 3.26] mm which respectively correspond to dispensing precisions of [0.3, 0.7] nl. The dispensing needles were made of glass for smaller sizes, ID/OD = [50/80, 82/120, 200/250, 400/500, 600/700] μm (Hilgenberg), and made of stainless steel for the largest size ID/OD = 0.84/0.127 mm. The diameter of the structures we built were approximately the needle ID. We observe building of the particle structures *in situ* with two video microscope cameras. One views the needle orifice and liquid bridge with a 3X objective (Mitutoyo Telecentric 3X Objective, Edmund Optics stock # 56-985) and 5 megapixel CCD (DCC 1645C, Thorlabs). The other views the needle and entire structure with a 1X objective (Mitutoyo Telecentric 1X Objective, Edmund Optics stock # 56-984) and 10 megapixel CCD (EO-10012C, Edmund Optics). For each objective, the needle and structure are backlit with a telecentric lens (Techspec Telecentric Backlight Illuminator, Edmund Optics), and LED spotlights (Amscope LED-6W) are used to illuminate the front side of the structure facing the objectives. The video feeds from both CCD's are simultaneously recorded and displayed on a computer screen – we use the onscreen view to monitor the building of the structure and adjust the dispense rate and stage motion.

Microstructural characterization. Imaging the surface of the structures was performed with a Zeiss Merlin SEM in high efficiency secondary electron imaging mode, at an acceleration voltage of 1 kV and probe current of 80 to 100 pA. X-ray Microscopy of the interior of the structure was performed courtesy of Dr. Steve Kelly of Carl Zeiss X-ray Microscopy, Inc. Zernike phase contrast images were acquired with a Zeiss Xradia 810 Ultra system, at photon energies of 5.4 keV and a total scan time of 25 hours. The field of view for data acquisition was 65 μm × 65 μm and the voxel size was 64 nm. Three-dimensional reconstruction of the image slices was performed with ORS Visual SI Advanced software.

Reflectance measurements. We constructed vertical particle structures, broke them at the base, and mounted them on a flat adhesive substrate. The surface of the structure was illuminated through a microscope objective (Olympus, 20× objective lens, 0.4 N.A.) which also collected the light reflected from the sample. The reflected light passed through an optics train coupled to an optical fiber (Ocean Optics; 100-μm core) and was analysed with a grating spectrometer (Ocean Optics; Maya Pro) controlled via the software IGOR.

Surface tension estimates. Using our liquid dispensing apparatus, we drew particle suspension into a needle (ID/OD: 0.6 / 0.7mm) and syringe from the supplier's bottle. We then dispensed the suspension through the needle (0.0417 mm^3/s) and video-recorded the growing pendant drop, and used the video frame before the drop fell from the needle to calculate the suspension's surface tension by the pendant drop method. The vertical force balance on drop comprises gravitational F_g, surface tension F_γ, capillary pressure F_p, and head pressure F_h components:

$0 = F_g + F_\gamma + F_p + F_h = -\rho V g + \gamma 2\pi R - \frac{2\gamma}{r}\pi R^2 + \rho g h \pi R^2$. The expression for the surface tension is therefore $\gamma = \frac{\rho g\left(V - h\pi R^2\right)}{2\pi R\left(1 - R/r\right)}$.

Here, r is the mean radius of the droplet, R is the radius of the neck of the droplet pinned to the needle's OD, h is the distance from the needle to the centroid of the droplet, ρ is density of the droplet, and g is gravitational constant, and V is the volume of the droplet determined by image analysis.

The surface tension of particle suspensions from Polysciences was measured to be 73.0 ± 2.0 mN/m, equal to pure water. However, the surface tension of particle suspensions from Bangs Laboratories was measured to be 56.6 ± 1.1 mN/m. The lower surface tension is due to the residual surfactants, typically sodium dodecyl sulfate (SDS), from the particle synthesis process. According to data from Lin et al. [68], a surface tension of 55 mN/m of SDS solution corresponds to a surfactant concentration of 2×10^{-7} mol/cm^3. During construction of a particle structure, these surfactants are further concentrated by the evaporation of water. Approximately 98% of the volume of the particle suspension is evaporated in the tower building process, and we estimate the surfactant concentration increases to about 3×10^{-5} mol/cm^3, which exceeds the critical micelle concentration of 6.7×10^{-6} mol/cm^3. Above the critical micelle concentration, the surface tension is 38.0 ± 1.7 mN/m. Therefore, we assume the surface tension of the liquid during building of a structure is 38.0 ± 1.7 mN/m for particle suspensions from Bangs Laboratories and

73.0 ± 2.0 mN/m for suspensions from Polysciences. We use this assumption when plotting the data points in Figure 2.3b.

Radial change ΔR measurements. The radial changes of the structure were measured by image analysis of videos, implemented in Matlab. A region of interest (≈ 1.0 mm × 0.10 mm, corresponding to 600 pixels by 60 pixels) was defined by its fixed distance from the substrate. Video frames were binarized using Sobel edge detection and the radial change was measured from the number of pixels between the detected edges. The reported radial change is the average radial change across the region of interest.

Zeta potential measurement. Electrophoretic mobility of particles μ_e was measured by phase analysis light scattering (ZetaPALS Potential Analyzer, Brookhaven Instruments). Each measurement was collected from 3 runs of at least 20 cycles with samples at room temperature T ≈ 25 °C. The particles are suspended in deionized water at PH 7, i.e., 10^{-7} M ion concentration. The Debye-Huckel parameter is $\kappa = 10^{-6}$ [m^{-1}], so κa <5 for our particles and the zeta potential is calculated by $\zeta = \frac{3}{2}\frac{\mu\mu_e}{\varepsilon}$, where μ and ε are the dynamic viscosity and dielectric permittivity of water, respectively. Surfactant is present in some of our particle suspensions sourced from one particular supplier (Bangs Laboratories), however we ignore this in estimating κ. Zeta potential measurements for each particle size are given in Table S2.1.

Particle volume fraction estimates in the structure. During construction, a layer of the particle structure contracts its radius as it transits the wet section, which then expands upon passage

through the drying front. We observe that the final radius R of the structure once it is dry corresponds to a close-packed arrangement of particles based on our SEM images of the particle structures after they are constructed. If we further assume that the particles remain in approximately the same arrangement to one another once precipitated from the bottom of the liquid bridge and that the change in the structure's radius ΔR reflects a uniform volumetric change, then the expressions for the space s between the particles and particle volume fraction ϕ_2 as a function of $\Delta R/R$ are:

$$s(\Delta R/R) = 2a\frac{\Delta R}{R} \qquad \phi_2(\Delta R/R) = \frac{\phi_2^0}{1+\Delta R/R};$$

ϕ_2^0 is the close-packed particle volume fraction when the structure is dry, as observed in our SEM images. It is in the range $\phi_2^0 \in [\approx 0.64, 0.74]$ based on the ordering of the particles; $\phi_2^0 \approx 0.64$ corresponds to random close packing and $\phi_2^0 = 0.74$ corresponds to face-centered or hexagonal close packing. We measure $\Delta R/R \approx 0.01 - 0.05$, so the initial space between the particles is a few percent of their radii.

Estimates of uncertainty. For all plots, the quantity plotted on each axis, say $p(x_i)$ which is a function of the parameters x_i, we estimate to have uncertainty $\Delta p(x_i) = \sum \left| \Delta x_i \, \partial_{x_i} p(x_i) \right|$. This is just the magnitude of each term in the total differential for $p(x_i)$. The uncertainty estimates for parameters Δx_i are given below for each plot.

In Fig. 2.3, the vertical axis quantity is $\dot{z}$ and we take $\Delta \dot{z}$ to be the difference between the steepest and least steep slopes in plots of stage position z vs time; measurements of stage position

were obtained by image analysis of the *in situ* optical microscopy videos. The horizontal axis quantity is $\phi_1 f(\phi_2)\gamma a/(1-\phi_1)\mu L$. According to the manufacturers for the particle suspensions $\Delta\phi_1 \approx 0.01$ and $\Delta\phi_2 \approx 0.001$ based on the X-ray microscopy. For particle suspensions from Polysciences Inc., $\Delta\gamma = 2\text{mN/m}$ is the standard deviation of the surface tension measurements we performed by the pendant droplet method; for particle suspensions from Bangs Laboratories, we use $\Delta\gamma = 1.7\text{mN/m}$, according to measurements performed by Lin et al [68]. Δa was taken to be the standard deviation of particle radius as reported by the manufacturers of the particle solutions. $\Delta\mu$ was taken as 2.7 μPa, 2.0 μPa, 1.8 μPa, for temperatures of 50 °C, 70 °C, and 80 °C, respectively, as reported in reference data by Kestin et al [69]. ΔL is the length of the drying front located at the end of the wetting length, measured by image analysis of the *in situ* optical microscope videos.

In Fig. 2.6c, the vertical axis quantity is a^2 and the horizontal axis quantity is RH. Δa is the standard deviation provided by the manufacturer. ΔR is the difference between the largest and smallest radius of a given particle structure, and ΔH is the standard error of the spacing between the cracks. ΔR and ΔH were measured by in situ optical microscopy.

2.8 Supporting Information

Forces acting on a particle arriving at the top of a precipitating structure

During construction, a particle arriving at the top of the structure experiences a downward Stokes force F_μ from the water flowing past, as well as a repulsive, upward electrostatic double layer force F_ζ from the other particles. The density of the water is $\rho \approx 10^3$ kg/m^3, the dynamic viscosity of the water is $\mu \approx 4.04 \times 10^{-4}$ Pa.s, we calculated the average speed of the water traveling through the structure to be $U \approx 0.03-3$ mm/s, the permittivity of the water is $\varepsilon \approx 5.66\times10^{-10}$ F/m, and the pH of the water is 7, i.e., the ion concentration is $\approx 10^{-7}$M. The heated plates were maintained at constant temperature in the range 60–80 °C depending on the experiment. The Reynolds number is $\mathrm{Re} = \rho Ua/\mu \approx 10^{-6}-10^{-3}$ in our experiments. As a simple estimate, $F_\mu/F_\zeta \sim \mu aU/\varepsilon\zeta^2$ and approximate values of this quantity are listed in Table S2.1 for each particle size we used. $F_\mu/F_\zeta < 1$ indicates that initially there is space between the particles.

Scaling argument for build speed

Underlying assumptions. The underlying assumption for the steady-state construction of a structure, i.e., for constant build rate $\dot{z}$, radius R and wet length L, is that there is similarity in the physical picture [70]. Specifically, the curve representing the pressure drop in the wet section as a function of the distance from the bottom of the liquid bridge up to the drying front, i.e., $P(\Delta z)$ for $\Delta z \in [0, L]$, is the same when scaled by the maximum pressure drop P_F and by the wet length L. This requires a similarity in the rate of evaporation from the surface of the structure as a function of the distance from the bottom of the liquid bridge up to the drying front. Presumably, the rate of evaporation is limited by the diffusion of water vapor into the air near the liquid bridge and limited by the restriction to flow through the network of particles near the drying front [71,72].

Provided this similarity, $\nabla P \sim P_F/L$ determines the scaling for the average flux of water through the needle into the particle structure according to Darcy's law $q \sim -k/\mu(P_F/L)$. The linear relationship we find in Fig. 2.3b indicates that this assumption of similarity is approximately correct, at least within the measurement precision and parameter range of our experiments.

Driving pressure. As a differential layer of the particle structure with volume $\pi R^2 dz$ transitions across the drying front from wet to dry, the change in surface energy for each particle in this volume is $u = \left(\gamma_{ap} - \gamma_{lp}\right) A_p = \gamma \cos\theta A_p$, where $A_p = 4\pi a^2$ is the surface area of one particle. The number of particles in the differential layer is $n\pi R^2 dz$, n being the number density of particles, and the relationship between volume fraction and number density is $\phi_2 = nV_p$, where $V_p = \frac{4\pi}{3} a^3$ is the volume of one particle. The corresponding change in free energy for differential layer is

$$dF = un\pi R^2 dz = \left(3\phi_2 \gamma \cos\theta / a\right) \pi R^2 dz ;$$

we ignore the changes in ϕ_2 across the drying front which are at most ~1% (Fig. 2.5), as well as the minimal liquid content that may remain in the dry section. The driving force acting to rewet the particles is $-dF/dz$, and so the average driving pressure $P_{l'}$ across the structure's cross section area is

$$P_{l'} = -\left(dF/dz\right)/\pi R^2 = -3\phi_2 \gamma \cos\theta / a ;$$

this is also the pressure of the liquid at the drying front relative to atmosphere.

Alternatively, starting from the Laplace capillary pressure equation $P = -\gamma \nabla \cdot \hat{n}$, $\hat{n}$ being the unit normal for the liquid menisci surface, the maximum curvature the liquid menisci can attain between the particles is $\sim 1/a$, so $P \sim -\gamma / a$. The additional dependency on contact angle and particle volume fraction is most easily obtained by the free energy consideration given above.

Mass balance. During building of a structure, a mass volume V_1 with particle volume fraction ϕ_1 inside the needle eventually becomes the mass volume V_2 with particle volume fraction ϕ_2 that is a layer if the dry part of the particle structure with radius *R* and height *z*. Both V_1 and V_2 contain the same number of particles, and the difference $V_1 - V_2$ is the amount of evaporated water V_{evap}. V_1 comprises water and particle mass volumes:

$$V_1 = \underbrace{\left(1-\phi_1\right)V_1}_{\text{water volume}} + \underbrace{\phi_1 V_1}_{\text{particle volume}} ;$$

V_2 similarly comprises water and particle mass volumes, where $\eta \in [0,1]$ is the fraction of the interstitial space between the particles that may retain water (presumably, η is nearly zero):

$$V_2 = \underbrace{\eta\left(1-\phi_2\right)\pi R^2 z}_{\text{water volume}} + \underbrace{\phi_2 \pi R^2 z}_{\text{particle volume}} .$$

Therefore the amount of evaporated water is:

$$\begin{aligned} V_{evap} &= V_1 - V_2 \\ &= \frac{\phi_2}{\phi_1}\pi R^2 z - \left(\eta\left(1-\phi_2\right)+\phi_2\right)\pi R^2 z && \text{... by } \phi_1 V_1 = \phi_2 \pi R^2 z \\ &= \frac{\phi_2}{\phi_1}\left(1-\phi_1\right)\pi R^2 z && \text{... by assuming } \eta = 0 \end{aligned}$$

The water flow rate through the needle and into the particle structure is the time derivative of V_{evap}, $\dot{V}_{evap}$. The water flux q, i.e., average flow rate per cross-sectional area, is therefore

$$q = \frac{\dot{V}_{evap}}{\pi R^2} \approx \frac{\phi_2}{\phi_1}\left(1-\phi_1\right)\dot{z} .$$

Permeability function. The Kozeny-Carman equation is approximate for ordered and random sphere packings, and therefore is appropriate to model the flow permeability through the polycrystalline particle structures:

$$k = f(\phi_2)a^2 \approx \frac{\left(1-\phi_2\right)^3}{45\phi_2^2} a^2 .$$

X-ray microscopy was performed on a section of a particle structure comprised of $a = 373$ nm particles, and the ORS Visual SI Advanced software was used to calculate a particle number density of 3.37 particles/μm^3, which corresponds to a volume fraction $\phi_2 = 0.73$. This is less than the close-packed fcc volume fraction due to grain boundaries and voids in the structure. It was not possible to X-ray smaller particles due to the resolution limits of the Zeiss Xradia 810 Ultra.

We use $\phi_2 = 0.73$ for all structures when plotting Fig. 2.3b. This is only an approximation. In reality, ϕ_2 varies a few percent based on the change in radius of the structure across the wet length (Fig. 2.5) and may also vary depending on the size of the polycrystalline domains which may vary depending on particle radius a.

Scaling argument for crack initiation

Simple example. Before discussing the particle structures, we provide an analogous example with simple and explicit calculations. Consider a rigid cylindrical shell with radius R and height l that has a square array of tangent circular holes of radius a covering its surface. The array of holes is oriented so that the number of holes stacked vertically is $l/2a$ and the number of holes stacked around the circumference of the cylinder is $2\pi R/2a$. Defining the cylindrical area $A_l = 2\pi Rl$, the total number of holes is $N = A_l/4a^2$. The volume inside the cylindrical shell is filled with a stationary liquid that is pinned to the holes and is at pressure difference P from atmosphere due to its surface tension γ. Considering only wetting energy terms in light of our dominant balance (Fig. S2.7), we ignore gravity and regard evaporation at the holes as simply the removal of liquid at constant temperature.

The liquid meniscus in each hole has the shape of the surface of a spherical cap defined by the hole radius a and cap height h. We consider the cap height to be on the order of a, and write $h = a\xi$ where ξ is a dimensionless proportional factor. The spherical cap's volume V_a, surface area A_a and radius of curvature r are

$$V_a = \frac{\pi a^3}{6}\xi\left(3+\xi^2\right), \qquad A_a = \pi a^2\left(1+\xi^2\right), \qquad r = a\frac{1+\xi^2}{2\xi};$$

and the capillary pressure difference across the meniscus is

$$P = -\frac{2\gamma}{r} = -\frac{\gamma}{a}\cdot\frac{4\xi}{1+\xi^2}.$$

Let a differential amount of liquid dV evaporate from the cylinder while the liquid menisci remain pinned to the holes of radius a. This in turn changes the surface area of the menisci by dA, and the change in free energy is:

$$\begin{aligned} dF &= -PdV + \gamma dA \\ &= -PNdV_a + \gamma N dA_a \qquad \text{... by } dV = NdV_a,\ dA = NdA_a \\ &= -PN\frac{\partial V_a}{\partial \xi}d\xi + \gamma N\frac{\partial A_a}{\partial \xi}d\xi \\ &= -\left(\xi\pi^2\gamma Rl\right)d\xi + \left(\xi\pi^2\gamma Rl\right)d\xi \\ &= 0 \end{aligned}$$

The interpretation of $dF = 0$ above is the following. Evaporating a volume of liquid at pressure removes energy, while the increase in surface area adds energy. These energy quantities balance and indicate that the system is in equilibrium. Moreover, $dF = 0$ is anticipated without calculation because a differential amount of liquid added to and subtracted from the cylinder oscillates each meniscus around a point of equilibrium.

The changes dV and dA occur concurrently in a differential window of time, so we expect these quantities can be parameterized by the same variable; here the natural choice is ξ. Thus for $dF = 0$, the differential $d\xi$ is unimportant and we can focus on the expression

$$0 = \underbrace{-\xi\pi^2\gamma Rl}_{\substack{\text{Energy released} \\ \text{by evaporation}}} + \underbrace{\xi\pi^2\gamma Rl}_{\substack{\text{Energy acquired} \\ \text{by creating surface area}}} .$$

We can also arrive at the above expression by recognizing the following scaling of terms, ignoring the differential $d\xi$ that is ultimately inconsequential: $P \sim -\gamma/a$, $N \sim A_l/a^2$, $dV_a \sim a^3$, $dA_a \sim a^2$; therefore $-PdV = -PNdV_a \sim -\gamma A_l$ and $-\gamma dA = -\gamma NdA_a \sim -\gamma A_l$. The expression for $dF = 0$ is therefore

$$0 = -c_1\gamma A_l + c_2\gamma A_l ;$$

we have introduced the factors c_i that are functions of geometry and $c_1 / c_2 = 1$. In this example $c_i = \pi\xi/2$. If we were to modify this example so that the liquid menisci may also de-pin and recede from the hole radius *a*, all the insights given above as well as the scaling of terms remains the same, however the coefficients c_i would be explicit functions of geometry and contact angle θ.

Particle structures. For the particle structures in our experiments, the water is in between particles of radius *a* as opposed to within holes of radius *a* in the above example. The geometry of the liquid menisci between the particles is more complicated, and the menisci may deform and recede between the particles, however the scaling of terms follows essentially the same argument as that given in the above example.

Consider a cylindrical section of a structure with radius *R* and height *l* as described in the main text; its surface has an area $A_l = 2\pi Rl$ and contains a total number of particles $N \sim A_l/a^2$. The change in free energy for the section is

$$\begin{aligned} dF &= -PdV + \gamma dA + \gamma_{lp}dA_{lp} + \gamma_{ap}dA_{ap} \\ &= -PdV + \gamma dA + \cos\theta\gamma dA_{ap}. \end{aligned} \qquad \text{...by} \begin{cases} dA_{ap} = -dA_{lp} > 0 \\ \gamma_{ap} - \gamma_{lp} = \gamma\cos\theta \end{cases}$$

The pressure difference of the liquid from atmosphere scales as $P \sim -\gamma/a$, and around each particle on the section's surface we may ascribe an evaporated volume $dV_a \sim a^3$ and changes in surface area quantities $dA_a \sim a^2$. This gives $dV = NdV_a \sim A_l a$ and $dA, dA_{lp}, dA_{ap} \sim NdA_a \sim A_l$. The expression for $dF = 0$ therefore becomes

$$0 = -c_1 \gamma A_l + \gamma c_2' A_l + c_3' \gamma \cos\theta A_l$$

$$= \underbrace{-c_1 \gamma A_l}_{\text{Energy released by evaporation}} + \underbrace{c_2 \gamma A_l}_{\text{Energy acquired by creating surface area}} \qquad \text{...by } c_2 = c_2' + c_3' \cos\theta$$

The proportional factors c_i here are functions of geometry and θ, and $c_1 / c_2 = 1$. Because we approximate the particles as hard spheres, the condition $c_1 / c_2 = 1$ physically corresponds to the particles being immobile. This is analogous to the cylindrical shell being rigid in the above example. The rest of the argument for crack initiation in the section follows from here in the main text.

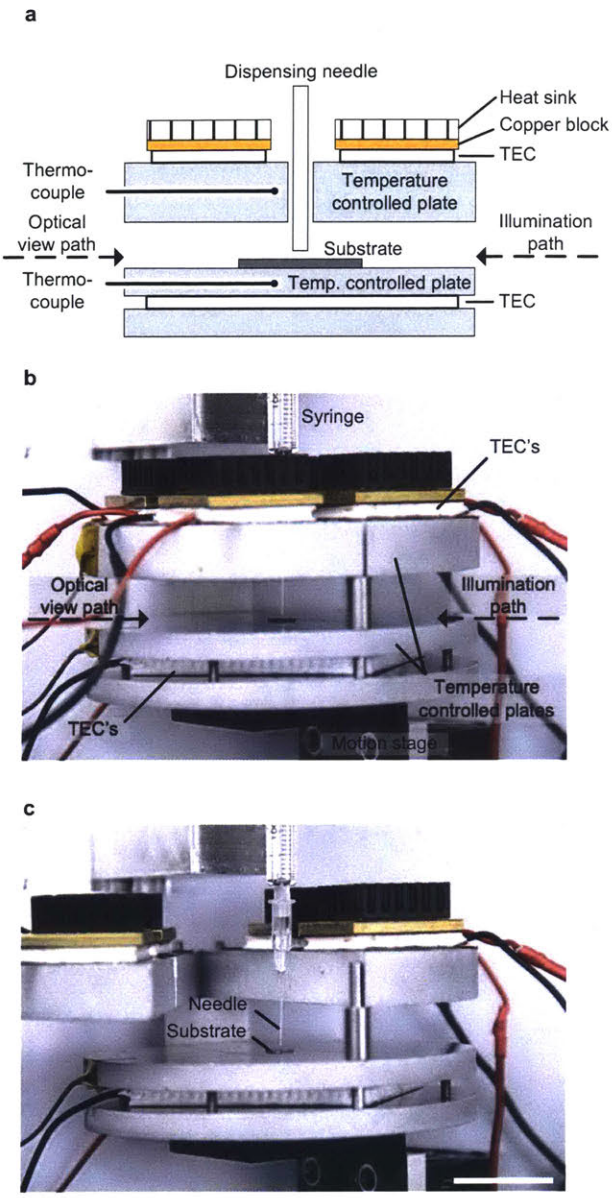

Figure S2.1 Experimental setup. (a) Schematic of experimental setup for construction of particle structures in a temperature controlled environment. (b) Configuration during experiments. (c) Top plate opened during experiment preparation, showing the protrusion of the needle through the top temperature controlled plate. Scale bar represents 25 mm.

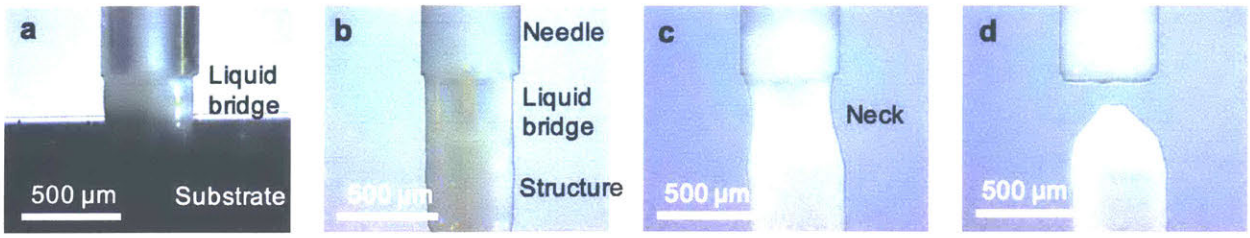

Figure S2.2. Video snapshots of a typical experiment. a) establishment of the liquid bridge, b) tower growth in progress, c) liquid bridge necking, d) a freshly pinched off structure.

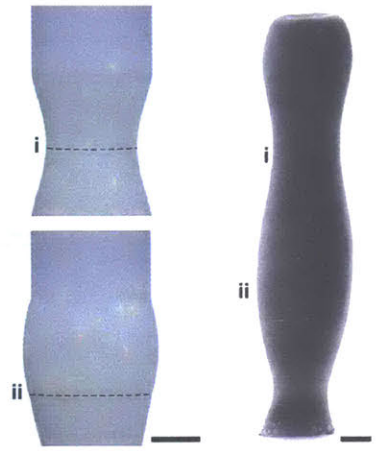

Figure S2.3. An hourglass structure built by (i) constricting and (ii) bulging the liquid bridge. The dotted line indicates the interface between the structure and the liquid bridge. Scale bars: 200 µm.

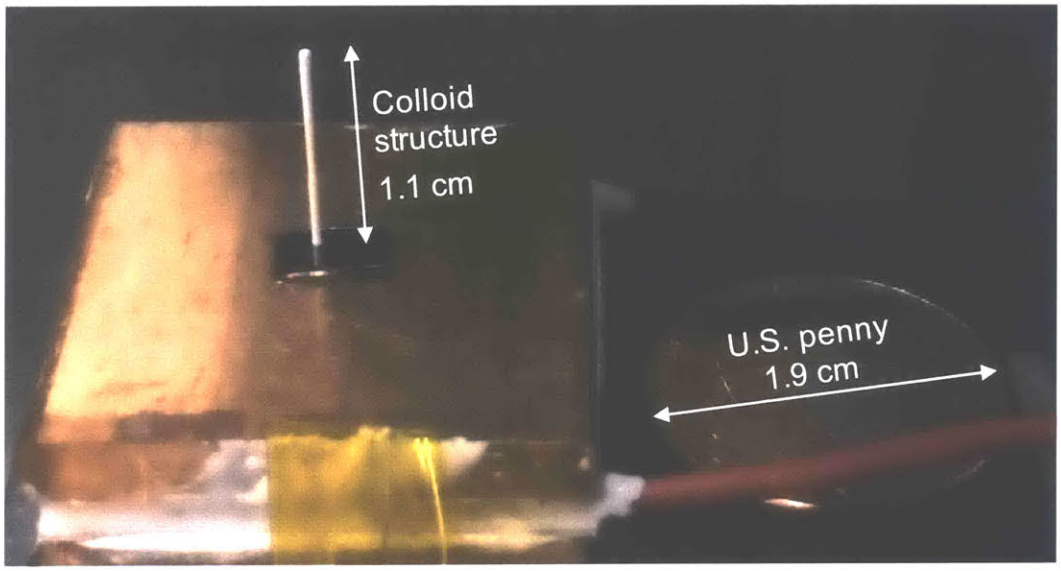

Figure S2.4. Photograph of a freestanding colloid structure 1.1 cm in height. One the right: A U.S. penny, 1.9 cm in diameter, for comparison of size. This is the tallest colloid structure that we have built with our apparatus.

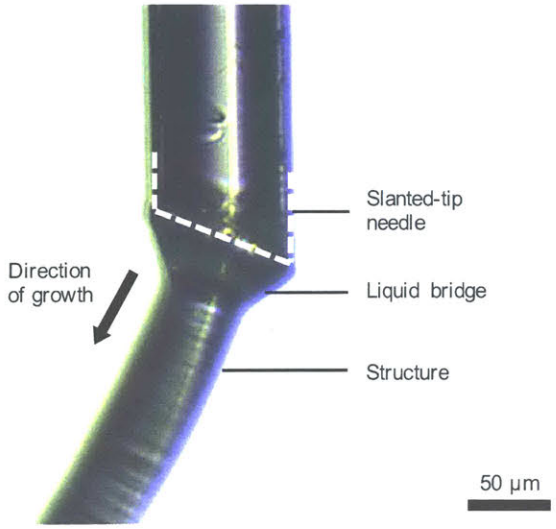

Figure S2.5. Growth of a helical structure from a slanted-tip needle.

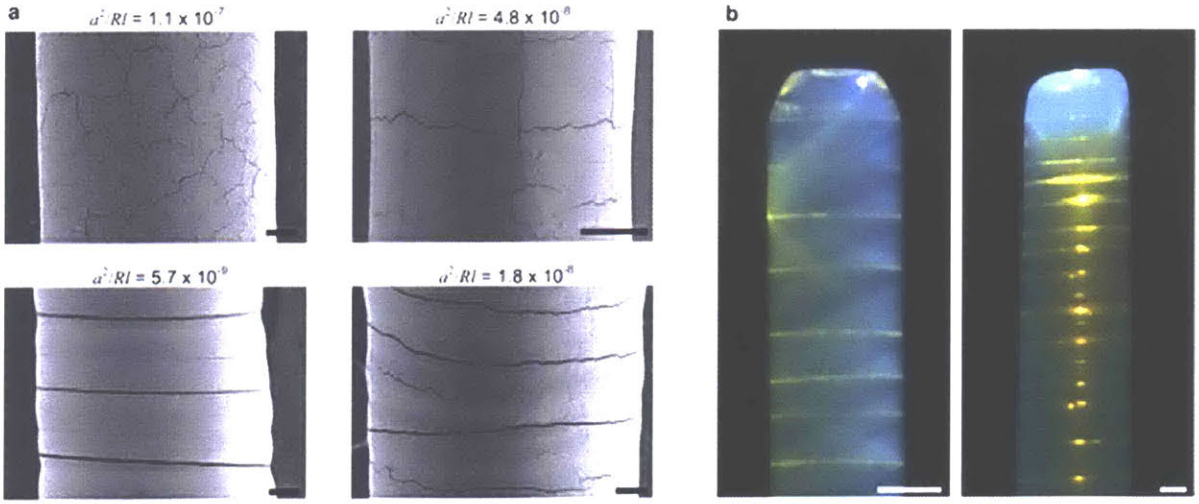

Figure S2.6 Crack patterns. (a) Clockwise from top left: crack patterns in sections of structures for $a^2/Rl = \left[1.1\times10^{-7}, 4.7\times10^{-8}, 1.7\times10^{-8}, 5.7\times10^{-9}\right]$ show a transition from cracks in arbitrary orientations to only circumferential; the bottom left image is an example of a white data point in Fig. 4b and the others are examples of grey data points. (b) Left, right: top sections of two structures (both a = 44nm) with $R = \left[110, 220\right]$ μm and $a^2/Rl = \left[1.5\times10^{-8}, 4.3\times10^{-9}\right]$ show an increase in the density of circumferential cracks in accordance with Eq. 2 and Fig. 4c. Scale bars represent 50 µm (a); 100 µm (b).

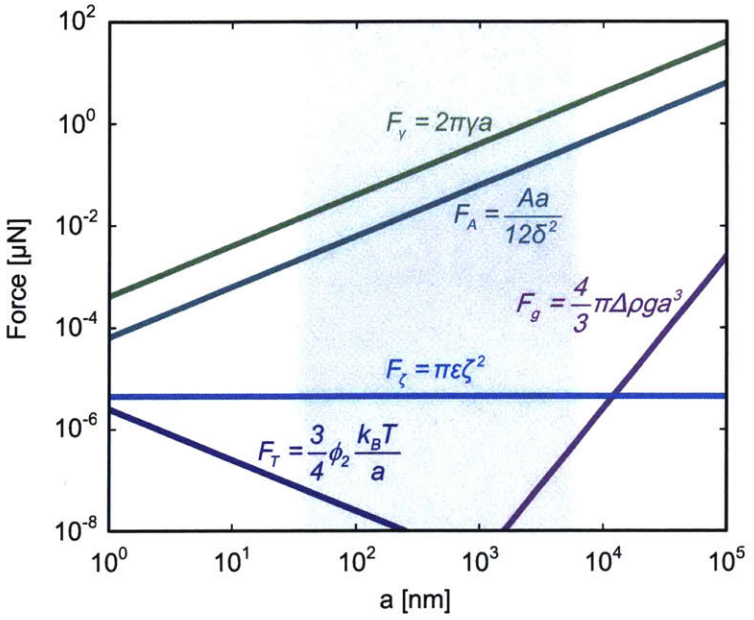

Figure S2.7. Forces acting on a particle at crack initiation. Within the section of a particle structure that develops a crack, i.e., the section with height l, we estimate the particles approximately contact one another in a close-packed arrangement (Fig. 2b, Supplementary Figures 2, 3). Estimates of the following characteristic forces on a particle are plotted above: gravitational force F_g, surface tension and capillary pressure forces F_γ, Van der Waals attractive force F_A, electrostatic repulsive force F_ζ, and thermal (i.e., osmotic pressure) force F_T. The range of particle sizes used in our experiments is indicated by the gray shaded region; in this range, surface tension and capillary pressure forces are dominant. Quantities in the above formulas are: density difference $\Delta\rho := \rho_{polystyrene} - \rho_{water} \approx 0.04\rho_{water}$; gravitational acceleration $g = 9.8$ [m/s^2]; Hamaker constant $A \approx 1.4\times10^{-20}$ [J]; molecular space between contacting particles $\delta \sim 10^{-1}$ [nm]; dielectric constant of water $\varepsilon \approx 63\varepsilon_0$ (at 70 °C); zeta potential $\zeta \approx 50$mV; temperature $T = 70$ C, and Boltzmann constant $k_B = 1.38\times10^{-23}$ [J/K]. All other quantities are defined in the main text.

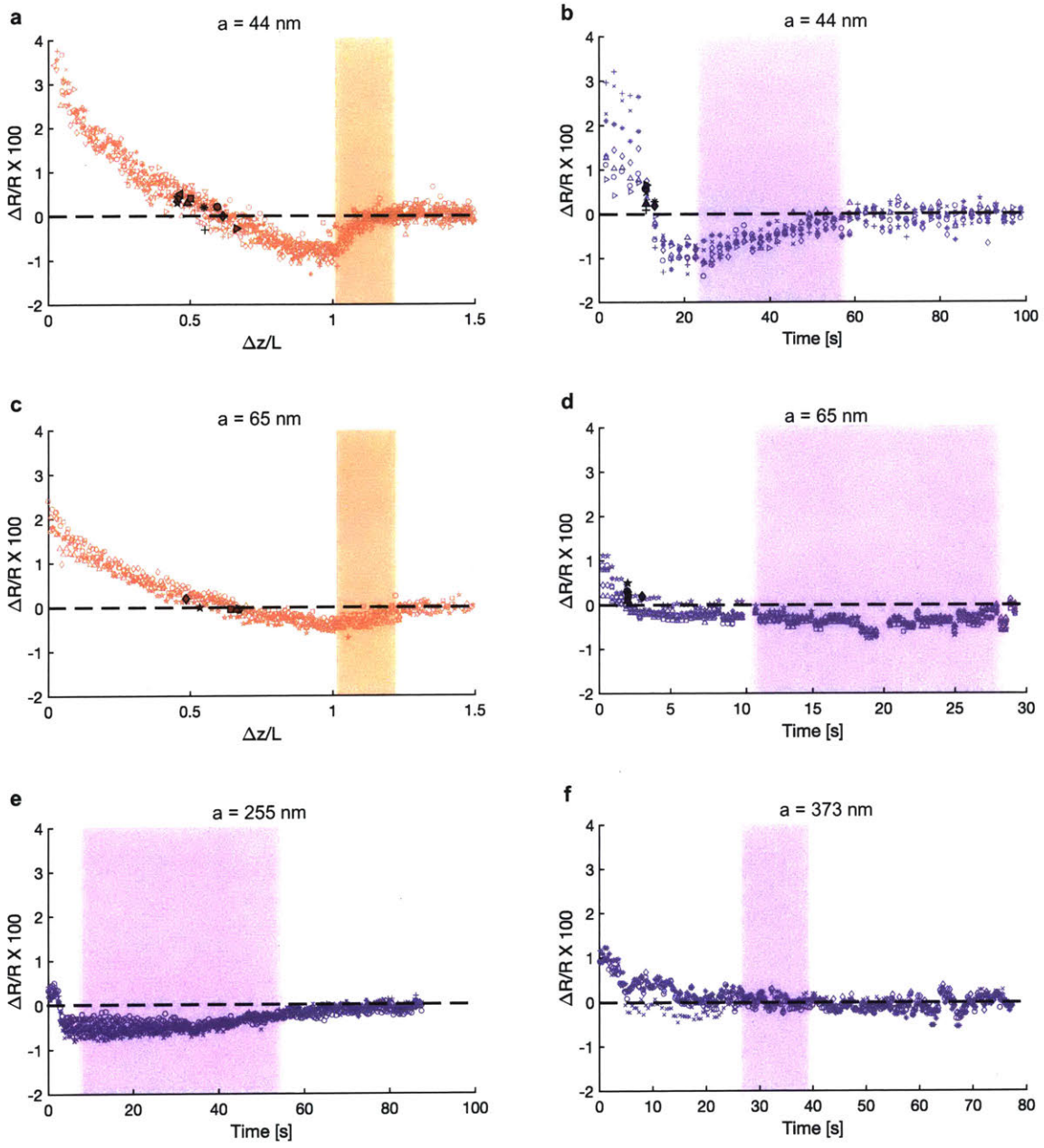

Figure S2.8. Radial changes and crack initiation. Each plot shows the radial change of a thin cross-section layer of a structure ΔR, relative to its final radius R when dry. The horizontal axis indicates whether the measurement was taken: (**i**) during construction as a function of the layer's distance below the bottom of the liquid bridge Δz, normalized by the structures wet length L; or (**ii**) at termination as a function of time. The shaded regions indicate passage through the drying front, which relieves the capillary pressure constricting the structure. Each plot shows several thin layers that were analyzed, where each individual layer is indicated by marker type; the darker-filled, black-outlined markers in (**a-d**) indicate the occurrence of a crack in the layer. The pattern of radial change is the same regardless of whether the structures crack. Plots (**a**, **b**) correspond to the same structure (also the same as Main Fig. 2b), and (**c**, **d**) correspond to the same structure.

Table S2.1. Zeta potential measurements and estimates of F_μ / F_ζ.

a [nm]	ζ [nm]	F_μ / F_ζ	γ [mN/m]	Mfr, Catalog#, Lot#
44	-44.29 ± 0.36	0.003 — 0.004	73.0 ± 2.0	Polysciences, 00876-15, Lot# 678040
65	-54.23 ± 0.92	0.0003 — 0.007	56.6 ± 1.1	Bangs, PS02N, Lot# 12799
85	-54.06 ± 1.13	0.0004 — 0.0007	56.6 ± 1.1	Bangs, PS02N, Lot# 8815
105	-51.49 ± 0.42	0.0008	56.6 ± 1.1	Bangs, PS02N, Lot# 9936
110	-44.3 ± 0.86	0.0019 —0.014	73.0 ± 2.0	Polysciences, 07305-15, Lot# 671232
140	-42.54 ± 0.28	0.002 — 0.006	56.6 ± 1.1	Bangs, PS02N, Lot# 9827
255	-36.63 ± 0.56	0.007 — 0.017	73.0 ± 2.0	Polysciences, 07307–15, Lot# 679675
373	-41.48 ± 0.15	0.01 — 0.024	73.0 ± 2.0	Polysciences, 07309-15, Lot# 671953
500	-55.34 ± 0.56	0.05 — 0.09	73.0 ± 2.0	Polysciences, 07310-15, Lot# 672955
5000	$\approx 50^*$	0.07 — 0.14	73.0 ± 2.0	Polysciences, 17136-5, Lot# 685747

*Zeta potential cannot be reliably measured due to sedimentation. Based on typical values from the other particle sizes, we assume $\zeta \approx 50\text{mV}$.

Table 2.1 | Experimental parameters for each structure built in this study.

	a [nm]	R [mm]	Z [mm]	L [mm]	$\dot{z}$ [mm/s]	Q [mm^3/s]	T [°C]	γ [N/m]	μ [Ns/m^2]	λ [nm]	ζ [V]	a^2 / Rl
1	44	0.03	0.53	0.36	0.00614	0.02422	50	73.0	5.47E-04	—	-44.29	2.1E-07
2	44	0.04	0.90	0.53	0.00371	0.01135	50	73.0	5.47E-04	—	-44.29	8.3E-08
3	44	0.10	5.43	0.98	0.00182	0.00602	70	73.0	4.05E-04	—	-44.29	1.9E-08
4	44	0.21	6.01	1.21	0.00125	0.00602	50	73.0	5.47E-04	—	-44.29	7.5E-09
5	44	0.18	5.75	1.90	0.00106	0.00285	70	73.0	4.05E-04	—	-44.29	5.7E-09
6	44	0.21	4.97	2.00	0.00077	0.00612	70	73.0	4.05E-04	—	-44.29	4.7E-09
7	65	0.21	1.95	1.00	0.00112	0.01138	70	56.7	4.05E-04	—	-54.23	2.0E-08
8	65	0.32	4.23	1.40	0.00079	0.00734	70	56.7	4.05E-04	—	-54.23	9.5E-09
9	85	0.24	3.75	1.40	0.00082	0.01178	70	52.6	4.05E-04	—	-54.06	2.2E-08
10	85	0.34	4.85	2.00	0.00076	0.00916	70	52.6	4.05E-04	—	-54.06	1.1E-08
11	95	0.23	2.49	1.40	0.00074	0.00716	70	50.9	4.05E-04	420	-50.11	2.8E-08
12	105	0.26	3.76	2.40	0.00076	0.00770	70	51.7	4.05E-04	460	-51.49	1.8E-08
13	110	0.04	0.87	0.53	0.00337	0.00538	50	69.8	5.47E-04	510	-44.3	6.0E-07
14	110	0.11	4.86	2.30	0.00138	0.01048	50	69.8	5.47E-04	510	-44.3	4.8E-08
15	110	0.19	5.98	3.25	0.00121	0.00519	70	69.8	4.05E-04	510	-44.3	1.9E-08
16	110	0.55	1.69	—	0.00044	0.02603	80	69.8	3.55E-04	510	-44.3	1.3E-08
17	140	0.29	2.12	—	0.00066	0.00894	70	54.8	5.47E-04	620	-42.54	3.2E-08
18	255	0.04	1.15	0.43	0.00289	0.00697	50	71.8	5.47E-04	—	-36.63	3.7E-06
19	255	0.12	2.21	—	0.00133	0.00308	50	71.8	5.47E-04	—	-36.63	2.6E-07
20	255	0.22	4.39	—	0.00118	0.00756	70	71.8	4.05E-04	—	-36.63	6.7E-08
21	255	0.60	3.40	—	0.00090	0.02978	80	71.8	3.55E-04	—	-36.63	3.2E-08
22	373	0.04	0.51	—	0.00250	0.00652	50	73.1	5.47E-04	—	-41.48	6.6E-06
23	373	0.12	4.12	—	0.00189	0.00497	50	73.1	5.47E-04	—	-41.48	2.8E-07
24	373	0.21	6.00	—	0.00132	0.00892	70	73.1	4.05E-04	—	-41.48	1.1E-07
25	373	0.23	4.49	—	0.00104	0.00796	70	73.1	4.05E-04	—	-41.48	1.4E-07
26	500	0.04	0.37	—	0.00255	0.00519	50	70.9	5.47E-04	—	-55.34	1.7E-05
27	500	0.23	5.34	—	0.00144	0.00787	50	70.9	5.47E-04	—	-55.34	2.0E-07
28	5000	0.12	2.25	—	—	—	70	—	4.05E-04	—	—	9.7E-05
29	5000	0.03	3.20	—	—	—	70	—	4.05E-04	—	—	3.1E-04
30	5000	0.09	0.77	—	—	—	70	—	4.05E-04	—	—	3.6E-04
31	5000	0.14	1.33	—	—	—	70	—	4.05E-04	—	—	1.4E-04

Columns left to right: particle size, structure radius, structure total height, wet length to drying front (if applicable), build rate, rate of total evaporation, temperature, estimate of surface tension in the wet section, water's viscosity, peak wavelength reflection (if applicable), zeta potential (if applicable), a^2/Rl (plotted in Fig. 4b).

3 In-plane direct-write assembly

The work presented in this section was a joint effort with fellow graduate student Sara Nagelberg, and undergraduate students Elizabeth Chang-Davidson and Joel Tan. The design and construction of the experiment apparatus was implemented jointly between Elizabeth and myself. Elizabeth and Joel performed most of the direct-write experiments. I performed microstructural characterization and modelling of assembly rate. Optical characterization was jointly performed by Sara and myself. The implementation of optical modelling (outlined in Supporting Information) is credited to Sara. The work here was originally written for the following journal article:

> Tan, A. T. L.; Nagelberg, S. N.; Chang-Davidson, E. C.; Tan, J.; Yang, J. K.; Kolle, M.; Hart, A. J. Digital fabrication of Patterned Colloidal Crystals by Direct-Write Assembly. *In preparation.*

3.1 In-plane direct-write assembly of patterned colloidal crystals

Nature is replete with instances of hierarchically structured materials that create visually stunning appearances. For example, peacock feathers, butterfly wings, and beetle shells are structured on the nano-, meso-, and macro-scales, resulting in iridescence and structural color.[73–75] There is also much scientific interest and commercial value in creating similarly structured man-made materials for applications including photonic devices and visual displays.

These and other technology needs require materials fabrication techniques that provide control of material structure over multiple length scales. Self-assembly provides a convenient means for controlling material structure from the bottom up, and there have been numerous works on convective self-assembly of colloidal particles into photonic crystals, including seminal work by Vlasov[22] and others.[76–79] It is even possible to create patterned colloidal crystals for photonic and sensing applications.[80–82] However, these techniques often require the

prefabrication of templates or masks, and lithographic etching,[77,83] especially when spatial control of the material is required.

Recently, we presented a means for combining the principles of colloidal self-assembly with direct-write techniques. By controlling the motion of a dispensing syringe needle relative to a stage, it is possible to fabricate colloidal crystals into specific shapes, such as vertical pillars and more complex geometries such as helices.[84] Here, we extend this technique to the more general case of planar direct-write self-assembly. We show direct-write self-assembly as a tool for fabrication of high quality iridescent colloidal crystals in arbitrary patterns, wherein in the pattern is predetermined by a digital template.

Direct-write assembly is performed by the scheme shown in Fig. 3.1a. A silicon wafer or glass substrate is mounted onto a stage with precision motion control and temperature control (30 °C). A dispensing needle is positioned slightly above the substrate. A suspension of polystyrene particles (diameter D = 746 nm) is dispensed through the needle and contacts the substrate, forming a liquid meniscus between the needle and the substrate. The substrate is then moved laterally by the stage, while maintaining the gap between the substrate and the needle. As the substrate moves, particles are transported to the trailing edge of the meniscus by an evaporation-induced flux. The particles are then compacted into a colloidal crystal at the trailing edge of the meniscus. Therefore, a crystal can be written by relative motion of the needle over the stage at a velocity matching the approximate rate of crystal growth. An optical image of an exemplary colloidal crystal is shown in Fig. 3.1c. Furthermore, the trajectory of crystal growth can be influenced by multi-axial stage motion. As an example, Fig. 3.1b shows alternating stage

movement in the x and y directions, resulting in a serpentine-shaped crystal which appears iridescent to the naked eye.

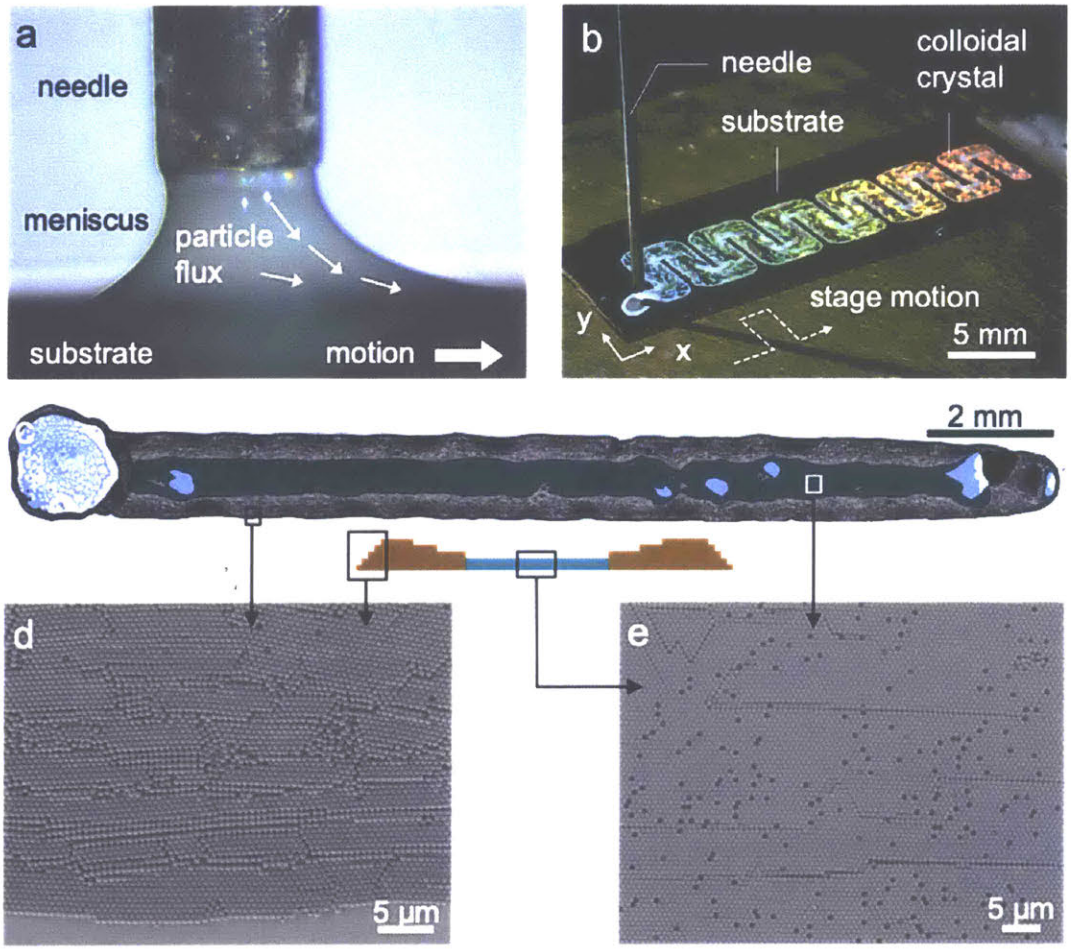

Figure 3.1. Fabrication of colloidal crystals by in-plane direct-write self-assembly. (a) In-plane direct-write self-assembly is performed by precision dispense of a colloidal suspension from a needle, coupled with lateral substrate motion. (b) A colloidal crystal can be patterned by movement of the stage in planar *x* and *y* directions. (c) Optical image (top) and schematic cross-section (bottom) of an exemplary colloidal crystal. The edge of the crystal (brown coloration) is thicker than the middle. The middle consists of mostly particle bilayers (green coloration) and monolayers (blue coloration). (d) SEM image showing multilayer terraces at the edge of the crystal. (e) SEM image of the middle region of the crystal showing defects such as dislocations and vacancies.

3.2 Kinetics of in-plane assembly

For the purpose of studying the rate of crystal growth, the stage is moved in a single direction at a constant speed. We consider the speed of the stage to be equivalent to the write speed. To grow the crystal shown in Fig. 3.1c, the substrate was translated from left to right. Therefore, the direction of crystal growth was from right to left. When the stage motion and the dispense of particles was stopped, the meniscus pinched off, leaving behind a "coffee-ring stain" typical for aqueous colloidal suspensions. In Fig. 3.1c, the structural colors correspond to different crystal thickness. Blue regions correspond to particle monolayers, green regions correspond to bilayers, and the other brownish colors correspond to 3 or more layers of particles. We observe that the edge of the crystal is thicker than in the middle, a result of outward capillary flow towards the contact line of the meniscus. However, the thickness of the middle region is uniform and can be controlled by the write speed, as will be discussed in detail later. SEM confirms the presence of multiple layers of particles at the edge (Fig. 3.1d), and a uniform crystal thickness in the middle region. In the middle region, the particles are dominantly in hexagonal packed order, albeit with typical crystal defects such as vacancies and dislocations.

The key to continuous direct-write self-assembly of colloidal crystals is matching the write speed to the rate of crystal growth determined by evaporative flux from the trailing meniscus. We can approximate the rate of crystal growth at the trailing end of the meniscus to be the same as in other convective assembly techniques such as dip-coating and blade-casting.

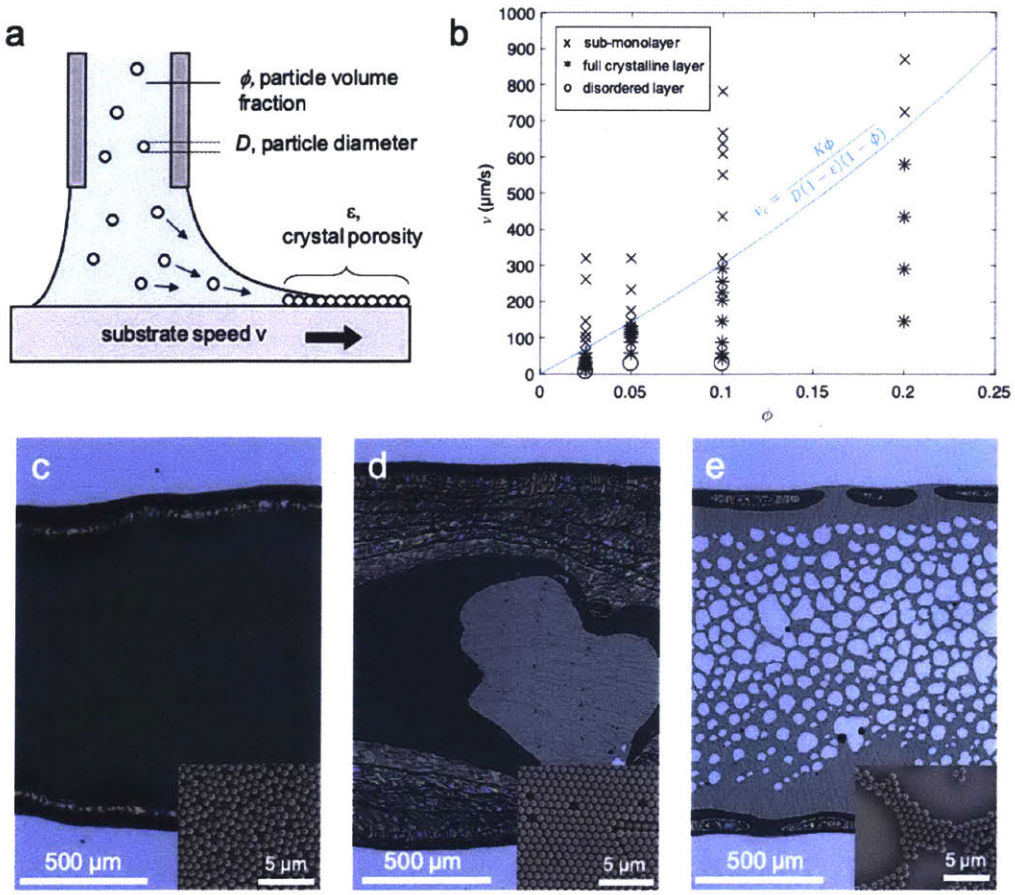

Figure 3.2. Optimization of direct-write process parameters. (a) Schematic of the direct-write assembly process, where ϕ is the volume fraction of particles in solution, D is the particle diameter, ε is the porosity of the colloidal crystal, and v is the substrate speed. (b) An operational phase diagram where disordered, crystalline, and sub-monolayer phases are plotted as a function of ϕ and v. The curve delineates the natural assembly speed as modelled by the Dimitrov-Nagayama equation. (c-e) Optical microscope images and inset SEM of colloid trails with (c) disordered, (d) ordered, and (e) sub-monolayer phases.

By considering the balance of the rate of crystal growth with the flux of water and particles transported to the crystal growth front, Dimitrov and Nagayama[85] proposed the following equation to calculate the rate of crystal growth v_c,

$$v_c = \frac{\beta l j_e \varphi}{h(1-\varepsilon)(1-\varphi)} \qquad \textbf{Eq 3.1}$$

Here, h is the height of the crystal, ε is the porosity of the crystal, and φ is the volume fraction of particles in suspension, as depicted in Fig. 3.2a. Further, l is a characteristic evaporation length, j_e is the water evaporation flux, and β is an interaction parameter between 0 and 1, where $\beta = 1$ corresponds to complete entrainment of particles by water flux.

The thinnest possible crystal is a particle monolayer, where $h = D$. Moreover, it is possible to simplify the equation by lumping $\beta l j_e$ into an experimentally fitted parameter K, as previously demonstrated by Prevo and Velev.[86] Eq 3.1 therefore simplifies to

$$v_c = \frac{K\varphi}{D(1-\varepsilon)(1-\varphi)} \qquad \textbf{Eq 3.2}$$

This simplified equation can then be used to create an operational phase diagram which maps the relationship between experimental variables and crystallinity of the deposited particles. From a series of experiments at different write speeds v and feedstock particle concentrations φ, we identified disordered, ordered, and sub-monolayer phases, as plotted in Figure 3.2b. The curve delineates the rate of crystal growth for a monolayer according to Eq 3.2, with ε = 0.605 (corresponding to hexagonal close packing) and fitting $K = 8 \times 10^4$ m^2/s. Below this line, crystalline phases of at least single-particle thickness are obtained, such as shown in Fig. 3.2d. Above the line, the write speed v exceeds the rate of crystal growth v_c, resulting in a sub-monolayer phase, such as shown Fig. 3.2e. Additionally, we note that, at very low speeds, the particles are deposited as disordered aggregates, such as shown in Fig. 3.2c.

This operational phase diagram serves as a practical guide for high throughput direct-write self-assembly. As a case in point, the typical as-received concentration of commercial colloidal particles is $\varphi = 0.025$, which requires a write speed of ~50 μm/s for the crystalline phase. However, by simply increasing the concentration of particles to $\varphi = 0.2$ via centrifugation and decanting, the concentrated particle suspension can then be used to boost write speed by an order of magnitude to ~600 μm/s.

3.3 Effect of toolpath

Multi-axial stage motion moves the substrate relative to the dispensing needle, essentially creating a toolpath for the direction of crystal growth. Therefore, a colloidal crystal can be directly patterned using a digital template, without the need for further process steps such as etching. To create a digital template, we created a simple vector graphic (SI Fig. S3.1) which was then converted to a script of commands for moving the stage in x and y directions. The colloid suspension is dispensed at a constant rate while translating the stage according to the script, resulting in a patterned colloidal crystal in the shape of the vector graphic, as shown in Fig. 3.3.

The general iridescence throughout the colloidal crystal indicates a high degree of crystallinity. However, we note some small regions lacking iridescence, which indicates lack of particle order. Specifically, these regions occur where there was a turn or overlap in the toolpath, suggesting that the toolpath trajectory can have a strong influence on self-assembly.

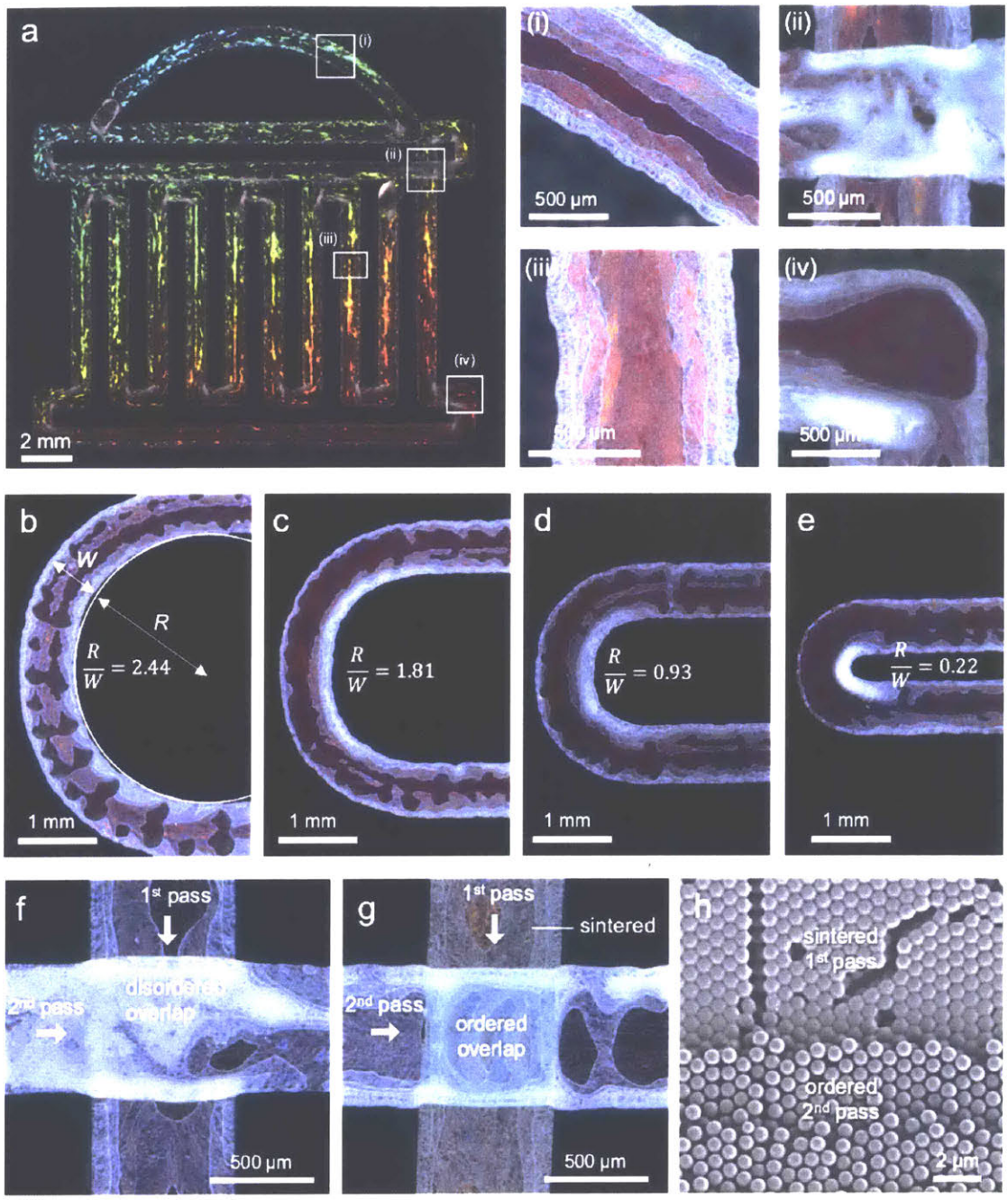

Figure 3.3. Effect of direct-write tool path on crystal order. (a) Left: Photograph of a colloidal crystal patterned by control of the direct-write trajectory. Right: Optical microscope enlargements showing the morphology of a (i) wide arc, (ii) overlap, (iii) straight line, and (iv) sharp turn. (b-e) The crystallinity of a colloidal trail is affected by curvature of the direct-write trajectory, as demonstrated by curved trails with turning radius of (b) 2.0 mm, (c) 1.5 mm, (d) 1.0 mm, and (e) 0.5 mm. W is the width of the trail and R is the inside radius of curvature of the

trail. Generally, the inside of the curved trail is ordered when R/W > 1 but becomes disordered when $R/W < 1$. (f-g) Optical images of perpendicular overlapping trails. (f) Without sintering, overlapping colloidal trails result in disorder, as apparent from the whitish region on the trail from the second pass. (g) After sintering of the trail from the first pass, the trail from the second pass is deposited atop with crystalline arrangement. (h) SEM image of a sintered first pass and an ordered second pass.

The local curvature of the toolpath affects order, and the limiting cases are revealed in Fig. 3.3a i, iii and iv. In the limit of a straight line (Fig. 3.3a iii) or wide arc (Fig. 3.3a i), crystallinity is maintained. In contrast, in the limit of a sharp 90 ° turn, there is a whitish patch on the inside of the turn which indicates a region of disorder. Therefore, there must be some intermediate radius of curvature that corresponds to the onset of particle disorder.

To investigate this onset, we performed a series of experiments with different tool path curvatures. We denote the inside radius of curvature as R and the width of the colloidal trail as W, as shown in Fig. 3.4a. Fig. 3.4a-d shows colloidal trails with progressively smaller R. However, W is constant because it is dictated by the diameter of the dispensing needle, which is kept the same. In general, as R decrease relative to W, the deposit of particles on the inside of the turn becomes thicker and eventually becomes disordered when R << W. This observation is in general agreement with the operational phase diagram (Fig. 3.2b) which shows that slow write speeds lead to disordered deposits. The deposition rate of particles relative to the local tangential velocity is inversely proportional to the local curvature of the path. In the experimental conditions for Fig. 3.4e, the volume fraction of particles $\varphi = 0.05$ and the tangential velocity at the middle of the tool path is $v_1 = 146$ μm/s. The radius of curvature at the middle of the toolpath is $R_1 = 500$ μm and the inside radius of curvature of the toolpath is $R_2 = 140$ μm. Therefore, the

tangential velocity at the inside of the toolpath is $v_2 = (R_2/R_1)v_1 = 40$ μm/s. These conditions ($\varphi = 0.05$, $v_2 = 40$ μm/s) corresponds to the onset of disorder in Fig. 3.2b.

Fig. 3.3 (ii) shows that an overlap in the direct-write toolpath results in disorder, and we hypothesize that this is due to the array of particles from the first pass being broken up by the liquid meniscus during the second pass. Therefore, if the particles from the first pass are effectively immobilized, then it may be possible to prevent the break-up of the particle array and preserve crystallinity for multiple passes to build up 3-D prints.

One means of immobilizing the particle array is to sinter the particles. To sinter the particles, a colloidal crystals sample was heated to 110 °C for 15 minutes, followed by 1 minute of oxygen plasma treatment. The oxygen plasma improves the wettability of the surface, which becomes hydrophobic after the heating step. The sintering causes a slight color change in the colloidal crystal due to necks forming between the particles, which reduces the interparticle spacing. A second pass of direct-write was then performed atop the first pass, as shown in Fig. 3.3g. Separately, a second pass of direct-write was also performed on a control sample which was not sintered, as shown in Fig. 3.3f. The preservation of structural color on the sintered sample, compared to the whitish regions on the control sample, shows that sintering was effective in immobilizing the particle array from the first pass, allowing the particles on the second pass to self-assemble on the sintered array with crystalline registry. SEM confirms particle order on the second pass for the sintered sample (Fig. 3.3h), and particle disorder the second pass for the control sample (SI Fig. S3.2). Potentially, layer-wise sintering of the particles

could be employed for building up multilayer structures with crystalline registry of the particles, which would be a means of 3-D printing colloidal crystals.

3.4 Optical properties

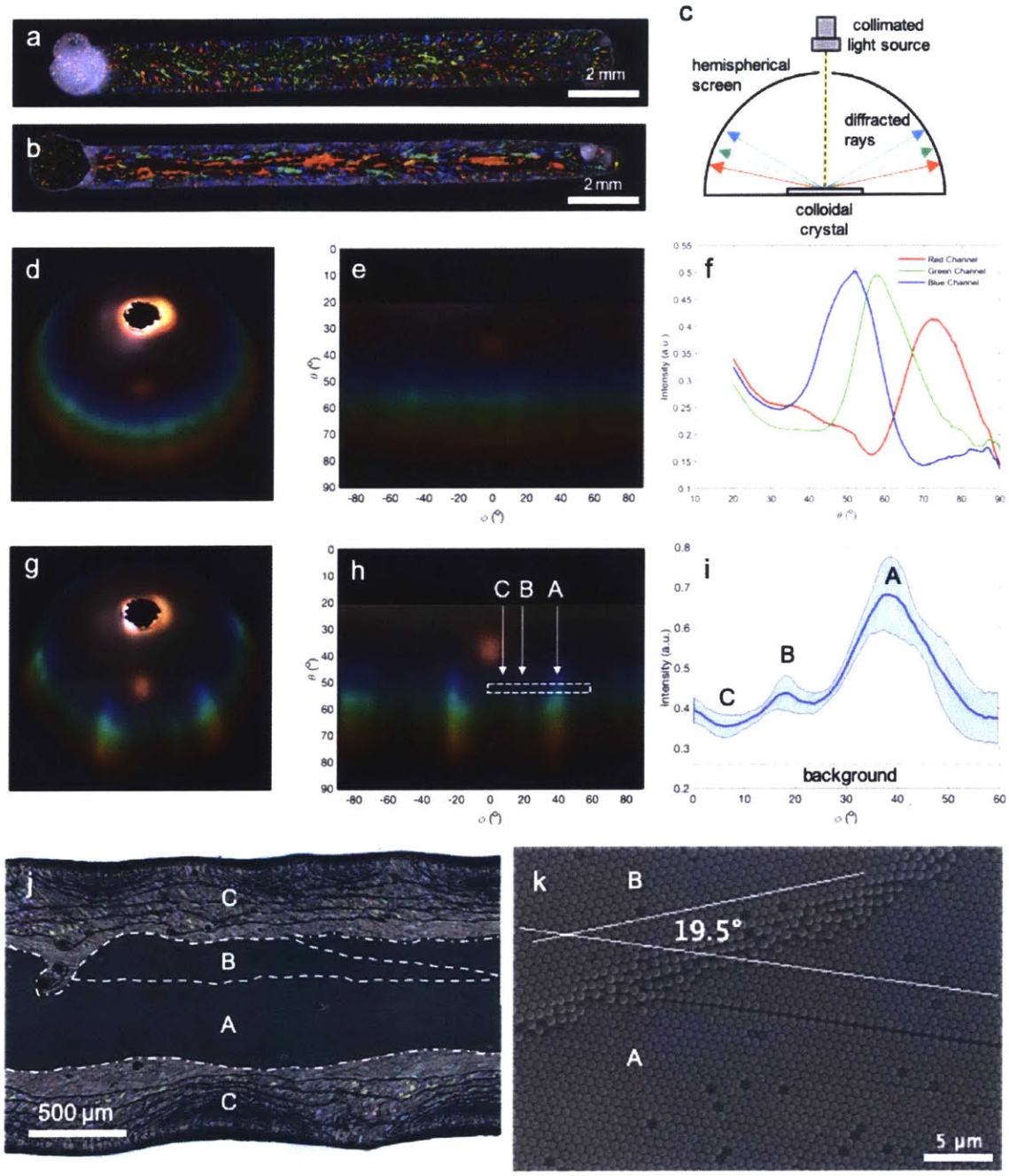

Figure 3.4. Optical properties of direct-write colloidal crystals. (a,b) Photographs of (a) small-grain and (b) large-grain colloidal crystal imaged under ring lighting around the objective lens. (c) Schematic depicting the characterization of optical properties by illuminating the colloidal crystal with collimated light at an angle normal to the crystal and observing the projection of diffracted colors on a hemispherical screen. (d,g) Photograph of colors projected from the (d) small-grain and (g) large-grain colloidal crystal. (e, h) Colors from the (e) small-grain and (h) large-grain samples linearly mapped onto azimuthal angle ϕ and polar angle θ. (f) Plot of intensity vs θ for each of the RGB channels, obtained by averaging over all values of ϕ. (i) Plot of intensity vs ϕ derived from the blue channel of (h), ranging $\phi = 0$ to 60°, at $\theta = 52°$. The solid blue line is the intensity averaged over 6-fold symmetry. The shaded region represents uncertainty. The highest peak is from the largest grain, A; the second highest peak is from the second-largest grain, B; The lowest intensity is an estimate of the amount of light from various other small grains, C. The shaded region represents measurement uncertainty. (j) Optical image of the illuminated region, with A, B, and C grain structures identified. (k) SEM image analysis confirms that the largest grain A and the second-largest grain B are misoriented by 19.5°.

The direct-write colloidal crystals exhibit an intriguing array of structural colors that seem correlated to crystalline order, lighting, and viewing conditions. Indeed, colloidal assemblies are known to exhibit a diverse range of optical phenomena which can form the basis for functional devices such as lasers, displays, and sensors. The primary mechanisms by which structural colors are commonly created are broadly categorized into thin film interference, multilayer interference, grating diffraction, and interference phenomena, each enabled by nano- to micro- scale periodicity on the order of the wavelengths of visible light.[87] We therefore characterize the optical properties of these direct-write colloidal crystals to elucidate the mechanism for their iridescent structural color. Moreover, we compare small-grain (grain size < 0.01 mm^2) samples, (Fig. 3.4a) prepared by fast write speeds, and large-grain (grain size > 0.1 mm^2) (Fig. 3.4b) samples, prepared by optimized write speeds, so as to establish structure-property relationships via optical characterization.

To characterize the light scattering and iridescence of a printed colloidal crystal, we illuminated the sample with collimated light such that the reflected light was projected onto a translucent hemispherical screen, as illustrated in Fig. 3.4c. This technique allows colors from all viewing angles to be visualized in a single image.[88] The projection of colors from the small-grain sample (Fig. 3.4a) is shown in Fig. 3.4d. The separation of color leads us to hypothesize that the colloidal crystal acts as a reflective diffraction grating, since shorter wavelengths are diffracted at smaller angles with respect to the normal, as one would expect from the grating equation

$$m\lambda = d(\sin\theta_i + \sin\theta_m) \qquad \textbf{Eq 3.3}$$

Where m is the diffraction order, d is the grating spacing, θ_i and θ_r are respectively the angles of incident and diffracted rays relative to the normal. In our experimental conditions, m = 1 since we observe only one diffraction order, $\theta_i = 0°$ since the incident ray is normal to the sample, and $d = \sqrt{3}/2D$ since the particles are arranged in a hexagonal lattice.

The colors on the hemispherical screen in Fig. 3.4d can be linearly mapped with respect to polar angle θ and azimuthal angle ϕ, yielding Fig. 3.4e. From Fig. 3.4e, the intensity can be averaged over all values of ϕ and plotted as a function of θ for each of the three color channels, as shown in Fig. 3.4f. The peaks can be used, in conjunction with Eq. 3.3, to estimate particle size by using λ = 490, 550, and 650 nm as the peak wavelengths for the blue, green, and red channels respectively.[89] This yielded an estimated diameter of 751 nm, which is close to the known colloid diameter of 746 nm.

If there are many small grains present, such as for the sample shown in Fig. 3.4a, then there will be many overlapping diffraction peaks, such that the scattered intensity is almost constant along all ϕ angles. However, if there are only a few grains present, then there will be distinct peaks visible. When the same experiment is performed with the large-grain sample (Fig. 3.4b), strong diffraction peaks are observed, as shown in Fig. 3.4g and 3.4h. The six-fold symmetry of the diffraction pattern projected onto the sphere indicates that the particles are in hexagonal arrangement. Moreover, by analyzing the relative intensities of the peaks, it is possible to deduce information about the size proportions of the grains present in the illuminated sample area. To perform this analysis, we extracted intensity vs ϕ from the $\theta = 52°$ segment of Fig. 3.4h and plotted the data as Fig. 3.4i. Due to the six-fold symmetry of the diffraction pattern, the data is collapsed onto $\phi = 0$ to $\phi = 60°$. The highest and second-highest peaks should correspond to the largest and second-largest grains, which we designate as grains A and B, respectively. The intensity level marked by the black solid line should then correspond to the much smaller grains of various orientations, which we designate as C. By comparing the relative peak intensities, we estimate that the area fraction of the various grain structures are $f_A \approx 0.4$, $f_B \approx 0.1$, and $f_C \approx 0.5$ (see SI for description of calculation). This result may be compared to the direct measurement of relative grain sizes via image analysis. An optical micrograph of the illuminated region is shown in Fig. 3.4j, with the A, B, and C structures identified and labelled. By image segmentation, we measured $f_A = 0.32$, $f_B = 0.09$, and $f_C = 0.59$. Given the large uncertainty in the peak signal for A, the estimates from the diffraction peak intensities are in reasonable agreement with the measurements from the micrograph. Finally, using SEM (Fig. 3.4k), we measured that

grains A and B are misoriented by 19.5°. This is in close agreement with the intensity plot (Fig. 3.4i), which shows the A and B peaks 20° apart.

3.5 Conclusions

We demonstrated freeform fabrication of colloidal crystals by in-plane direct-write self-assembly, and experimentally derived an operational phase diagram which maps write-speeds and particle concentrations that lead to crystalline features. We demonstrated the effect of toolpath trajectory on the crystallinity of the colloidal assemblies, and showed that sintering can be used to stack overlapping passes. Finally, we established grating diffraction as the mechanism for the structural color effects in these colloidal crystals, and showed that simple characterization of the optical properties of the crystals yields reliable information about microstructure, such as particle order, grain size, and orientation. In future work, in-plane direct-write assembly could be extended to a practical technique for 3-D printing of colloidal crystals if a means for rapidly sintering each layer could be developed. Additionally, a propitious line of research would be to explore how the direct-write technique could be employed to assemble diverse types of particles to create complex colloidal assemblies for applications. As a simple example, in Fig. 3.5, we demonstrate direct-write of colloidal crystals comprising of different particle sizes (500 nm, 746 nm, and 1 μm) and different particle compositions (PS, PMMA, and silica) on the same silicon wafer. Fig. 5 also demonstrates the limits to the width of the crystal that can controlled by the diameter of the needle. Although smaller needles may be used for direct-write assembly, the width of the crystal is not strictly proportional to the diameter of the needle, as shown from the progression of needle sizes from 22 gauge (OD/ID = 0.7 mm / 0.4 mm) to 27 gauge (OD/ID =

0.4 mm / 0.2 mm) to 33 gauge (OD/ID = 0.2 mm / 0.1 mm). At 33 gauge, the smallest needle size, the crystal width was similar to that of the 27 gauge due to similar spreading of the liquid meniscus (SI Fig. S3.3). Spreading of the liquid meniscus at a finite contact angle is necessary for successful deposition of particles.[90,91] Future work on direct-write could include exploring the ultimate resolution limits of direct-write by tuning the hydrophilicity of the surface via plasma treatment or pre-depositing molecular self-assembled monolayers onto the substrate so as to control spreading of the meniscus. Finally, we note that, while macroscopic printed features can be well-controlled by the direct-write toolpath, at the microstructural level, every trace or image that is printed with direct-write is unique, which suggests applications of direct-write in generating security codes.

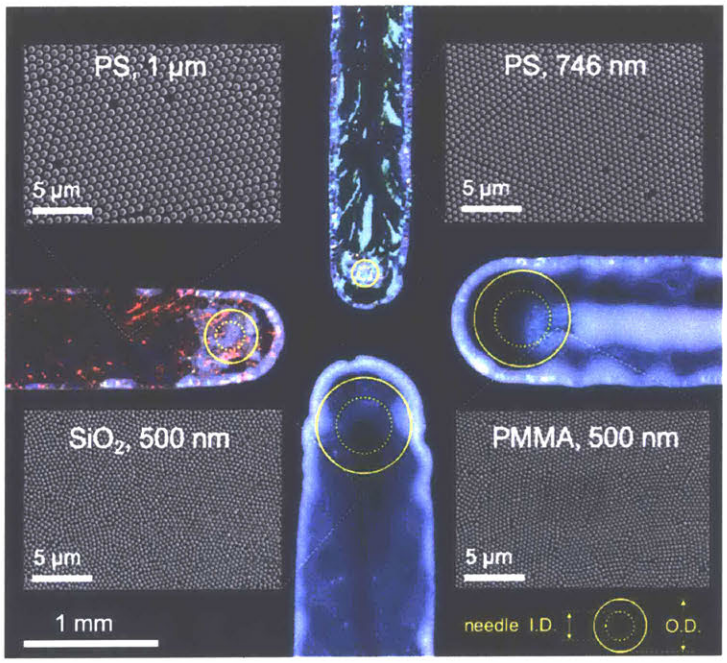

Figure 3.5. Multiple colloidal crystals fabricated on a single substrate with different needle sizes. Clockwise from top: 746 nm polystyrene particles with a 33 Ga needle; 500 nm polymethylmethacrylate (PMMA) particles with a 22 Ga needle; 500 nm silica particles with a

22 Ga needle; 746 nm polystyrene particles with a 27 Ga needle. The needle diameters are overlaid on the respective colloidal crystal.

3.6 Experimental details

Direct-write self-assembly. An aqueous suspension of polystyrene particles (750 nm diameter, Polysciences Inc.) was loaded into a 100 µl syringe (Hamilton 1710 RN) affixed with a blunt tip needle (Hamilton point style 3, 27Ga) and placed into a custom-made holder. The plunger of the syringe is depressed using a linear actuator (M-229.26S, Physik Instrumente) commanded from a computer. The stage is heated to 30±0.1 °C by a thermoelectric chip (Custom Thermoelectric) and the stage temperature is measured by an embedded K-type thermocouple (Omega) fed to a temperature controller (PTC 10, Stanford Research Systems). The stage is actuated by linear motors (Zaber LRM025A- E03T3-MC03) controlled by a two-axis stepper motor controller (Zaber X-MCB2- KX14B) via the Zaber Console software. To perform direct-write in complex trajectories, the shapes were drawn using Carbide Create software, and the G-code was converted into native motor commands using the G-code translator in the Zaber Console software.

Microstructural characterization. Optical images were taken using a Zeiss Smartzoom optical microscope. Images were taken in coaxial lighting mode (Fig. 1c, 2c, 2d, 2e, 5j) to clearly distinguish monolayers, bilayers, and multilayers. Images were taken in ring lighting mode (Fig. 3, 4, 5a, 5b) to clearly distinguish iridescent and non-iridescent regions. SEM was performed with a Zeiss Merlin High Resolution SEM in high efficiency secondary electron imaging mode,

at an accelerating voltage of 1 kV and probe current of 100 pA. Image analysis was performed using ImageJ.

Characterization of optical properties. The colloidal crystal sample was illuminated by a light source (Ocean Optics HL-2000) directed by an optical fiber (Thorlabs M25L01, ø200μm, 0.22 NA) to a collimating lens (Thorlabs F230SMA-A, alignment wavelength = 543 nm, f = 4.34 mm, NA = 0.57). The collimated light was directed to shine through a hole drilled through a translucent hemispherical screen (half a ping pong ball) and onto the sample placed in the middle of the enclosing hemisphere. The light projected onto the screen was recorded with a DSLR camera (Canon EOS Rebel T3i) which was fixed in position using an articulated arm.

3.7 Supporting Information

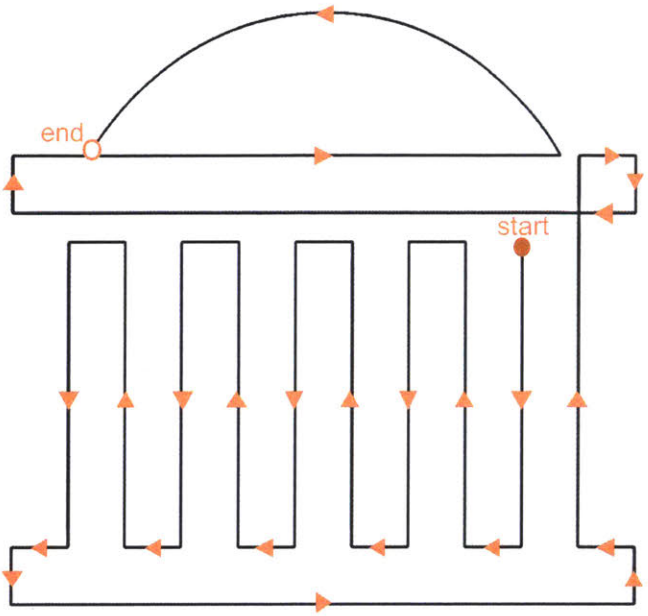

Figure S3.1. Simple vector graphic (black line) overlaid with the direct-write toolpath (orange arrows) used for fabrication of the colloidal crystal shown in Fig. 3a.

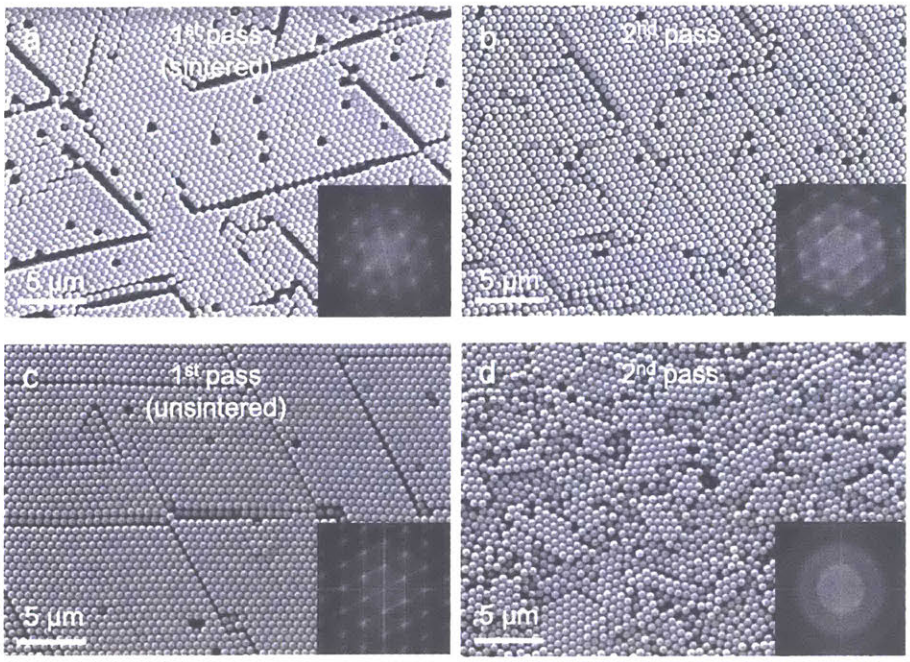

Figure S3.2. SEM of overlapping passes. (a) Sintered 1st pass. (b) 2nd pass over the sintered 1st pass. (c) Unsintered 1st pass. (c) 2nd pass over the unsintered 1st pass. Insets: 2-D Fast Fourier Transform of the corresponding image. Hexagonal peaks indicate order and the diffuse rings indicate disorder.

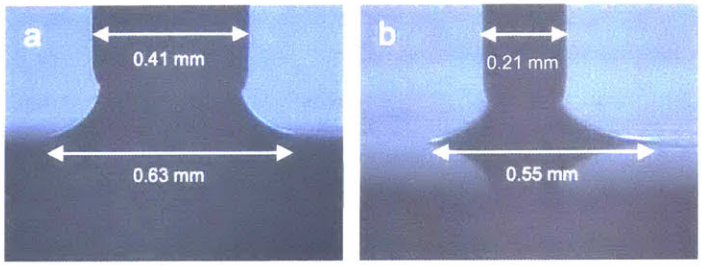

Figure S3.3. Optical images of the meniscus spreading from a (a) 27 gauge needle and (b) 33 gauge needle. Although the 33 gauge needle is half the diameter of the 27 gauge needle, the spreading of the liquid meniscus is not proportional to the diameter of the needle.

Quantitative Angle Measurements from Ping Pong Ball images.

Courtesy of Sara Nagelberg

The ping pong ball as a screen is a clean and simple way of capturing the full color distribution for all viewing angles in just a couple measurements. From a top view of the ping pong ball it is simple to quantitatively map pixels on the image to precise angles (θ, ϕ). From the center of the ping pong ball (found by manually fitting a circle to the edges in imagej)

$$(x, y) = (R\cos(\phi)\sin(\theta), R\sin(\phi)\sin(\theta))$$

Unfortunately the top view of the ping pong does not always easily captured, particularly when the illumination is at normal incidence. For this reason, we captured the color pattern from a side view of the ping pong ball. We define the viewing direction of the camera as $(\theta_{cam}, \phi_{cam} = 0)$ and mapping back from these views can be done with a coordinate transformation. First we will define a new pair of angles (Δ, β) measured from the camera to sample axis as shown in Figure S4. Again measured from the center of the ping pong ball the pixel locations corresponding to these angles are:

$$(x, y) = (R\cos(\beta)\sin(\Delta), R\sin(\beta)\sin(\Delta))$$

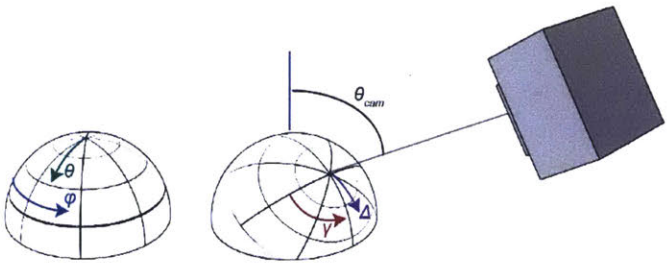

Figure S3.4. Camera Angle. Global coordinate system shown as well as the projected system, when imaged at an angle. Δ is the angle measured from the camera axis, and γ is the azimuthal angle in this rotated coordinate system. By converting from (Δ, γ) coordinates to the global (θ, ϕ) coordinates, we can quantitatively determine the angle to which each color is scattered from photographs taken at an angle.

In order to determine (Δ, β) in terms of (θ, ϕ), consider a point on the surface of the ping pong ball in 3D:

$$\begin{pmatrix} X \\ Y \\ Z \end{pmatrix} = \begin{pmatrix} \cos(\phi)\sin(\theta) \\ \sin(\phi)\sin(\theta) \\ \cos(\theta) \end{pmatrix}$$

We then can rotate these coordinates first around the Z-axis by ϕ_{cam} then around the y axis by θ_{cam} to get new coordinates:

$$\begin{pmatrix} X' \\ Y' \\ Z' \end{pmatrix} = \begin{pmatrix} \cos(\theta_{\text{cam}}) & 0 & \sin(\theta_{\text{cam}}) \\ 0 & 1 & 0 \\ -\sin(\theta_{\text{cam}}) & 0 & \cos(\theta_{\text{cam}}) \end{pmatrix} \begin{pmatrix} \cos(\phi_{\text{cam}}) & -\sin(\phi_{\text{cam}}) & 0 \\ \sin(\phi_{\text{cam}}) & \cos(\phi_{\text{cam}}) & 0 \\ 0 & 0 & 1 \end{pmatrix} \begin{pmatrix} X \\ Y \\ Z \end{pmatrix}$$

And then:

$$\beta = \operatorname{atan}\left(\frac{Y'}{X'}\right), \qquad \Delta = \operatorname{acos} Z'$$

Grain and Colloid Size Estimates

From the color distributions, it is possible to gain an estimate of the grain and colloid size in the illuminated area. Each grain will diffract light in a pattern with six-fold symmetry, the angle that each color is scattered to is set by the first order diffraction equation:

$$\sin(\theta) = \frac{\lambda}{d}$$

Where $d = \frac{\sqrt{3}}{2}D$ is the distance between diffraction planes and D is the diameter of the colloids. Main Figure 4f shows the intensity as a function of polar angle θ for each of the three color channels, obtained by averaging over all values of ϕ. The peaks can be used to estimate colloid size, by using $\lambda = 490,\ 550,$ and 650 nm as the peak wavelengths for the blue, green, and red channels respectively. This yielded an estimated diameter of 751nm whereas the real colloid size was 747nm.

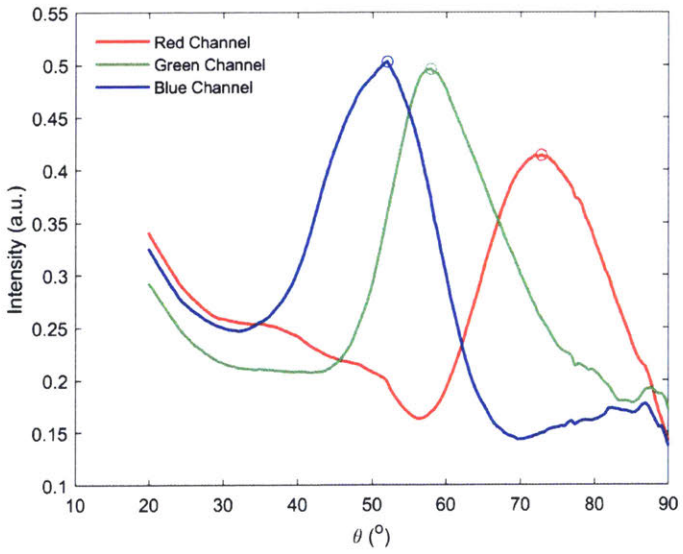

Figure S3.5. Polar Dependence of Diffracted light. Intensity measured from ping pong ball photographs for each of the RGB channels. The peak values can be used to determine colloid size.

More interestingly, the spacing and relative height of diffraction orders in the azimuthal direction gives an estimate of the grain structure. If there are many small grains present, then there will be many overlapping diffraction patterns, such that the scattered intensity is constant as ϕ is varied. If there are only a few grains present, however, then there will be distinct peaks visible in figure 4g.

In order to get an estimate of the size of the grains using this technique, we compare the relative intensity of each of the peaks. Because of the six-fold symmetry of the colloid structure, we only need to look at 60 degrees of the scattered light, therefore we average each of the 60-degree sections that is visible in our image of the ping pong ball, (figure S6a) Because scattering from the ping pong ball is not perfectly uniform, a white scatterer (Teflon tape) was used to normalize the azimuthal color distributions. The Teflon tape acts a Lambertion scatterer and should not be used to normalize in the polar direction, as its scattering profile does have a θ dependence.

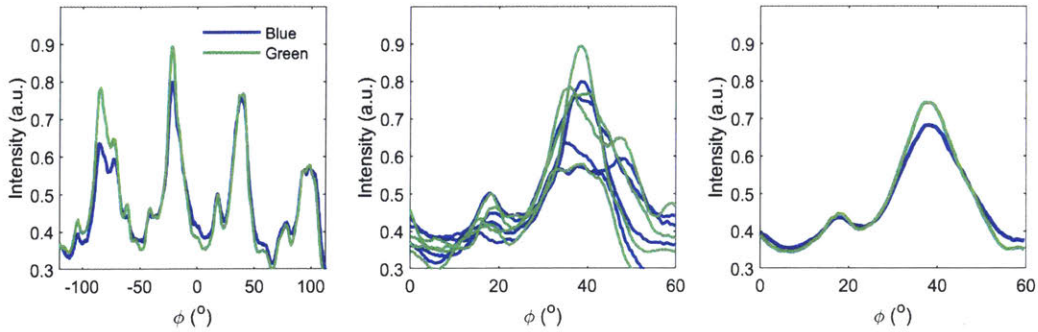

Figure S3.6. Azimuthal Dependence of Diffracted light. Intensity measured in the ping pong ball image through the peak θ values shown in Figure S3.5 . **a.)** full visible region of ping pong ball. **b.)** the data in (a) looped back over each 60-degree section, **c)** the average of (b), showing 2 distinct peaks in intensity corresponding to two large grains.

In the case of the example shown in Figure S3.6, there are two distinct peaks, as well as a low level continuum of diffraction from small grains. We first subtract off the background that can be associated with the illumination of the ping pong ball (dotted line in Figure S3.6c). The integral of the area under the curve corresponds to the total light scattered by the printed crystal. The area labeled as C corresponds to light scattered by small randomly oriented smaller grains. A and B correspond to larger grains. The relative height of A and B should correspond to the relative size of these two grains. The uncertainty is estimated from the standard deviation of the different 60-degree sections.

From this information, we can estimate that there is a large grain (A) that covers $41\% \pm 14\%$ of the illuminated area, a smaller grain (B), rotated about 20^o from the first, that covers $11\% \pm 6\%$ of the illuminated area, and the remaining $48\% \pm 17\%$ is covered by small, randomly oriented grains.

4 Generalizing direct-write assembly

4.1 General scaling of forces in direct-write assembly

As shown in Chapters 2 and 3, direct-write assembly can be used to assemble polystyrene particles spanning an order of magnitude in size (100 nm to 1 μm diameter). Nevertheless, given the vast library of colloidal building blocks available with modern synthetic techniques, it is of both fundamental interest and technological importance to explore if other colloidal particles are amenable to direct-write assembly.

The foremost task for generalizing direct-write assembly is to identify the forces that are relevant to the process. First, we consider the attractive and repulsive interaction potentials between particles to understand why the particles can assemble. Second, we consider the other forces: surface tension, thermal, viscous drag, and gravitational forces, which influence assembly. We then consider how these forces change when working with particles of different compositions and sizes.

The interaction potential is essential because the ability of a colloidal system to self-assemble depends on the magnitude and length scale of the interaction potential.[92] In general, for a system of particles to assemble, there must be a net attractive potential between the particles so that there can be a driving force for the particles to come together. However, if only an attractive potential exists, the particles will irreversibly stick together on first encounter and do not have ample opportunity to explore different space-filling configurations. For the particles to assemble

into a crystal, there must also be a repulsive potential between them. The repulsive potential, if comparable in magnitude to the attractive potential, can provide an energy barrier that prevents uncontrolled aggregation. This allows the particles to explore different space-filling configurations and eventually settle into crystalline positions, which is the minimum energy configuration. In the case of the polystyrene particles that we have used in all our experiments so far, there is a native negative charge due to anionic surfactants grafted onto the surface of the particle. The negative charge then provides the necessary repulsive potential. The attractive potential is due to van der Waals forces.

We now consider the case of steady state assembly, where a dilute dispersion of particles in the liquid bridge attempt to join a growing crystal. To simplify the physics of steady-state assembly, we may consider the potentials for a single particle approaching a flat semi-infinite solid, as illustrated in Fig. 4.1. This allows us to apply DLVO theory[93] as follows:

The attractive van der Waals potential of a sphere near a flat surface is approximated by[94]

$$U_{VDW} = -\frac{Aa}{6D} \qquad \text{Eq. 4.1}$$

where a is the particle radius, D is the distance between the surface of the particle and the flat surface, and A is the Hamaker constant, estimated to be of order 10^{-20} J. This approximation is valid for $D << a$.

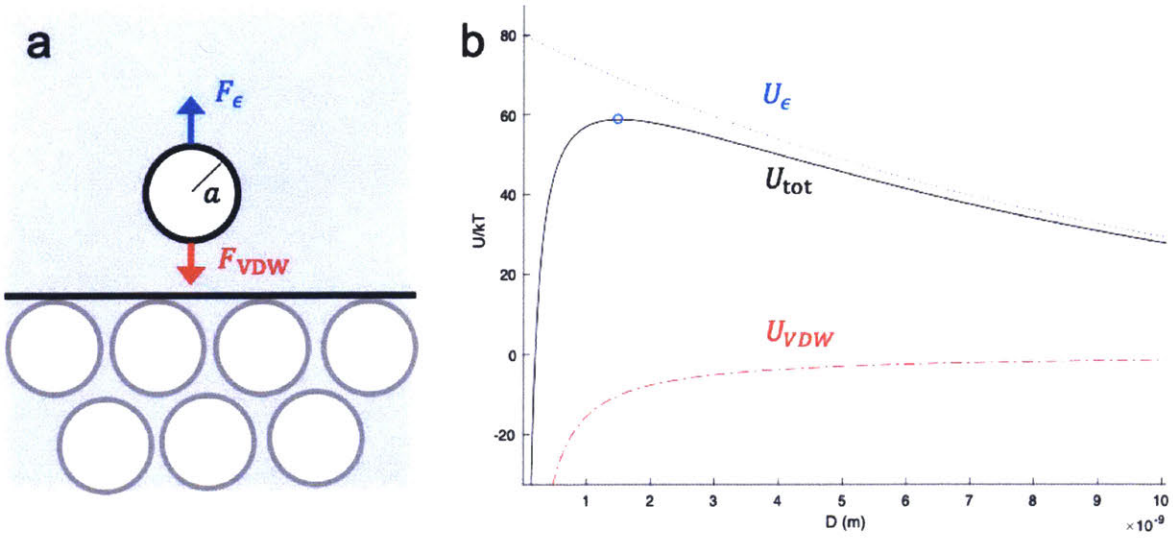

Figure 4.1. (a) A particle of radius a approaching a solid crystal array is simplified as a particle approaching a smooth surface. F_ϵ is the repulsive electrostatic force and F_{VDW} is the attractive van der Waals force. (b) Plot of the electrostatic potential U_ϵ, the van der Waals potential U_{VDW}, and the total potential U_{tot}.

The repulsive potential, for small separation distance ($D << a$), is given by[95]

$$U_\epsilon = aZe^{-\kappa D} \qquad \text{Eq. 4.2}$$

where κ is the Debye parameter, typically of order 10^8 nm^{-1}, and Z is the interaction constant for electrostatic interactions, given by

$$Z = 64\pi\varepsilon_0\varepsilon(kT/e)^2 \tanh^2(ze\psi_0/4kT) \qquad \text{Eq. 4.3}$$

where ε_0 is the permittivity of free space, ε is the relative permittivity of water at 70 °C, e is elementary charge, and ψ_0 is the surface potential, estimated to be 36 mV for 100 nm particles by a zeta potential analyzer.

The total potential, which is plotted in Fig. 4.1b, is the sum of the electrostatic potential and the van der Waals potential

$$U_{tot} = U_{\epsilon} + U_{VDW} \qquad \text{Eq. 4.4}$$

From Fig. 4.1b, we may observe that since U_{ϵ} scales as $\sim e^{-D}$, while U_{VDW} scales as $\sim 1/D$, van der Waals attraction dominate at short distances (<1 nm) while electrostatic repulsion dominates at larger distances (> 5 nm). At intermediate distances, there is an energy barrier which peaks at ~1.5 nm. It is this energy barrier that prevents uncontrolled agglomeration of particles into random aggregates. While Fig. 4.1b is based on a simplified physical picture and plotted based on values for polystyrene particles, its qualitative features should be generic to charged particles in aqueous dispersion.

Having established the nature of interaction potentials responsible for assembly, we now consider the other forces in direct-write assembly which act on the particles regardless of the interaction potentials. These forces are surface tension, thermal (osmotic) force, viscous (Stokes) drag, and gravitational force. The forces scales as listed in Table 4.1

Table 4.1. Scaling of surface tension, thermal force, viscous force, and gravitational force on spherical particles in direct-write assembly.

Force	**Equation**	
Surface tension	$F_{\gamma} \sim \gamma a$	Eq. 4.5
Thermal (osmotic)	$F_{kT} \sim kT/a$	Eq. 4.6

Viscous force on particle in motion through liquid	$F_\eta \sim 6\pi\eta u a$	Eq. 4.7
Gravity (buoyant)	$F_g \sim \frac{3}{4}\pi\Delta\rho g a^3$	Eq. 4.8

In the above table, γ is surface tension, k is the Boltzmann constant, T is the absolute temperature (343K for a typical experiment), η is the dynamic viscosity of water (404 μPa.s), $\Delta\rho$ is the difference in density between polystyrene and water, g is gravitational acceleration, and u is the velocity of the particle estimated to be the average flow velocity of the liquid dispensed from the needle.

It is instructive to visualize how these forces scale with respect to particle size, so that we may identify the range of particle sizes that may be amenable to direct write assembly. For the case of polystyrene particles in water, the plot of each force with respect to particle size is presented in Fig. 4.2a.

It is readily apparent that surface tension dominates over all other forces by at least 2 orders of magnitude from 10 to 10^5 nm. This agrees with the experimental observation that, when a particle touches the air-liquid interface, it is stuck the interface. Our typical experiments take place in the particle size regime of between 100 nm and 1 μm. In that regime, $F_\gamma > F_\eta > F_{kT} > F_g$. Therefore, viscous drag force drives the particles toward the bottom of the liquid bridge, where they concentrate into a crystal. The viscous drag force is sufficient to go against the thermal force which favors diffusion of particles away from the crystal. The gravitational force is the weakest force in this range of particle size, and therefore sedimentation can be neglected.

We also note three important regimes where there are crossovers between thermal force, viscous force, and gravitational force.

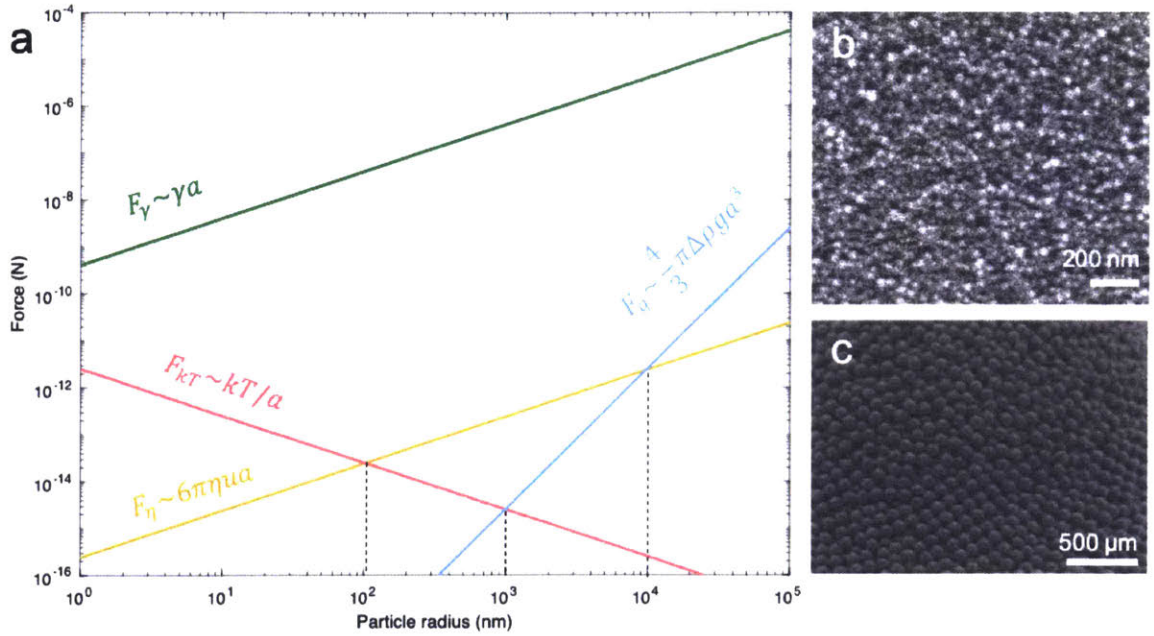

Figure 4.2. (a) Scaling of forces with respect to particle radius *a*. (b) SEM of 40 nm particles (c) SEM of 10 μm particles.

Below $a \sim 100$ nm, kT becomes comparable with the viscous force. Therefore, it may be difficult to assemble particles below $a \sim 100$ nm as the viscous force driving the particles together has to compete against the thermal force driving the particles away from each other. Fig. 4.2b shows an SEM of attempted assembly of a = 40 nm particles, where the particles are disordered despite a tight size distribution (CV < 0.01).

Above $a \sim 1$ μm, F_g becomes competitive with kT. Therefore, sedimentation may become appreciable, but it is not yet competitive with the viscous drag force that drives the particles down the liquid bridge.

Above $a \sim 10$ μm, F_g becomes competitive with F_η, which means that the particles are subject to sedimentation more than entrainment by the viscous drag force. Since the sedimentation cannot be controlled to regulate the rate of assembly, the particles tend to sediment into amorphous deposits, as shown in Fig. 4.2c.

Therefore, for polystyrene particles, the window of particle sizes appropriate for direct-write assembly is 100 nm < a < 1 μm.

4.2 Direct-write assembly of non-polymer particles

Although the above discussion centered on polystyrene particles as a model system, the qualitative themes are general and the scaling of forces may be applied to other colloids. To explore the generality of direct-write assembly beyond polymer particles, we choose to assemble gold and silica nanoparticles as respective examples of a conductive metal and dielectric ceramic. As shown in Fig. 4.3a, with respect to particle size, the scaling of surface tension, thermal force, viscous force, and gravitational force do not change with particle composition. However, the magnitude of gravitational force changes appreciably due to the heavier densities of silica and gold. The crossover between F_η and F_g occurs at $a \approx 2$ μm for silica and $a \approx 500$ nm for gold. Meanwhile, the crossover between F_{kT} and F_η remains the same, at $a \approx 100$ nm. Therefore the window of particle sizes amenable to direct-write assembly is

between ~100 nm and ~2 μm for silica, and between ~100 nm and ~500 nm for gold.

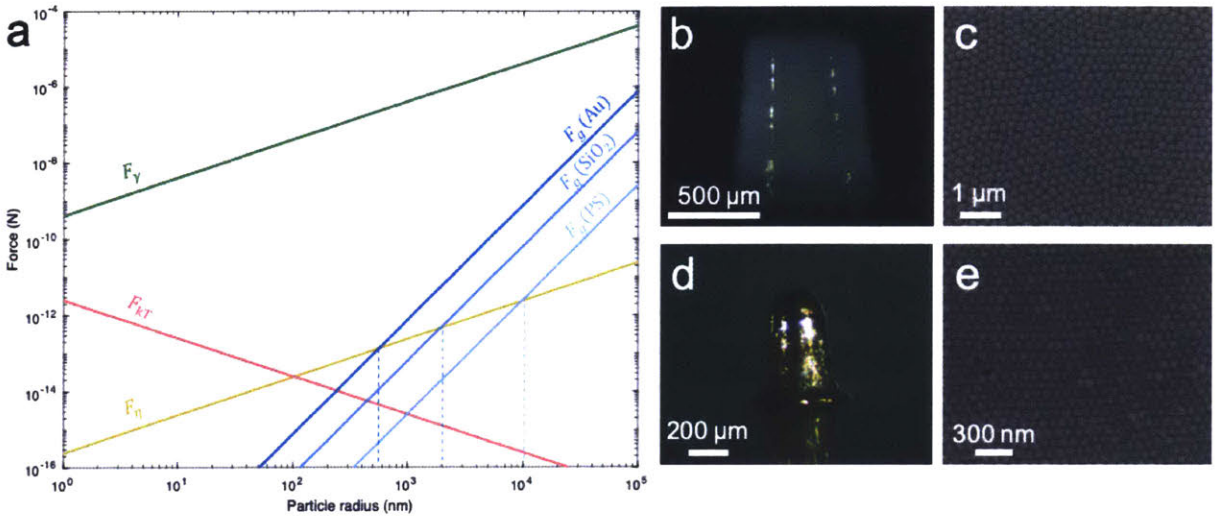

Figure 4.3. (a) Scaling of forces with respect to particle radius, for polystyrene (PS), silica (SiO_2), and gold (Au) particles. Note that only the magnitude of F_g changes with composition. (b) Optical and (c) SEM images of a direct-write structure composed of silica particles. (d) Optical and (e) SEM images of a direct-write structure composed of gold particles.

Furthermore, as discussed in the prior section, for a colloidal system to self-assemble, in addition to the ubiquitous van der Waals potential, there must be a repulsive potential. We therefore procured silica particles of a = 250 nm and gold particles of a = 100 nm functionalized with negatively charged carboxyl groups to provide the repulsive potential.

Direct-write assembly was then applied to the silica and gold particles. Fig. 4.3b-d shows optical and SEM images of the assembled structures, which have crystalline order.
Although these are two instances of direct-write assembly of non-polymer particles, these experiments imply that the scaling of forces provide guidelines to the choice of particle size and composition for successful direct-write assembly. We may then consider tailoring the properties of macroscale colloidal materials via deliberate choice of particle size and composition.

4.3 Direct-write assembly with non-aqueous colloids

This thesis has thus far explored direct-write assembly with various particle sizes and compositions, but only for particles dispersed in water. However, many colloidal particles require functionalization with long chain hydrocarbon ligands to be dispersible in organic solvents such as toluene. Therefore, in this section, we investigate the feasibility of performing direct-write assembly with nanoparticles dispersed in non-aqueous solvents, where the source of repulsive interactions is steric rather than electrostatic.

To investigate, we once again consider the magnitude and length scale of the interparticle interaction potentials, as well as the scaling of surface tension, thermal force, viscous force, and gravitational force with respect to particle size. As mentioned in Section 4.1, for self-assembly to occur, the particles interacting in a fluid medium must have both an attractive potential and a repulsive potential.

The attractive potential is provided by van der Waals forces. Between two spherical particles close to each other (D << a), the van der Waals potential is given by

$$U_{VDW} = \frac{-Aa}{12D} \qquad \text{Eq. 4.9}$$

In organic solvents, the repulsive potential is provided by steric forces. The steric repulsion potential, U_S, arises from the entropic penalty associated with the overlap of polymer chains. Between two spherical particles densely coated with long chain ligands,

$$U_s = \infty \qquad r < 2a$$

$$= \frac{\pi^2 akT\Gamma h_0^3}{6Nb^2}\left[-\ln u - \frac{9}{5}(1-u) + \frac{1}{3}(1-u^3) - \frac{1}{30}(1-u^6)\right] \qquad 2a \le r \le 2(a+2h_0)$$

$$= 0 \qquad r > 2(a + h_0)$$

Eq. 4.10

Where Γ is the surface density of grafted polymers, h_0 is the equilibrium length of the grafted polymer, N is the number of Kuhn monomers, b is the length of each Kuhn monomer, and the variable u is defined as

$$u = \frac{r-2a}{2h_0} \qquad \text{Eq. 4.11}$$

We identified oleic-acid functionalized iron oxide nanoparticles dispersed in toluene as promising system for direct-write assembly. Prior work by Dreyer et al. showed that these functionalized iron oxide nanoparticles are capable of self-assembly into a supercrystal, and the oleic acid ligands are capable of thermally-induced crosslinking reactions, as illustrated in Fig. 4.4. The crosslinked supercrystal has been shown to have exceptional mechanical properties (hardness of 4 GPa and strength of 630 MPa).[96]

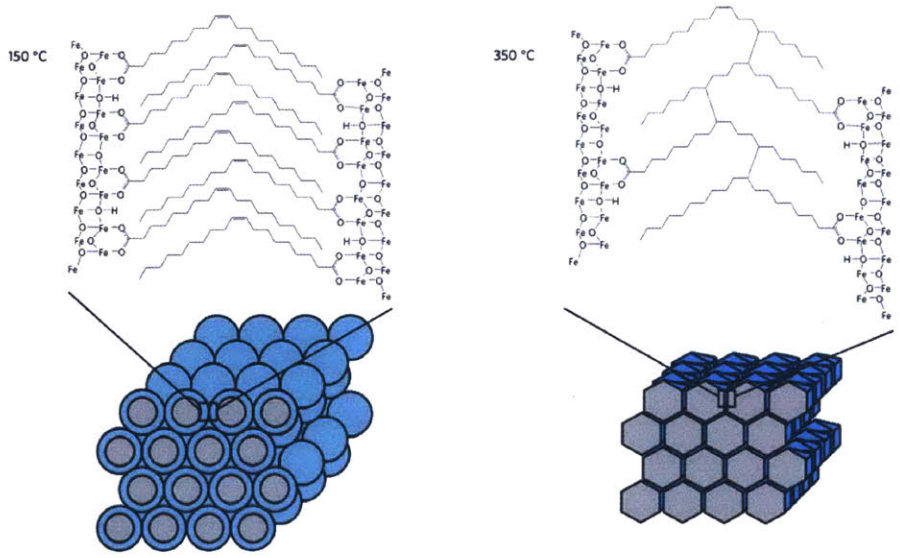

Figure 4.4. Iron oxide nanoparticles functionalized with oleic acid self-assemble into a supercrystal (left), which can be thermally treated to induce cross-linking of the particles (right). Reproduced from [96]

The estimated interparticle potential between these particles is plotted in Fig. 4.5. The specific parameters for the functionalized iron oxide nanoparticles are a = 10 nm, $\Gamma = 1\ \mathrm{nm}^{-2}$, b = 1.1 nm, h_0 = 1.97 nm (molecular length of oleic acid), and N is related to the number of chemical monomers, n, as N = 0.15n. For oleic acid, n = 18. We observe that, at slightly before the equilibrium brush thickness, the magnitude of the steric repulsion rises very sharply. Due to the compressibility of the ligands, the energy minimum is at r_0 = 23.10 nm, and the separation between the particle surfaces is $r_0 - 2a$ = 3.10 nm, which is slightly less than what it would be if the ligands were fully extended, $2h_0$ = 3.94 nm. Therefore, one may approximate the stabilizing ligands has hard shells, which only slightly compress when the particles self-assemble.

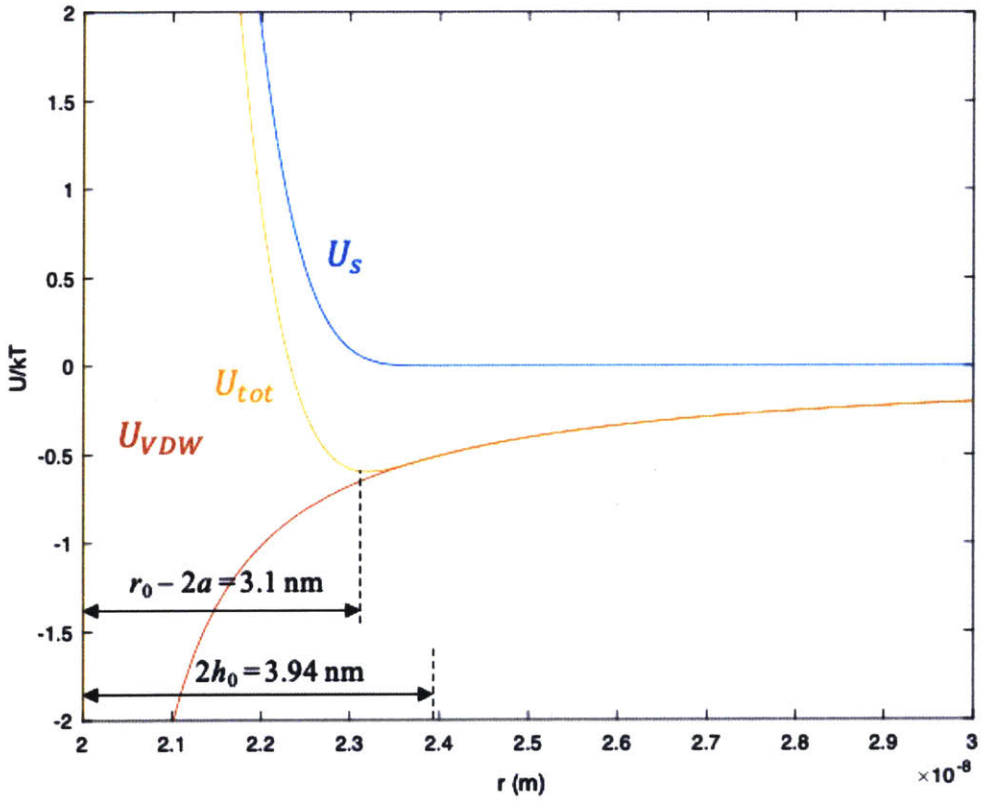

Figure 4.5. Plot of the interparticle potentials between two a = 10 nm iron oxide nanoparticles. The total interparticle potential (yellow) is the sum of the van der Waals potential (red) and the steric potential (blue).

With the assurance that a particle system has at least the appropriate interparticle interaction potential for self-assembly, one should then estimate the scaling of forces in direct-write assembly with respect to particle size, and identify the range of particle sizes amenable to direct-write assembly.

To investigate if the iron oxide nanoparticles are amenable to direct-write assembly, we plotted the magnitudes of surface tension, thermal force, viscous force, and gravitational force, as shown in Fig. 4.6. Here it is assumed that the iron oxide particles have a density of 5.4 gm/cm^3 and that the particles are dispersed in toluene, which has a density of 0.865 g/cm^3 and viscosity of 560 μPa.s, and surface tension of 29.7 mN/m. The plot suggests that, for successful direct-write assembly, the particle size should be no smaller than ~8 nm to prevent thermally-induced disorder and no larger than ~10 μm to prevent sedimentation-induced aggregation.

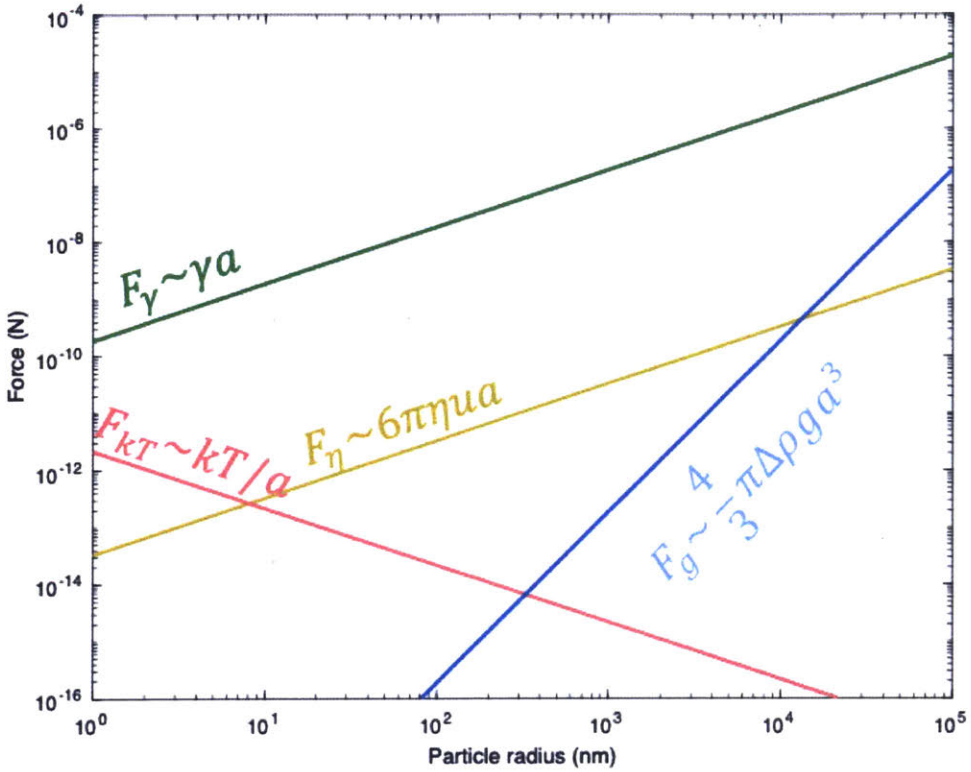

Figure. 4.6. Scaling of forces with respect to particle radius, for iron oxide particles in toluene.

Furthermore, since we are investigating a change in solvent from water to toluene, an additional matter to consider is whether a liquid bridge can be formed with toluene, especially since toluene has a much smaller surface tension (29.7 mN/m) compared to water (72.8 mN/m). As described in Chapter 2, the liquid bridge is essential for direct-write assembly because the meniscus of the liquid bridge provides spatial confinement for crystallization to take place, and the bridge allows particles to dispensed continuously for uninterrupted crystal growth.

The formation of a liquid bridge is determined by a balance between gravitational force and surface tension. Here, we may consider another length scaling factor, the capillary constant λ_c, which is given by

$$\lambda_c = \sqrt{\frac{\gamma}{\rho g}} \qquad \text{Eq. 4.12}$$

For water, the capillary constant is ~3 mm. This means that the liquid bridge can be extended to approximately 3 mm before rupturing. For toluene, the capillary constant is calculated to be ~ 2 mm. Although the surface tension for toluene is lower than water, its density is also lower, which results in a capillary constant similar to water. Therefore, it is reasonable to attempt direct-write assembly with a toluene-based colloidal suspension.

We attempted direct-write assembly with 18 nm iron oxide nanoparticles dispersed in toluene at a concentration of 55.8 mg/ml (corresponding to a particle volume fraction of 0.01). Due to the fast evaporation rate of toluene, the experiment was performed at room temperature instead of the temperature of 70 °C that we used for water. All other aspects of the experiment remained essentially the same. The assembled tower, shown in Fig. 4.7a, has a diameter of 100 μm and height of 1.5 mm. Fig. 4.7b shows SEM of the fracture surface of the tower, which shows terraces of particles and 60° cleavage lines, confirming the crystallinity of the structure.

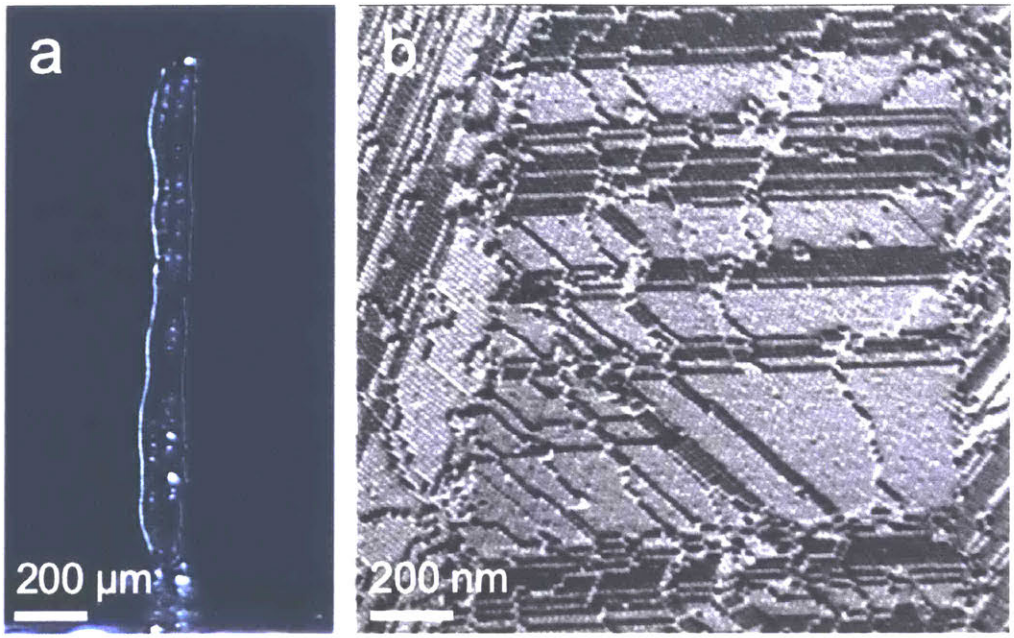

Figure 4.7. Iron oxide supercrystal fabricated by direct-write assembly. (a) Optical image of the supercrystal. (b) SEM image of the fracture surface, exposing cleavage planes characteristic of a crystalline structure.

Through the example of oleic acid functionalized iron oxide nanoparticles dispersed in toluene, we have extended the direct-write assembly technique to non-aqueous colloidal systems. We also discussed the importance of the capillary constant in formation of the liquid bridge. Table 4.2 shows a list of other organic solvents and their capillary constants. All the capillary constants appear to be greater than 1 mm, which suggests that it would be possible to use these solvents to form a liquid bridge as long as the needle-substrate gap is smaller than 1 mm. The selection of particle composition and size would then be decided by the scaling of forces and interparticle potentials as discussed above. Since one of the most attractive advantages of direct-write assembly is the ability to tailor material properties by choice of colloidal particle, it is

hoped that this chapter serves as a guide to selecting the most promising colloidal systems for direct-write assembly.

Table 4.2. List of capillary constants for common organic solvents.

	γ (mN/m)	ρ (g/cm^3)	λ_c (cm)
Toluene	29.71	0.87	0.19
Hexane	18.40	0.66	0.17
Benzene	28.22	0.87	0.18
Diethyl ether	17.06	0.71	0.16
Chloroform	27.10	1.49	0.14
1,4-Dioxane	30.86	1.03	0.17

4.4 Observations on the limits of crystalline assembly

In Chapter 2, we showed that it is possible to build colloidal crystals exceeding centimeter heights (Fig. S2.4). A natural question to pose is whether there are intrinsic physics that limit how tall we can build a structure with direct-write assembly. Therefore, in this section, we report some observations on loss of crystallinity when attempting to build tall colloidal crystals from polystyrene particles.

In some of our experiments, we observed a loss in crystallinity which typically happens when the tower grows to aspect ratios larger than 5. The onset of the loss in crystallinity is observable with in situ video microscopy. We observe the particles start to disjoin from the tower and swirl around the liquid bridge. The snapshot of such swirling of the particles is shown in Fig.

4.8. The swirling continues for the rest of the tower build, and, as a result, the crystallinity at the top of the tower is disrupted, as shown in Fig. 4.9.

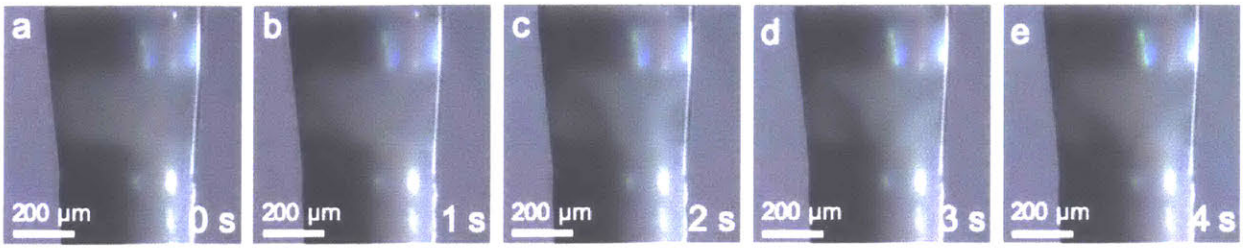

Figure 4.8. Series of optical images of particles disjoining from the solid and swirling in the liquid bridge.

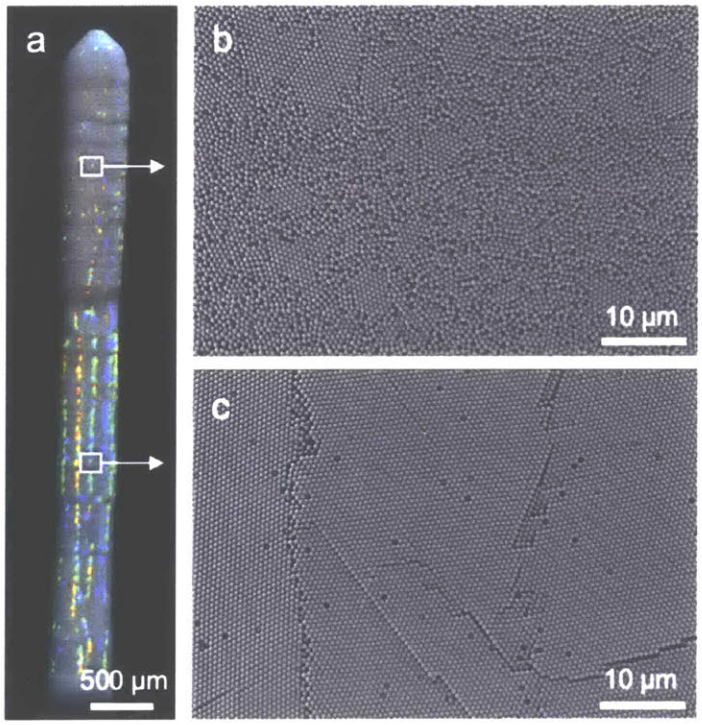

Figure 4.9. (a) Optical image of a colloidal tower, where the bottom half is crystalline and the top half is amorphous. (b) Representative SEM of the amorphous region. (c) Representative SEM of the crystalline region.

Previously, in Section 4.1, we discussed the role of the viscous drag force in directing the particles toward the tower at the bottom of the liquid bridge. Therefore, if the particles disjoin from the tower, then there must be a force that acts counter to the viscous force, i.e., from the bottom to the top of the liquid bridge. We hypothesize that the counter-acting force is electrostatic repulsion. As described in Section 4.1, each polystyrene particle has a slight negative charge due to the residual anionic surfactant molecules grafted on the surface of the particle. Therefore, there is an accumulation of negative charge as the tower grows. We hypothesize that the onset of particle swirling corresponds to a regime where the cumulative charge of particles in the tower results in an electrostatic repulsion that is strong enough to compete with the viscous force acting upon the particles.

The viscous force acting on a particle is given by the Stokes Equation (Eq. 3.7). Meanwhile, the electrostatic force acting on a particle located at the top of the tower can be calculated by an integration of Coulomb's Law over the volume of the tower, giving

$$F_q = 6\pi\sigma^2 a\left[\frac{\phi_T R_T}{\varepsilon_T}\left\{1+\xi-\sqrt{(1+\xi^2)}\right\}-\frac{\phi_N R_N}{\varepsilon_N}\right] \qquad \text{Eq. 4.13}$$

Where σ is the areal charge density on a particle, ϕ is the volume fraction of particles, ε is the dielectric permittivity, and the subscripts T and N refer to the tower and needle respectively. The quantity ξ is the aspect ratio $\xi = H/R_T$, where H is the height of the tower. The derivation of Eq. 4.13 is detailed in Supporting Information.

The ratio of the electrostatic force to the viscous force is given by

$$\frac{F_q}{F_\eta} = \frac{\sigma^2}{\eta v}\left[\frac{\phi_T R_T}{\varepsilon_T}\left\{1 + \xi - \sqrt{1+\xi^2}\right\} - \frac{\phi_N R_N}{\varepsilon_N}\right] \qquad \text{Eq. 4.14}$$

The onset of swirling should occur when $F_q/F_\eta \sim 1$ because the electrostatic repulsion becomes comparable to the viscous force. Interestingly, this effect should be independent of particle size because $F_q \sim a$ and $F_\eta \sim a$. Therefore, the role of particle size cancels out.

An intuition for F_q/F_η can be obtained by inspecting how the quantity $\left\{1 + \xi - \sqrt{1+\xi^2}\right\}$ varies as the tower grows. Figure 4.10 shows a plot of $\left\{1 + \xi - \sqrt{1+\xi^2}\right\}$ versus ξ. According to the plot, the quantity $\left\{1 + \xi - \sqrt{1+\xi^2}\right\}$ maxes out to unity at approximately $\xi = 10$.

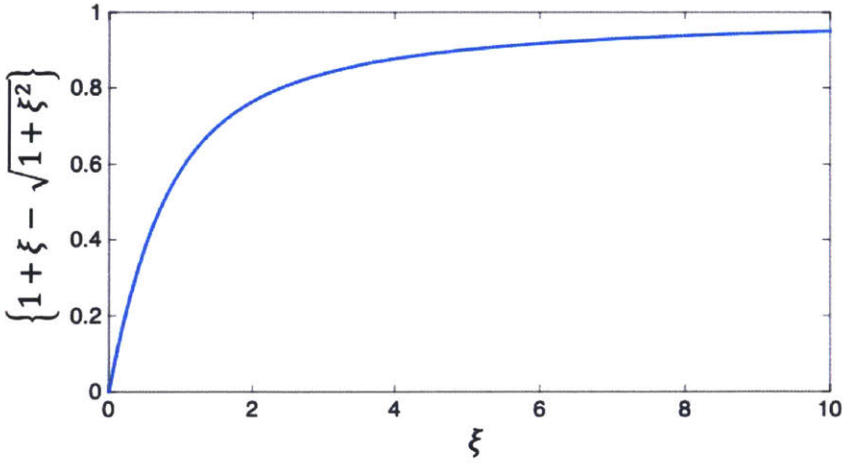

Figure 4.10. Plot of $\left\{1 + \xi - \sqrt{(1+\xi^2)}\right\}$ against ξ, where ξ is the aspect ratio $\xi = H/R_T$

Therefore, to avoid electrostatically impeded growth,

$$\frac{\sigma^2}{\eta v}\left[\frac{\phi_T R_T}{\varepsilon_T} - \frac{\phi_N R_N}{\varepsilon_N}\right] < 1 \qquad \text{Eq. 4.15}$$

Unfortunately, Eq. 4.15 is difficult to validate experimentally because the observation of particle swirling is difficult to reproduce, even under seemingly identical experimental conditions and a controlled temperature environment. Nonetheless, we note that, in exploring the ultimate height limits of direct-write assembly, one should consider non-obvious effects from the scaling of competing forces such as the competition between viscous force and electrostatic repulsion.

4.5 Supporting Information

Derivation of Electrostatic Force Equation 4.13 (Courtesy of Justin Beroz)

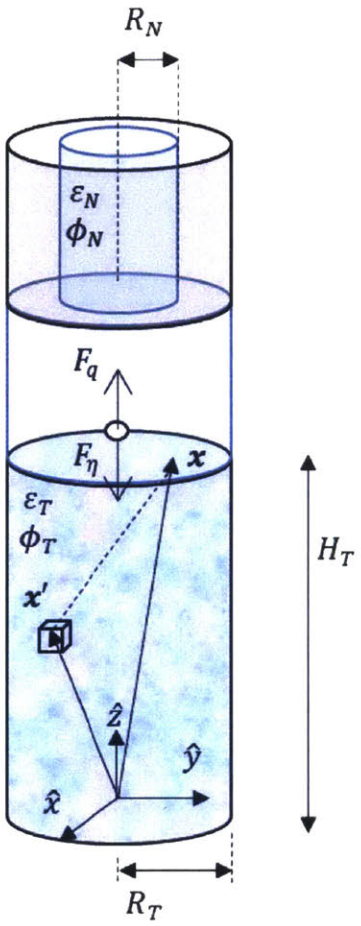

Figure S4.1: Coordinate system and quantities used to integrate the effect of electrostatic forces on a particle by the tower and the liquid column in the needle

According to Coulomb's Law, the differential electric field contribution at $\boldsymbol{x}$ from the differential element at $\boldsymbol{x'}$ is

$$d\mathbf{E}(\mathbf{x}) = \frac{\rho}{4\pi\tilde{\varepsilon}} \cdot \frac{\mathbf{x}-\mathbf{x}'}{|\mathbf{x}-\mathbf{x}'|^3}$$

where ρ is the charge density in a volume V

The total field at x is

$$\mathbf{E}(\mathbf{x}) = \frac{\rho}{4\pi\tilde{\varepsilon}}\int \frac{\mathbf{x}-\mathbf{x}'}{|\mathbf{x}-\mathbf{x}'|^3}d^3\mathbf{x}'$$

$$= \frac{-\rho}{4\pi\tilde{\varepsilon}}\nabla\int \frac{1}{|\mathbf{x}-\mathbf{x}'|}d^3\mathbf{x}' \qquad \text{since } \frac{\mathbf{x}-\mathbf{x}'}{|\mathbf{x}-\mathbf{x}'|^3} = -\nabla\left(\frac{1}{|\mathbf{x}-\mathbf{x}'|}\right); \quad \nabla = \frac{\partial}{\partial x_i}$$

Integrating over the cylindrical tower of radius R and height H in cylindrical coordinates:

$$\begin{cases} \mathbf{x} = r\mathbf{e}_1 + z\mathbf{e}_3 \\ d\mathbf{x} = rdrd\theta dz \end{cases}; \qquad \begin{cases} \mathbf{e}_1 = \cos\theta\hat{x} + \sin\theta\hat{y} \\ \mathbf{e}_2 = -\sin\theta\hat{x} + \cos\theta\hat{y} \\ \mathbf{e}_3 = \hat{z} \end{cases}; \qquad \nabla\psi = \frac{\partial\psi}{\partial r}\hat{r} + \frac{1}{r}\frac{\partial\psi}{\partial\theta}\hat{\theta} + \frac{\partial\psi}{\partial z}\hat{z}$$

$$\mathbf{E}(\mathbf{x}) = \frac{-\rho}{4\pi\varepsilon_{eff}}\nabla\int \frac{1}{|\mathbf{x}-\mathbf{x}'|}d^3\mathbf{x}'$$

$$= \frac{-\rho}{4\pi\varepsilon_{eff}}\nabla\int \frac{r'dr'd\theta'dz'}{\sqrt{(r\cos\theta - r'\cos\theta')^2 + (r\sin\theta - r'\sin\theta')^2 + (z-z')^2}} \qquad \begin{matrix} r':[0,R] \\ \theta':[0,2\pi] \\ z':[0,H] \end{matrix}$$

Simplifying the calculation to the field along center axis $r = 0$ & focusing on the $\hat{z}$ component:

$$E_z(0,z) = \frac{-\rho}{2\tilde{\varepsilon}}\frac{\partial}{\partial z}\iint dr'dz' \frac{r'}{\sqrt{r'^2 + (z-z')^2}} \qquad \text{performing } \theta \text{ integration here as well}$$

$$= \frac{-\rho}{2\tilde{\varepsilon}}\frac{\partial}{\partial z}\int_0^H dz'\left[\sqrt{r'^2 + (z-z')^2}\right]_{r'=0}^{r'=R}$$

$$= \frac{-\rho}{2\tilde{\varepsilon}}\frac{\partial}{\partial z}\int_0^H dz'\left\{\sqrt{R^2 + (z-z')^2} + \sqrt{(z-z')^2}\right\}$$

$$= \frac{-\rho}{2\tilde{\varepsilon}}\int_0^H dz'\left\{\frac{z-z'}{\sqrt{R^2 + (z-z')^2}} + \frac{z-z'}{\sqrt{(z-z')^2}}\right\}$$

$$= \frac{\rho}{2\tilde{\varepsilon}}\left[\sqrt{R^2 + (z-z')^2} - \sqrt{(z-z')^2}\right]_{z'=0}^{z'=H}$$

$$= \frac{\rho}{2\tilde{\varepsilon}}\left\{\left(\sqrt{R^2 + (z-H)^2} + H - z\right) - \left(\sqrt{R^2 + z^2} - z\right)\right\} \qquad \text{recognizing that only } z:[0,H] \text{ is physical}$$

$$= \frac{\rho R}{2\tilde{\varepsilon}}\left\{\left(\sqrt{1 + \left(\frac{z}{R} - \xi\right)^2} + \xi - \frac{z}{R}\right) - \left(\sqrt{1 + \left(\frac{z}{R}\right)^2} - \frac{z}{R}\right)\right\} \qquad \text{introducing aspect ratio } \xi := \frac{H}{R}$$

There is also a downward electrical force on a particle at $z = H_T$ from the column of particles above it in the dispensing needle. All our dispensing needles have ξ, and so, in summary, the electric force on this particle is

$$F_q = q\left[E_{z,Tower} + E_{z,Needle}\right] = 6\pi\sigma^2 a\left[\frac{\phi_T R_T}{\tilde{\varepsilon}_T}\left\{1 + \xi - \sqrt{1+\xi^2}\right\} - \frac{\phi_N R_N}{\tilde{\varepsilon}_N}\right]$$

for a particle tower built to aspect ratio $\xi = H_T / R_T$

5 Conclusion and Outlook

5.1 Summary

This thesis has introduced direct-write assembly as a fabrication technique that may be used to assemble colloidal building blocks into macroscale colloidal crystals. This thesis has explored two modes of direct-write assembly: Freeform assembly and in-plane assembly. In freeform assembly, we demonstrated the assembly of centimeter-scale freestanding colloidal crystals from polystyrene particles between 100 nm and 1 μm in size. We derived a scaling law that describes the rate of assembly, and demonstrated the emergence of structural color that can be tuned via the size and ordering of the particles. For in-plane assembly, we demonstrated that direct-write can be used to pattern planar colloidal crystals directly from a digital template, without the need for masks or etching. Leveraging the principles of convective assembly, the process can be optimized for high writing at mild process temperature while maintaining long-range order of the colloidal crystals. We establish structure-property relationships that allow microstructural information such as relative grain size and orientation to be deduced from the crystal's diffractive properties. Finally, we consider the scaling and magnitude of various forces in direct-write assembly and discuss how the direct-write technique may be employed to assemble a diverse range of particle size and compositions.

5.2 Future opportunities

One the most interesting questions that remains to be answered is whether direct-write assembly can be employed to grow a single crystal. Perhaps one may take inspiration from the Czochralski

process that is used to create single crystal ingots of electronic grade silicon. In the Czochralski process, a seed crystal is dipped into a melt and then slowly pulled upwards from the melt. In direct-write assembly, the liquid bridge is analogous to the melt, but the technique, as described in this thesis, does not involve the use of a seed. In future work, a patterned substrate, with grooves corresponding to close-pack arrangement of particles, may be used as the 'seed' to epitaxially induce crystal growth in a single direction.

Another area for further investigation is the improvement of mechanical properties of the colloidal crystals. Currently, the assembled particles are held together by weak van der Waals forces, and are therefore extremely fragile. Sintering of the particles may be able to improve the mechanical properties, but over-sintering will sacrifice the periodicity of the colloidal crystal, which is responsible for other properties such as structural color. Furthermore, the mechanical properties of the sintered structure will not exceed that of the bulk material. Perhaps one could take inspiration from natural materials such as nacre, which uses a hierarchical organization of soft organic and hard inorganic components, resulting in high strength and toughness. One could attempt to infiltrate the direct-write colloidal crystals with a polymer, but complete infiltration of the polymer into the colloidal crystal will be challenging. Blockage of the voids between the particles by the polymer causes the infiltration to be a self-limiting process. A better route may be to explore the assembly of particles consisting of a hard inorganic core grafted with soft polymer chains. Covalent crosslinking between the polymer chains would then improve the mechanical properties of the colloidal structure without sacrificing the periodicity of the crystal.

Finally, in an attempt to keep the physics of direct-write assembly simple, this thesis has explored only the assembly of one type of particle. A matter of fundamental curiosity is whether direct-write assembly can be used to assemble binary or multi-component crystals. This opens up a whole range of possibilities. Attempting to co-assemble differently sized particles, oppositely charged particles, and particles of different composition would surely result in many fascinating results – one can anticipate new crystal structures, defect engineering, synergistic photonic effects, just to name a few.

6 References

(1) Kolle, M.; Salgard-Cunha, P. M.; Scherer, M. R. J.; Huang, F.; Vukusic, P.; Mahajan, S.; Baumberg, J. J.; Steiner, U. Mimicking the Colourful Wing Scale Structure of the Papilio Blumei Butterfly. *Nat. Nanotechnol.* **2010**, *5* (7), 511–515.

(2) Zheng, X.; Shen, G.; Wang, C.; Li, Y.; Dunphy, D.; Hasan, T.; Brinker, C. J.; Su, B. L. Bio-Inspired Murray Materials for Mass Transfer and Activity. *Nat. Commun.* **2017**, *8*, 14921.

(3) Aizenberg, J.; Weaver, J. C.; Thanawala, M. S.; Sundar, V. C.; Morse, D. E.; Fratzl, P. Materials Science: Skeleton of Euplectella Sp.: Structural Hierarchy from the Nanoscale to the Macroscale. *Science (80-.).* **2005**, *309* (5732), 275–278.

(4) Blanco, A.; Chomski, E.; Grabtchak, S.; Ibisate, M.; John, S.; Leonard, S.; Lopez, C.; Meseguer, F.; Miguez, H.; Mondia, J.; et al. Large-Scale Synthesis of a Silicon Photonic Crystal with a Complete Three-Dimensional Bandgap near 1.5 Micrometres. *Nature* **2000**, *405* (6785), 437–440.

(5) Vlasov, Y. a; Bo, X. Z.; Sturm, J. C.; Norris, D. J. On-Chip Natural Assembly of Silicon Photonic Bandgap Crystals. *Nature* **2001**, *414* (6861), 289–293.

(6) Valden, M.; Lai, X.; Goodman, D. W. Onset of Catalytic Activity of Gold Clusters on Titania with the Appearance of Nonmetallic Properties. *Science* **1998**, *281* (5383), 1647–1650.

(7) Joo, S. H.; Choi, S. J.; Oh, I.; Kwak, J.; Liu, Z.; Terasaki, O.; Ryoo, R. Ordered Nanoporous Arrays of Carbon Supporting High Dispersions of Platinum Nanoparticles. *Nature* **2001**, *412* (6843), 169–172.

(8) Podsiadlo, P.; Kaushik, A. K.; Arruda, E. M.; Waas, A. M.; Shim, B. S.; Xu, J.; Nandivada, H.; Pumplin, B. G.; Lahann, J.; Ramamoorthy, A.; et al. Ultrastrong and Stiff Layered Polymer Nanocomposites. *Science* **2007**, *318* (5847), 80–83.

(9) Bonderer, L. J.; Studart, A. R.; Gauckler, L. J. Bioinspired Design and Assembly of Platelet Reinforced Polymer Films. *Science* **2008**, *319* (5866), 1069–1073.

(10) Lee, D.; Rubner, M. F.; Cohen, R. E. All-Nanoparticle Thin-Film Coatings. *Nano Lett.* **2006**, *6* (10), 2305–2312.

(11) Lee, Y.-J.; Braun, P. V. Tunable Inverse Opal Hydrogel PH Sensors. *Adv. Mater.* **2003**, *15* (78), 563–566.

(12) Zhang, H.; Braun, P. V. Three-Dimensional Metal Scaffold Supported Bicontinuous Silicon Battery Anodes. *Nano Lett.* **2012**, *12* (6), 2778–2783.

(13) Tao, A.; Kim, F.; Hess, C.; Goldberger, J.; He, R.; Sun, Y.; Xia, Y.; Yang, P. Langmuir–Blodgett Silver Nanowire Monolayers for Molecular Sensing Using Surface-

Enhanced Raman Spectroscopy.

(14) Velev, O. D.; Lenhoff, A. M.; Kaler, E. W. A Class of Microstructured Particles through Colloidal Crystallization. *Science* **2000**, *287* (5461), 2240–2243.

(15) Yi, G. R.; Manoharan, V. N.; Klein, S.; Brzezinska, K. R.; Pine, D. J.; Lange, F. F.; Yang, S. M. Monodisperse Micrometer-Scale Spherical Assemblies of Polymer Particles. *Adv. Mater.* **2002**, *14* (16), 1137–1140.

(16) Brugarolas, T.; Tu, F.; Lee, D. Directed Assembly of Particles Using Microfluidic Droplets and Bubbles. *Soft Matter* **2013**, *9* (38), 9046.

(17) Zhao, Y.; Shang, L.; Cheng, Y.; Gu, Z. Spherical Colloidal Photonic Crystals. *Acc. Chem. Res.* **2014**, *47* (12), 3632–3642.

(18) Vogel, N.; Utech, S.; England, G. T.; Shirman, T.; Phillips, K. R.; Koay, N.; Burgess, I. B.; Kolle, M.; Weitz, D. A.; Aizenberg, J. Color from Hierarchy: Diverse Optical Properties of Micron-Sized Spherical Colloidal Assemblies. *Proc. Natl. Acad. Sci.* **2015**, *112* (35), 10845–10850.

(19) Luo, J.; Jang, H. D.; Sun, T.; Xiao, L.; He, Z.; Katsoulidis, A. P.; Kanatzidis, M. G.; Gibson, J. M.; Huang, J. Compression and Aggregation-Resistant Particles of Crumpled Soft Sheets. *ACS Nano* **2011**, *5* (11), 8943–8949.

(20) Luo, J.; Jang, H. D.; Huang, J. Effect of Sheet Morphology on the Scalability of Graphene-Based Ultracapacitors. *ACS Nano* **2013**, *7* (2), 1464–1471.

(21) Liu, S.; Wang, A.; Li, Q.; Wu, J.; Chiou, K.; Huang, J.; Luo, J. Crumpled Graphene Balls Stabilized Dendrite-Free Lithium Metal Anodes. *Joule* **2017**, *2* (1), 184–193.

(22) Vlasov, Y. a; Bo, X. Z.; Sturm, J. C.; Norris, D. J. On-Chip Natural Assembly of Silicon Photonic Bandgap Crystals. *Nature* **2001**, *414* (6861), 289–293.

(23) Vogel, N.; Utech, S.; England, G. T.; Shirman, T.; Phillips, K. R.; Koay, N.; Burgess, I. B.; Kolle, M.; Weitz, D. A.; Aizenberg, J. Color from Hierarchy: Diverse Optical Properties of Micron-Sized Spherical Colloidal Assemblies. *Proc. Natl. Acad. Sci.* **2015**.

(24) Xia, Y.; Gates, B.; Yin, Y.; Lu, Y. Monodispersed Colloidal Spheres: Old Materials with New Applications. *Adv. Mater.* **2000**, *12* (10), 693–713.

(25) Whitesides, G. M.; Grzybowski, B. Self-Assembly at All Scales. *Science (New York, N.Y.)*. American Association for the Advancement of Science March 29, 2002, pp 2418–2421.

(26) Deegan, R. D.; Bakajin, O.; Dupont, T. F.; Huber, G.; Nagel, S. R.; Witten, T. A. Capillary Flow as the Cause of Ring Stains from Dried Liquid Drops. *Nature* **1997**, *389* (6653), 827–829.

(27) Szekeres, M.; Kamalin, O.; Schoonheydt, R. A.; Wostyn, K.; Clays, K.; Persoons, A.; Dekany, I. Ordering and Optical Properties of Monolayers and Multilayers of Silica

Spheres Deposited by the Langmuir-Blodgett Method. *J. Mater. Chem.* **2002**, *12*, 3268–3274.

(28) Yin, Y.; Lu, Y.; Gates, B.; Xia, Y. Template-Assisted Self-Assembly: A Practical Route to Complex Aggregates of Monodispersed Colloids with Well-Defined Sizes, Shapes, and Structures. *J. Am. Chem. Soc.* **2001**, *123* (36), 8718–8729.

(29) Yang, H.; Jiang, P. Large-Scale Colloidal Self-Assembly by Doctor Blade Coating. *Langmuir* **2010**, *26* (16), 13173–13182.

(30) Fleck, N. A.; McMeeking, R. M.; Kraus, T. Convective Assembly of a Particle Monolayer. *Langmuir* **2015**, *31* (51), 13655–13663.

(31) Sharma, M.; Tan, A. T. L.; Smith, B. D.; Hart, A. J.; Grossman, J. C. Hierarchically Structured Nanoparticle Monolayers for the Tailored Etching of Nanoporous Silicon. *ACS Appl. Nano Mater.* **2019**, *2* (3), 1146–1151.

(32) Masuda, Y.; Itoh, T.; Itoh, M.; Koumoto, K. Self-Assembly Patterning of Colloidal Crystals Constructed from Opal Structure or NaCl Structure. *Langmuir* **2004**, *20* (13), 5588–5592.

(33) Huang, J.; Kim, F.; Tao, A. R.; Connor, S.; Yang, P. Spontaneous Formation of Nanoparticle Stripe Patterns through Dewetting. *Nat. Mater.* **2005**, *4* (12), 896–900.

(34) Adams, J. J.; Duoss, E. B.; Malkowski, T. F.; Motala, M. J.; Ahn, B. Y.; Nuzzo, R. G.; Bernhard, J. T.; Lewis, J. A. Conformal Printing of Electrically Small Antennas on Three-Dimensional Surfaces. *Adv. Mater.* **2011**, *23* (11), 1335–1340.

(35) Compton, B. G.; Lewis, J. A. 3D-Printing of Lightweight Cellular Composites. *Adv. Mater.* **2014**, *26* (34), 5930–5935.

(36) Sun, K.; Wei, T. S.; Ahn, B. Y.; Seo, J. Y.; Dillon, S. J.; Lewis, J. A. 3D Printing of Interdigitated Li-Ion Microbattery Architectures. *Adv. Mater.* **2013**, *25* (33), 4539–4543.

(37) Scheel, M.; Seemann, R.; Brinkmann, M.; Di Michiel, M.; Sheppard, A.; Breidenbach, B.; Herminghaus, S. Morphological Clues to Wet Granular Pile Stability. *Nat. Mater.* **2008**, *7* (3), 189–193.

(38) Adams, J. J.; Duoss, E. B.; Malkowski, T. F.; Motala, M. J.; Ahn, B. Y.; Nuzzo, R. G.; Bernhard, J. T.; Lewis, J. a. Conformal Printing of Electrically Small Antennas on Three-Dimensional Surfaces. *Adv. Mater.* **2011**, *23* (11), 1335–1340.

(39) Murphy, S. V; Atala, A. 3D Bioprinting of Tissues and Organs. *Nat. Biotechnol.* **2014**, *32* (8), 773–785.

(40) Zorlutuna, P.; Annabi, N.; Camci-Unal, G.; Nikkhah, M.; Cha, J. M.; Nichol, J. W.; Manbachi, A.; Bae, H.; Chen, S.; Khademhosseini, A. Microfabricated Biomaterials for Engineering 3D Tissues. *Adv. Mater.* **2012**, *24*, 1782–1804.

(41) Bertassoni, L. E.; Cecconi, M.; Manoharan, V.; Nikkhah, M.; Hjortnaes, J.; Cristino, A.

L.; Barabaschi, G.; Demarchi, D.; Dokmeci, M. R.; Yang, Y.; et al. Hydrogel Bioprinted Microchannel Networks for Vascularization of Tissue Engineering Constructs. *Lab Chip* **2014**, *14* (13), 2202–2211.

(42) Zhu, C.; Han, T. Y.-J.; Duoss, E. B.; Golobic, A. M.; Kuntz, J. D.; Spadaccini, C. M.; Worsley, M. A. Highly Compressible 3D Periodic Graphene Aerogel Microlattices. *Nat. Commun.* **2015**, *6* (1), 6962.

(43) Smay, J. E.; Cesarano, J.; Lewis, J. A. Colloidal Inks for Directed Assembly of 3-D Periodic Structures. *Langmuir* **2002**, *18* (14), 5429–5437.

(44) Ahn, B. Y.; Duoss, E. B.; Motala, M. J.; Guo, X.; Park, S.-I.; Xiong, Y.; Yoon, J.; Nuzzo, R. G.; Rogers, J. A.; Lewis, J. A. Omnidirectional Printing of Flexible, Stretchable, and Spanning Silver Microelectrodes. *Science* **2009**, *323* (5921), 1590–1593.

(45) Chopin, J.; Kudrolli, A. Building Designed Granular Towers One Drop at a Time. *Phys. Rev. Lett.* **2011**, *107* (20), 208304.

(46) Kagan, C. R.; Murray, C. B. Charge Transport in Strongly Coupled Quantum Dot Solids. *Nat. Nanotechnol.* **2015**, *10* (12), 1013–1026.

(47) Hilhorst, J.; Van Schooneveld, M. M.; Wang, J.; De Smit, E.; Tyliszczak, T.; Raabe, J.; Hitchcock, A. P.; Obst, M.; De Groot, F. M. F.; Petukhov, A. V. Three-Dimensional Structure and Defects in Colloidal Photonic Crystals Revealed by Tomographic Scanning Transmission x-Ray Microscopy. *Langmuir* **2012**, *28* (7), 3614–3620.

(48) Philipse, A. P.; Pathmamanoharan, C. Liquid Permeation (and Sedimentation) of Dense Colloidal Hard-Sphere Packings. *J. Colloid Interface Sci.* **1993**, *159* (1), 96–107.

(49) Aguirre, C. I.; Reguera, E.; Stein, A. Tunable Colors in Opals and Inverse Opal Photonic Crystals. *Adv. Funct. Mater.* **2010**, *20* (16), 2565–2578.

(50) von Freymann, G.; Kitaev, V.; Lotsch, B. V.; Ozin, G. A.; Spahn, P.; Ruhl, T.; Ozin, G. A.; Vekris, E.; Manners, I.; Aitchison, S.; et al. Bottom-up Assembly of Photonic Crystals. *Chem. Soc. Rev.* **2013**, *42* (7), 2528.

(51) Park, J. G.; Kim, S. H.; Magkiriadou, S.; Choi, T. M.; Kim, Y. S.; Manoharan, V. N. Full-Spectrum Photonic Pigments with Non-Iridescent Structural Colors through Colloidal Assembly. *Angew. Chemie - Int. Ed.* **2014**, *53* (11), 2899–2903.

(52) Takeoka, Y.; Yoshioka, S.; Teshima, M.; Takano, A.; Harun-Ur-Rashid, M.; Seki, T. Structurally Coloured Secondary Particles Composed of Black and White Colloidal Particles. *Sci. Rep.* **2013**, *3* (1), 2371.

(53) Takeoka, Y.; Yoshioka, S.; Takano, A.; Arai, S.; Nueangnoraj, K.; Nishihara, H.; Teshima, M.; Ohtsuka, Y.; Seki, T. Production of Colored Pigments with Amorphous Arrays of Black and White Colloidal Particles. *Angew. Chemie - Int. Ed.* **2013**, *52* (28), 7261–7265.

(54) Josephson, D. P.; Popczun, E. J.; Stein, A. Effects of Integrated Carbon as a Light Absorber on the Coloration of Photonic Crystal-Based Pigments. *J. Phys. Chem. C* **2013**, *117* (26), 13585–13592.

(55) Yan, Q.; Yu, J.; Cai, Z.; Zhao, X. S. Colloidal Photonic Crystals: Fabrication and Applications. In *Hierarchically Structured Porous Materials*; Wiley-VCH Verlag GmbH & Co. KGaA: Weinheim, Germany, 2011; pp 531–576.

(56) Routh, A. F. Drying of Thin Colloidal Films. *Reports Prog. Phys.* **2013**, *76* (4), 046603.

(57) Goehring, L.; Clegg, W. J.; Routh, A. F. Plasticity and Fracture in Drying Colloidal Films. *Phys. Rev. Lett.* **2013**, *110* (2), 024301.

(58) Míguez, H.; López, C.; Meseguer, F. J.; Blanco, Á.; Vázquez, L.; Mayoral, R.; Ocaña, M.; Fornés, V.; Mifsud, A.; Ocaña, M. Photonic Crystal Properties of Packed Submicrometric SiO2 Spheres. *Appl. Phys. Lett.* **1997**, *71* (9), 1148.

(59) Jiang, P.; Bertone, J. F.; Hwang, K. S.; Colvin, V. L. Single-Crystal Colloidal Multilayers of Controlled Thickness. *Chemistry of Materials*. American Chemical Society 1999, pp 2132–2140.

(60) Schall, P.; Cohen, I.; Weitz, D. A.; Spaepen, F. Visualization of Dislocation Dynamics in Colloidal Crystals. *Science* **2004**, *305* (5692), 1944–1948.

(61) Schall, P.; Cohen, I.; Weitz, D. A.; Spaepen, F. Visualizing Dislocation Nucleation by Indenting Colloidal Crystals. *Nature* **2006**, *440* (7082), 319–323.

(62) Tam, E.; Podsiadlo, P.; Shevchenko, E.; Ogletree, D. F.; Delplancke-Ogletree, M.-P.; Ashby, P. D. Mechanical Properties of Face-Centered Cubic Supercrystals of Nanocrystals. *Nano Lett.* **2010**, *10* (7), 2363–2367.

(63) Okubo, T. Melting Temperature of Colloidal Crystals of Polystyrene Spheres. *J. Chem. Phys.* **1991**, *95* (5), 3690.

(64) Peng, Y.; Wang, Z.; Alsayed, A. M.; Yodh, A. G.; Han, Y. Melting of Colloidal Crystal Films. *Phys. Rev. Lett.* **2010**, *104* (20), 205703.

(65) Lin, N. Y. C.; Bierbaum, M.; Schall, P.; Sethna, J. P.; Cohen, I. Measuring Nonlinear Stresses Generated by Defects in 3D Colloidal Crystals. *Nat. Mater.* **2016**, *15* (11), 1172–1176.

(66) Cheng, W.; Wang, J.; Jonas, U.; Fytas, G.; Stefanou, N. Observation and Tuning of Hypersonic Bandgaps in Colloidal Crystals. *Nat. Mater.* **2006**, *5* (10), 830–836.

(67) Ganapathy, R.; Buckley, M. R.; Gerbode, S. J.; Cohen, I. Direct Measurements of Island Growth and Step-Edge Barriers in Colloidal Epitaxy. *Science* **2010**, *327* (5964), 445–448.

(68) Lin, S.-Y.; Lin, Y.-Y.; Chen, E.-M.; Hsu, C.-T.; Kwan, C.-C. A Study of the Equilibrium Surface Tension and the Critical Micelle Concentration of Mixed Surfactant Solutions. *Langmuir* **1999**, *15* (13), 4370–4376.

(69) Kestin, J.; Sokolov, M.; Wakeham, W. A. Viscosity of Liquid Water in the Range of -8 °C to 150 °C. *J. Phys. Chem.* **1978**, *7* (3), 1978.

(70) Barenblatt, G. I. *Scaling, Self-Similarity, and Intermediate Asymptotics*; Cambridge University Press, 1996.

(71) Dufresne, E. R.; Corwin, E. I.; Greenblatt, N. A.; Ashmore, J.; Wang, D. Y.; Dinsmore, A. D.; Cheng, J. X.; Xie, X. S.; Hutchinson, J. W.; Weitz, D. A. Flow and Fracture in Drying Nanoparticle Suspensions. *Phys. Rev. Lett.* **2003**, *91* (22), 224501.

(72) Joshi, K.; Gilchrist, J. F. Estimation of Drying Length during Particle Assembly by Convective Deposition. *J. Colloid Interface Sci.* **2017**, *496*, 222–227.

(73) Kinoshita, S.; Yoshioka, S. Structural Colors in Nature: The Role of Regularity and Irregularity in the Structure. *ChemPhysChem*. John Wiley & Sons, Ltd August 12, 2005, pp 1443–1459.

(74) Kolle, M.; Steiner, U. Structural Color in Animals. In *Encyclopedia of Nanotechnology*; Springer Netherlands: Dordrecht, 2019; pp 3840–3854.

(75) Burg, S. L.; Parnell, A. J. Self-Assembling Structural Colour in Nature. *Journal of Physics Condensed Matter*. IOP Publishing October 17, 2018, p 413001.

(76) Denkov, N. D.; Velev, O. D.; Kralchevsky, P. A.; Ivanov, I. B.; Yoshimura, H.; Nagayama, K. Two-Dimensional Crystallization. *Nature* **1993**, *361* (6407), 26–26.

(77) Van Blaaderen, A.; Ruel, R.; Wiltzius, P. Template-Directed Colloidal Crystallization. *Nature* **1997**, *385* (6614), 321–323.

(78) P. Jiang; J. F. Bertone; K. S. Hwang, and; Colvin*, V. L. Single-Crystal Colloidal Multilayers of Controlled Thickness. **1999**.

(79) Xia, Y.; Gates, B.; Yin, Y.; Lu, Y. Monodispersed Colloidal Spheres: Old Materials with New Applications. *Adv. Mater.* **2000**, *12* (10), 693–713.

(80) Cui, Y.; Björk, M. T.; Liddle, J. A.; Sönnichsen, C.; Boussert, B.; Alivisatos, A. P. Integration of Colloidal Nanocrystals into Lithographically Patterned Devices. *Nano Lett.* **2004**, *4* (6), 1093–1098.

(81) Burgess, I. B.; Mishchenko, L.; Hatton, B. D.; Kolle, M.; Lončar, M.; Aizenberg, J. Encoding Complex Wettability Patterns in Chemically Functionalized 3D Photonic Crystals. *J. Am. Chem. Soc.* **2011**, *133* (32), 12430–12432.

(82) Hou, J.; Li, M.; Song, Y. Patterned Colloidal Photonic Crystals. *Angew. Chemie Int. Ed.* **2018**, *57* (10), 2544–2553.

(83) Yin, Y.; Lu, Y.; Gates, B.; Xia, Y. Template-Assisted Self-Assembly: A Practical Route to Complex Aggregates of Monodispersed Colloids with Well-Defined Sizes, Shapes, and Structures. *J. Am. Chem. Soc.* **2001**, *123* (36), 8718–8729.

(84) Tan, A. T. L.; Beroz, J.; Kolle, M.; Hart, A. J. Direct-Write Freeform Colloidal Assembly. *Adv. Mater.* **2018**, *30* (44), 1803620.

(85) Dimitrov, A. S.; Nagayama, K. Continuous Convective Assembling of Fine Particles into Two-Dimensional Arrays on Solid Surfaces.

(86) Prevo, B. G.; Kuncicky, D. M.; Velev, O. D. Engineered Deposition of Coatings from Nano- and Micro-Particles: A Brief Review of Convective Assembly at High Volume Fraction. *Colloids Surfaces A Physicochem. Eng. Asp.* **2007**, *311* (1–3), 2–10.

(87) Kinoshita, S.; Yoshioka, S.; Miyazaki, J. Physics of Structural Colors. *Reports Prog. Phys.* **2008**, *71* (7), 076401.

(88) Goodling, A. E.; Nagelberg, S.; Kaehr, B.; Meredith, C. H.; Cheon, S. I.; Saunders, A. P.; Kolle, M.; Zarzar, L. D. Colouration by Total Internal Reflection and Interference at Microscale Concave Interfaces. *Nature*. Nature Publishing Group February 27, 2019, pp 523–527.

(89) Deglint, J.; Kazemzadeh, F.; Cho, D.; Clausi, D. A.; Wong, A. Numerical Demultiplexing of Color Image Sensor Measurements via Non-Linear Random Forest Modeling. *Sci. Rep.* **2016**, *6*.

(90) Deegan, R. D.; Bakajin, O.; Dupont, T. F.; Huber, G.; Nagel, S. R.; Witten, T. a. Capillary Flow as the Cause of Ring Stains from Dried Liquid Drops. *Nature* **1997**, *389* (6653), 827–829.

(91) Deegan, R. Pattern Formation in Drying Drops. *Phys. Rev. E* **2000**, *61* (1), 475–485.

(92) Bishop, K. J. M.; Wilmer, C. E.; Soh, S.; Grzybowski, B. A. Nanoscale Forces and Their Uses in Self-Assembly. *Small* **2009**, *5* (14), 1600–1630.

(93) Verwey, E. J. W. Theory of the Stability of Lyophobic Colloids. *J. Phys. Colloid Chem.* **1947**, *51* (3), 631–636.

(94) Israelachvili, J. N.; Israelachvili, J. N. Chapter 13 – Van Der Waals Forces between Particles and Surfaces. In *Intermolecular and Surface Forces*; 2011; pp 253–289.

(95) Israelachvili, J. N.; Israelachvili, J. N. Chapter 14 – Electrostatic Forces between Surfaces in Liquids. In *Intermolecular and Surface Forces*; 2011; pp 291–340.

(96) Dreyer, A.; Feld, A.; Kornowski, A.; Yilmaz, E. D.; Noei, H.; Meyer, A.; Krekeler, T.; Jiao, C.; Stierle, A.; Abetz, V.; et al. Organically Linked Iron Oxide Nanoparticle Supercrystals with Exceptional Isotropic Mechanical Properties. *Nat. Mater.* **2016**, *15* (5), 522–528.